The Dissertation Committee for Wei Jiang Certifies that this is the approved version of the following dissertation:

Hydrophilic Polymer Foam and Microsphere Templates for Fabrication of Microcellular Nickel and Graphene Foams with Energy Storage Applications

Committee:

Wei Li, Supervisor

Deji Akinwande

Jonathan Chen

Guihua Yu

Hydrophilic Polymer Foam and Microsphere Templates for Fabrication of Microcellular Nickel and Graphene Foams with Energy Storage Applications

by

Wei Jiang, B.E.; B.Lit.; M.E.; M.S.T.A.T.

Dissertation

Presented to the Faculty of the Graduate School of

The University of Texas at Austin

in Partial Fulfillment

of the Requirements

for the Degree of

Doctor of Philosophy

The University of Texas at Austin

December 2015

Dedication

To my lovely wife, and daughter: Zhuoya You, and Izabella Yihan Jiang

Acknowledgements

First of all, I would like to sincerely express my appreciation and gratitude to my advisor and committee chair Dr. Wei Li for his expert guidance, support, and encouragement throughout the duration of this research. He has been a great mentor both academically and professionally. I learned a great deal from him, and kept on the course of completing my doctoral program thanks for the right balance of critical advice and encouragement provided by him.

I would also like to thank Dr. Deji Akinwande, Dr. Jonathan Chen, and Dr. Guihua Yu for agreeing to serve on my doctoral committee. I am thankful to them for their valuable suggestions and advice.

I would like to thank my colleagues in the Nano and Bio Materials Processing and Manufacturing Lab Liang Ma, Yongha Kim, Sriharsha Srinivas Sundarram, Russell Borduin, Jingyu Ock, Hao Xin, Daniel Justiss, Xiaoran Li, and Anish Dabhi for their helpful inputs to this work. I would also thank Dr. Guihua Yu, Dr. Joseph Koo, Dr. Jonathan Chen and Dr. Rodney Ruoff for letting me use equipment in their labs.

Finally，I would like to thank my wife and my parents for their encouragement and support. I would also like to thank my friends from Austin for their support in the pursuit of the degree.

Hydrophilic Polymer Foam and Microsphere Templates for Fabrication of Microcellular Nickel and Graphene Foams with Energy Storage Applications

Wei Jiang, Ph.D.

The University of Texas at Austin, 2015

Supervisor: Wei Li

Hydrophilic polymer foam and microsphere templates have attracted tremendous attentions in the past decade due to their applicability in numerous areas such as catalyst carriers and mini-reactors, filtration media, carbon foam fabrication templates, thermal and electrical insulators, and tissue engineering scaffolds. Hydrophilic polymer sphere and foam templates can be used to fabricate microcellular nickel foams and graphene foams that are finding unique opportunities in energy storage applications, including battery electrodes and matrices for solar energy storage. In this study open celled hydrophilic polymer foams and microsphere templates with controllable pore size and porosity were fabricated via solid state foaming and vacuum-assisted assembling methods. Hydrophilic polymer foams were fabricated with disulfonated poly(arylene ether sulfone) (BPS) and poly(ethylene glycol) (PEG) miscible blends.

Polymer microsphere templates made with PMMA, paraffin, and EAA spheres were used as templates for fabricating bulk nickel foams, which were further used as a template to fabricate graphene foams. In order to achieve bulk microcellular nickel and graphene foams, a novel electro-polishing-assisted electroless nickel (Ni) deposition

process was developed to mitigate the diffusion limitation problem. Fundamental mechanisms of the proposed process were studied using a finite difference model considering both ion diffusion and chemical reaction inside the porous media. The fabricated microcellular Ni foams exhibited sufficient thermal stability and were used to fabricate three dimensional (3D) few-layer-graphene (FLG) foams using a chemical vapor deposition (CVD) method. The resulting graphene foams had a pore size less than 100 μm, density of 0.0020 $g \cdot cm^{-3}$, and strut wall thickness of 5 nm. The surface-to-volume ratio of the foam was 2.5×10^5 $m^2 \cdot m^{-3}$.

Table of Contents

List of Tables

List of Figures

Chapter 1. Introduction

1.1 MOTIVATION

Porous media, composed of different materials and featuring varying pore size and pore morphology, show increasing importance because of their potential applications in fields such as chemical reaction, filtration, thermal and electrical insulation, nano/micro fabrication, separation, energy storage, and biomedical engineering [1, 2]. Open-celled micro/nano hydrophilic polymeric foams, hydrophilic polymer microsphere templates, and open-celled metallic foams are materials with exclusive transport properties resulting in attractive applications. For instance, hydrophilic polymer foams and hydrophilic polymer microsphere templates can be applied as humidification membranes, separation membranes, and templates for patterning metal foams. Open-celled metal foams find applications as frames of energy storage device and as substrates for fabricating three dimensional (3D) graphene/graphite structures [2-4].

Many techniques have been developed for making hydrophilic polymer foams with mass infiltration and separation applications. However, those techniques are either not efficient or not environmentally friendly [5-12]. In addition, existing techniques are only capable of fabricating hydrophilic polymer foams with several hundred μm or mm level pores. It is expected that smaller pore size would bring better mass transportation, infiltration, and separation properties. Hence, new techniques for fabricating hydrophilic polymer foams with varying porosity, pore size of several micrometer or nanometer level are needed.

Efficient methods for fabricating bulk nickel foams with microcellular pores (1-100 μm) are also lacking. This category of nickel foams feature higher internal

surface area to accommodate active materials compared with commercial nickel foams with pore size of several hundred micrometers, and have better active materials infiltration performance compared with nickel foams with nano level pore size. Among the many metal foam fabrication methods, electroplating of close-packed sphere templates is considered a promising approach to microcellular nickel foam fabrication due to its ability to control the pore size and produce highly ordered microstructures [13, 14]. However, as the sphere size or pore size becomes smaller while the overall foam size remains at a bulk level, many challenges arise. For example, the electroplating process will be limited by the ion-diffusion process into the small pore sized polymer templates. Therefore, a novel technique capable of enhancing the ion-diffusion in microsphere templates to fabricate bulk nickel foams needs to be developed. Modeling of the developed process is also required to understand mechanisms of ion diffusion and chemical reaction behaviors in order to optimize the process.

One major application of microcellular nickel foams is the substrate for fabricating 3D graphene foams, which have potential applications in high performance energy storage devices such as lithium-ion batteries and super capacitors. Recent studies have demonstrated 3D graphene foams with pore sizes on the level of several hundreds of micrometers [15-17]. Such a pore size level leads to a relatively low specific surface area and long charge transfer path, resulting in a slow charging/discharging rate for the energy storage device. Graphene foams of nanometer pore sizes were fabricated with a lithographically-defined polymer foam as a template [18]; however, this process is complex and introduces irremovable carbon residue lowering thermal and electrical properties of graphene foams. Bulk

microcellular few layer graphene foams with pore size between 1 and 100 μm need to be developed to balance the requirements of high active material loading and distinct thermal and electrical performances.

1.2 Research Objectives

The goal of this research is to fabricate microcellular metal foams and graphene foams with hydrophilic polymer microsphere assembly and open celled microcellular polymer foam as templates for potential energy storage related applications. Specifically, the following objectives have been identified:

- To develop novel fabricating techniques for hydrophilic polymer foams and microsphere templates with controllable pore size and porosity as metal foam deposition templates;
- To fabricate bulk microcellular nickel foam and graphene foam with hydrophilic polymer templates; and
- To understand the mechanisms of a proposed nickel foam fabrication method through modeling and simulation.

1.3 Organization of this Dissertation

This dissertation is organized into eight chapters. Chapter 1 is an introduction to this study consisting of motivation and objectives. Chapter 2 is a literature review on state-of-the-art fabrication techniques for open celled hydrophilic polymer templates and foams, nickel foams, graphene foams, and existing modeling efforts on eletroless/electro metal deposition methods and ion diffusion phenomena in porous media. In Chapter 3, fabrication of hydrophilic polymer templates using assembly of microspheres is presented. In Chapter 4, solid state foaming of

hydrophilic polymer micro/nano foams is introduced. In Chapter 5, fabrication of nickel micro foams using a novel hybrid electropolishing-electroless deposition method is discussed. Chapter 6 presents a finite difference model for ion diffusion and chemical reaction in porous media to understand the mechanisms of the hybrid process. Chapter 7 discusses the fabrication of 3D few-layer-graphene foam via chemical vapor deposition (CVD) on the obtained Ni foams. Finally, Chapter 8 summarizes the current research and provides recommendations for future work.

Chapter 2. Literature Review

2.1 Hydrophilic Polymer Templates and Foams

Polymer templates are assemblies of polymer micro or nano spheres with specific orders [19]. Methodologies and approaches of assembling them such as suspension evaporation, sedimentation, and compression have been developed [20-22]. After being bonded through thermal or solvent treatment, necking among spheres would be created to connect spheres together and convert the assembled templates to a 3D ordered structure with certain mechanical strength and interconnected interior spaces. The bonded templates find applications in optical devices and templates for fabricating 3D foams of other materials. Among the polymer templates, hydrophilic polymer templates allow easy access of aqueous solutions into their interior space, hence can be applied as templates for fabricating metal foams, the deposition of which requires an aqueous solution. After the removal of polymer templates, the metal left would form 3D foams with a reversed structure of the opal. Hydrophilic polymer templates are one of the main topics of interest in this work for metal foam fabrication.

Polymer foams, which consist of the polymer matrix and open space in the matrix, have attracted numerous attentions in the past decades due to their multiple advantages compared to unfoamed polymer [23]. Polymer foams can be identified to different categories with two different ways. Pore size is one way to identify them. When pore sizes are in the range of 1 μm to 100 μm, polymer foams are defined as microcellular foams, while pore sizes falling in the nanometer range, polymer foams are identified as nanofoams. The other way of characterizing polymer foams is based on interconnectivity among contacting cells. Open celled foams feature

interconnected cells (pores), while close celled foams have disconnected and isolated cells. Figure 2-1 shows morphologies of open and close celled foams. Compared with close celled foams, open celled foams have interconnected interior paths for fluid flow and mass transportation, which may be selective to different matters based on the morphology of the paths and chemical properties of the polymer matrix. Special applications including scaffolds for tissue engineering, templates for fabricating others foams, and filtration applications can be introduced based on the transport property [1, 2]. Among these foams, hydrophilic open-celled polymer foams, which have strong affinity for water, allow the transportation and infiltration of aqueous solutions to their interiors. Since aqueous solutions or mixtures are the media for tissue engineering, drug delivery, and electroless depositions of metal, hydrophilic open-celled polymer foams find many applications in these fields. In addition, hydrophilic open-celled polymer foams also find potential applications as waste water treatment membranes or humidification membranes (selectively allow water vapor penetration but block other gases) owing to their hydrophilic nature. Hydrophilic open celled polymer foams are the other main topic of interest in this work.

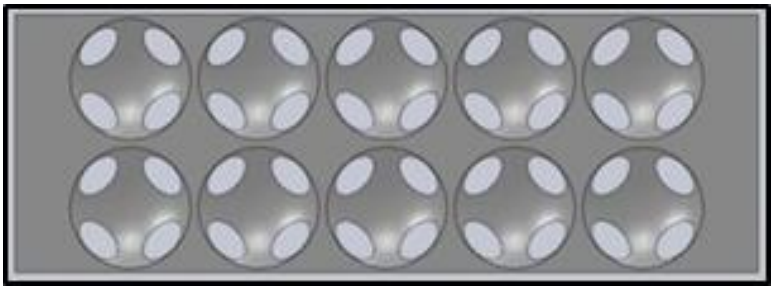

(a)

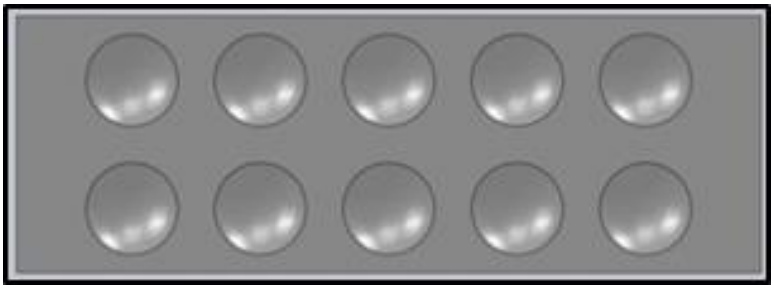

(b)

Figure 2-1. Schematics of (a) an open-celled and (b) a close-celled polymer foam

2.2 Fabrication Techniques for hydrophilic Polymer templates and foams

A number of methodologies have been developed to fabricate porous polymers for applications in metal foam fabrication, filtration, and tissue engineering. These techniques included melt molding and selective leaching, solvent casting and leaching, immiscible polymer blending and extraction, block co-polymer degradation, emulsion polymerization, and solid state foaming of polymer matrix. There are also many methods to create polymer microsphere assembly. A review of these methods is presented in this section.

2.2.1 Fabrication techniques of hydrophilic polymer templates

To fabricate polymer templates, polymer microspheres are assembled into a close-packed structure via specific methods such as suspension evaporation, sedimentation, and compression [22]. Polymer microspheres are dispersed to a liquid initially. The suspension is allowed to evaporate to settle microspheres on a substrate positioned in it. The suspension is also kept at a static environment to allow the microspheres to settle naturally at the bottom of the container. In addition, filters with pores smaller than the microspheres can be applied to remove liquid from the suspension and assembled microspheres. Xiao *et al.* assembled polymer templates with the sedimentation of PS spheres. The porosity of the obtained face-centered-cubic structure is 26% regardless the sphere size, and the pore (space among microspheres) size is around 100 nm determined by the applied spheres of 500 nm in diameter [19]. Zhang *et al.* assembled polymer templates employing an evaporation method with a PS sphere/water suspension. The porosity is also 26% and the pore size is smaller than 100 nm. The drawbacks of this technique include low fabrication efficiency, high complexity, and high cost because of the well-defined polymeric spheres used.

In general, polymer templates with a wide range of porosity (10 – 90%) and pore size (a few nanometers to a hundreds of microns) can be fabricated with the above techniques. However, hydrophilic polymer templates were rarely reported. The hydrophilicity can benefit the diffusion of aqueous metal plating electrolyte into the polymer templates. There is a need for new techniques to enhance the hydrophilicity of polymer templates.

2.2.2 Fabrication techniques of open-celled hydrophilic polymer foams

2.2.2.1 Melt blending and selective leaching

With this technique, polymers were melted and mixed with particles with a device such as an extruder. The mixture can then be shaped with an injection molding machine or a hot press. This technique can be employed without solvent because of the introduction of mechanical mixing. Foams with porosities from 36 to 94% have been fabricated with this technique. Cui *et al.* [24] fabricated hydrophilic polymers foams (up to 64% porosity, 5 μm pore size) from poly(ε-caprolactone) (PCL), poly(ethylene-oxide) (PEO), NaCl, and hydroxyapatite composites. The drawbacks of this technique are that the pore size and shape are determined by the applied salt particles, and that residue salt particles might be trapped in the polymer matrix.

2.2.2.2 Block co-polymers degradation

Block co-polymer is a long chain molecule produced from controlled polymerization of two monomers. The domains of different monomers form two phases when cooled and crystallized. One of the phases is extracted by chemical degradation to result in a nanoporous structure. The pore size formed from this technique is mostly less than 50 nm inherited from the size of the phases. Kang *et al.* [25] fabricated nanoporous hydrogel (water containing hydrophilic or water soluble polymer) using block co-polymer of cross linked PCL-b-PEO-b-PCL. The PCL section was extracted and the resulted pore size is less than 50 nm. The drawback of this technique is the complex procedure and application of multiple chemicals during polymerization and phase extraction. In addition, the hydrogel needs to be kept at a

certain humidity level to maintain its morphology, limiting its applications in low humidity conditions.

2.2.2.3 Emulsion polymerization

In emulsion polymerization of a porous structure, monomers are initially dispersed to a non-solvent and stabilized by surfactants or nanoparticles to form an emulsion with monomers located among non-solvent droplets. The emulsion is polymerized to solidify the monomers, and a porous structure will be formed after removal of the non-solvent [26]. Hua *et al.* fabricated open celled hydrophilic poly(acrylamide) porous structure from polymerization of Titania nanoparticles stabilized acrylamide/water solution in paraffin emulsion [26]. The pore sizes are in the range of 10-200 μm, and the porosities are dependent on the ratio of water and oil phase. The drawbacks of this technique include the use of organic solvent, the complexity of the process, and the problems associated with polymerization and monomer conversion.

2.2.2.4 Solution casting and phase separation

In this approach, polymer solution is cast into a mold featuring a desired shape. A porous structure is induced by phase separation resulting from solution evaporation. Foams with a porosity higher than 50% and 5-15 μm pore size are fabricated with this technique. The drawbacks of this approach include employment of solvents, limited thickness of foams, and existing of solid skin layers. Zhao *et al.* [27] fabricated porous hydrophilic poly(vinylidene fluoride) (PVDF) membranes (porosity > 75% and pore size < 20 μm) via evaporation induced phase separation in PVDF, hyperbranched polyglycerol, and N,N-dimethylacetamide solution.

2.2.2.5 Immiscible polymer blending and extraction

In the process, multiple immiscible polymers are melt-blended with an extruder to generate a co-continuous structure. An interconnected porous structure is formed by selective extraction of one or more phases with a proper solvent. The phase sizes formed from this technique are limited by the high viscosity of polymer and the capability of mechanical stirring, mostly on the level of ten to one hundred micrometers. Hence, the foam pore sizes are on the same level. Virgilio *et al.* [28] fabricated high porosity hydrophilic polymer foams through melt blending and solvent extraction of quaternary ethylene propylene diene rubber/PCL/PS/ploy lactic acid (PLA) composite. A maximum porosity of around 95% and pore size of 5-100 μm were obtained. Sundarram and Jiang *et al.* [29] fabricated high porosity ethylene acrylic acid (EAA) foams via melt processing of blends of EAA and PS. The hydrophilic foams have porosity as high as 55 % and pore size of around 4 μm. Again, this technique is not capable of controlling pore size and porosity of fabricated foams to a wide range.

2.2.2.6 Solid-state foaming of polymer matrix

With the solid-state foaming technique, formation of both micro and nano pore sized polymer foams are induced by bubble nucleation and gas diffusion in a polymer matrix. Thermoplastic polymers are needed due to the requirement of viscosity and flowability change during foaming [30]. The polymer samples with various shapes are initially saturated under a high pressure gas to obtain a certain gas concentration (including equilibrium concentration). Depending on the solubility in polymer matrix, the gas can generally be carbon dioxide or nitrogen. After saturation, the polymer matrix is foamed via nucleation and formation of bubbles

when experiencing a thermodynamic instability, which could be either a sudden increase in temperature or a rapid drop in pressure. The solid-state foaming technique has been applied to many thermoplastic polymers such as PMMA and EAA. Polymer foams with pore sizes ranging from 400 nm to 100 μm and porosity from 10 to 80% have been fabricated applying this technique [30-32]. The major advantage of this technique is its ability of controlling the pore size and porosity of fabricated polymer foams. However, the foams produced with this technique feature a graded structure with mostly closed cells [33-35], and the pore size of foamed polymers are mostly on the micron level. In addition, the gas concentration may decrease in some polymers because of polymer crystallization under a high saturation pressure. The decrease in gas concentration may introduce difficulty in foaming polymers to achieve desired morphology.

2.3 MICROCELLULAR NICKEL FOAMS

Microcellular metal [6] foams are materials with the advantages of both solid metals and those of porous materials [36, 37]. They feature low density, high internal surface area, high electrical conductivity, and high thermal conductivity. As a metal foam, high porosity microcellular nickel foams attract significant attention in recent years due to their potential in emerging applications such as electrodes for high efficiency lithium ion batteries, fuel cells, and nickel-zinc batteries [38, 39]. Nickel foams can also be used as templates for fabricating 3D graphene and ultrathin graphite foams [40-43]. In addition, they can be used as catalyst carriers for more efficient chemical reactions and media for filtering, electromagnetic shielding, and fluid pressure buffering.

Various fabrication methods have been developed [38, 39, 44-61] for nickel foams. These methods include solid-gas eutectic solidification, powder metallurgy, sintering of hollow spheres, mechanical stirring of nickel melt, casting of nickel melt into porous foam, and vapor deposition, electro deposition, and electroless deposition onto polymer templates.

2.3.1 Solid-gas eutectic solidification

In the solid-gas eutectic solidification technique, nickel metal is melted under pressurized hydrogen. After the casting of the gas containing melt to a mold, the trapped hydrogen starts escaping and induces the formation of foam. The pore size is determined by the pressure of hydrogen in the melt, the residue hydrogen pressure during crystallization of nickel and the temperature of molten metal [62]. The disadvantages of this technique include the requirement of a high temperature device, high energy consumption, and the formation of closed cells.

2.3.2 Powder metallurgy

Fine metal powder can be used to form porous metals through the powder metallurgy technique. Generally, fine metal powder and proper spacing powder are mixed together and compression molded to a specific shape and density. The molded blocks are thermally treated to decompose the spacing powder and to sinter the fine metallic powder compact, which forms a porous structure. However, foams fabricated with this technique feature a low porosity. A high temperature operation device is needed and the operation environment may be hazardous [63].

2.3.3 Hollow sphere sintering

Hollow nickel spheres with specific shell thickness have been applied to form porous nickel foams by sintering. The hollow nickel spheres are generally fabricated by depositing metal or coating and sintering metal slurry on polymer spheres [6] [64]. The sizes of hollow metal spheres are determined by the polymer spheres, and are generally in the range of several hundred micrometers to a few millimeters. Hence, hollow sphere sintering results in large pore sizes up to 8 mm.

2.3.4 Mechanical stirring

Nickel foams can be produced from molten nickel by mechanical stirring [44]. A high speed mechanical stirrer can be applied to nickel melt to generate air bubbles. The bubbles can be captured to form pores when the nickel melt is quenched rapidly. This method shows advantages of producing high porosity (90%) nickel foam rapidly in large volumes and with a low cost; however, the foam shows disadvantages of brittleness and big pore size of several hundred microns.

2.3.5 Melt casting

Another technique for fabricating nickel foams is to cast nickel melt into porous foams [44]. Polymeric foams are filled with heat resistant materials such as a mixture of calcium carbonate, phenolic resin and mullite. Nickel melt is cast into the space left by the burned polymer, and nickel foam is obtained by removing the heat resistant material using high pressure water. The limitation of this method is that it can only be used to fabricate nickel foams with large pores due to the difficulty of filling polymeric foams smaller than 100 μm.

2.3.6 Polymer patterning

Nickel foams are also made by depositing nickel on polymer foam templates via vapor deposition, electrodeposition, and electroless deposition. The templates are either foamed polymers or close-packed polymer sphere templates. Nickel foams with inversed structure with polymer templates are produced after the removal of polymer templates via solvent leaching or thermal treatment. The fabricated nickel foams inherit pore size and morphology from the applied templates, hence their porous structure is controllable with the selection of polymer templates [65]. Inorganic templates are not favored because they need to be removed with hazardous acid or base solutions, after the electroplating of nickel foams.

Polymer foams are the main templates for vapor deposition of nickel foams. Polyurethane sponge is an example of foamed polymer used as a substrate for nickel foam fabrication. The pore sizes of these foams range from 200 μm to 4 mm [39, 66]. Commercially available nickel foam, INCOFOAM, is fabricated via chemical vapor deposition on polyurethane foams. However, the vapor deposition technique is only applicable to templates with large pores (several hundred micrometers) owing to the problem of slow vapor diffusion.

Electrodeposition and electroless deposition methods have been used to fabricate smaller pore sized nickel foams compared with the methods discussed above. Brown *et al.* [59] electrodeposited and electroless deposited nickel foams on an open celled polymer foam with a porosity up to 97% and pore size around 20 μm. This process applied polymer templates produced with an emulsion technology, hence provided little control over pore size. Zhang *et al.* fabricated nickel foam via electrodeposition on a polystyrene opal template, in which the sphere diameter is

around 2 μm [54]. However, only a few layers of polymer spheres were assembled and the thickness of the fabricated nickel foam is less than 50 μm.

The fabrication of bulk microcellular nickel foams is challenging, and yet promises many important applications. Efficient methods of fabricating bulk nickel foams with micro pores (1-100 μm) are lacking. Among the many metal foam fabrication methods, electroplating of close-packed sphere templates is considered a promising approach to microcellular nickel foam fabrication due to its ability to control the pore size and to produce highly ordered microstructures [13, 14]. However, as the sphere size or pore size becomes smaller while the overall foam size remains at a bulk level, many challenges arise. For example, the electrodeposition process will be limited by ion-diffusion into the small pore sized polymer templates.

2.4 Modeling of Ion Diffusion in Porous Media and Ni Plating Process

Models regarding principles of both electro- and electroless deposition have been studied extensively in the past. Many theoretical and empirical models have been developed to explain the mechanisms of the process and predict the optimal plating conditions; however, most of the existing models only investigated the plating process on planar surfaces. In those models, the effect of current waveform, frequency, and duty cycle on plated metal structure were studied for electroplating; the effect of electrolyte concentration, composition, and temperature were investigated for electroless plating. A few models studied the metal electroplating employing alternating current in deep wells with micron level diameters, although metal foams have been fabricated with electroplating of polymer nanosphere templates [19]. The ion diffusion models in porous media have also been investigated. However, the correlation between ion diffusion and plated metal

thickness and thickness distribution in porous media does not exist. This section provides a review of analytical and numerical models that have been developed to describe the ion diffusion and electroless metal plating on planar surfaces, and electroplating on both planar surfaces and deep micro wells.

2.4.1 Electroplating models

A number of analytical models have been developed to describe metal electroplating on planar surfaces and in deep micro wells. The models are based on the ion diffusion from electrolyte toward the plating surface and the ion concentration near the surface is regulated by the plating current parameters [45]. In general, the morphology of plated metal is determined by the near surface ion concentration [67]. Wong *et al.* proposed a model to define the surface finish under currents with different waveforms. This model became foundation of many other models that were developed subsequently. The protrusion height of plated metal, h, which affects the surface roughness of plated metal, is defined as,

$$h = h_0 \cdot exp\left\{\frac{i \cdot d}{nzFD[(C_e' - C_e) + m(C_0 - C_e')]}\right\} \quad (2\text{-}1)$$

where h_0 is the initial height of a protrusion, i is the applied current density above the protrusion, d is the thickness of the formed metal underneath the protrusion, n and m are unit-less numbers decided by the shape of current waveform, z is the number of electron transferred when reducing one metal ion, F is Faraday's constant, D is a constant diffusion coefficient in the cases of both planar surface and deep well, C_0 is bulk ion concentration, C_e is the interfacial ion concentration on the

border of bulk electrolyte and diffusion layer, C_e' is the ion concentration near the plating surface.

Chung [68] provided an equation to relate the ion flux toward plating surface to the ion concentration at the plating surface.

$$\frac{C_e'}{C_0} = 1 - \frac{8\delta}{\pi^2 zFDC_0} \sum_{n=0}^{\infty} \frac{1}{(2n-1)^2} \times \left\{ i \cdot \frac{1-exp[x_1 \cdot T/(r+1)]}{1-exp[x_1 \cdot T]} \right\} \quad (2\text{-}2)$$

where δ is the diffusion layer thickness decided by stirring rate of electrolyte and D, x_1 is a constant decided by δ and D, T is the operation temperature, and r is duty cycle of applied current. The ion flux toward plating surface can be expressed as

$$J = \frac{i}{zFD} \quad (2\text{-}3)$$

2.4.2 Electroless plating on planar surfaces

A few studies have been performed to investigate the effect of electroless plating condition on surface finish. Mallory *et al.* [69] developed a model to describe the electroless nickel plating rate under different electrolytes and conditions as

$$r = e \cdot k \cdot \frac{[\ H_2PO_2^{-}]}{[H^+]^{0.4}} \quad (2\text{-}4)$$

$$e = exp(-\frac{E_a}{360R}) \cdot exp(\frac{E_a}{360R} \cdot \frac{T-360}{T}) \quad (2\text{-}5)$$

where k represents the reaction rate constant, $[\ H_2PO_2^{-}]$ and $[H^+]$ are ion concentrations, and e is an energy term, E_a in Equation (2-5) is the activation energy of the reaction, R is the idea gas constant, and T is the absolute temperature.

2.4.3 Ion diffusion in porous media

A number of analytical models regarding ion diffusion in porous media have also been established [9]. Yu *et al.* [21] developed a model to describe the tortuosity in porous media, which represents the difficulty of ion diffusion in porous media. A correlation between tortuosity and porosity was established and expressed as the following,

$$\tau = 0.5\left(1 + \sqrt{1-\phi}\right) + \frac{\sqrt{\left(\frac{1}{\sqrt{1-\phi}}-1\right)^2+0.25}}{1-\sqrt{1-\phi}} \tag{2-6}$$

where ϕ is the porosity of a material.

A model of calculating the diffusion coefficient in a porous media was proposed [70]. Diffusion coefficient in a face centered cubic structure was decided by porosity and tortuosity of the material as shown in the following equation,

$$D = D_0 \cdot \left(\frac{\phi}{\tau}\right) \tag{2-7}$$

where D_0 is the diffusion coefficient in bulk solution. This model was validated by a voltammetric scanning method. One side of the porous material was attached to an electrode and submerged in an electrolyte bath, a scanning current was applied and the relationship between the peak current density and scanning speed was established as shown in Equation (2-8). The slope of the peak current and scanning rate plot is the diffusion coefficient.

$$i_p/A = 0.4463nFC(nF/RT)^{1/2}v^{1/2}D^{1/2} \tag{2-8}$$

In Equation (2-8), *n* is the number of electron transferred when reducing one metal ion, *F* is Faraday's constant, *C* is the ion concentration in bulk electrolyte, *R* is molar gas constant, *T* is temperature, and *v* is scanning rate.

As seen in the review above, the developed models do not consider the electroplating and electroless plating in porous media. This study builds upon the reviewed work by combining the ion diffusion in porous media and electroless/electroplating reaction mechanisms to understand electropolishing assisted electroless metal plating in porous media.

2.5 Fabrication of 3D Graphene Foams

3D graphene foams are currently under intense study because of their high electrical and thermal conductivities and the lightweight property [13, 14, 15, 16]. Batteries with dramatically improved performance with such graphitic electrodes have been envisioned [11, 14].

Currently 3D graphene foams and graphitic foams have been fabricated through chemical vapor deposition (CVD) on commercially available Ni foams and surface modified commercial Ni foams [12, 17, 18, 19]. The drawback of these foams is their relatively low specific surface areas inherited from the commercial Ni foam templates, which have pore sizes on the level of several hundred micrometers. On the other hand, nanocellular nickel foams have been recently fabricated with a sphere-template electrodeposition method [20, 21, 22, 23]. However, the method itself is limited by the Ni ion diffusivity in the narrow channels [22, 24]. As a result, the foams that were demonstrated had only a few layers of pores and the overall thickness was only a few micrometers. In addition, large cracks occur in plane about every 50 μm in the obtained foams. More importantly, Ni foams with pore sizes smaller than 20 μm have shown insufficient thermal stability at the temperature required for graphite/graphene formation [25, 26] in CVD fabrication process.

Three-dimensional graphene foams of pore size smaller than a few microns have been fabricated using the self-assembly of polystyrene (PS) sphere and graphene oxide via an infiltration approach [27]. Graphene oxide and PS spheres were dispersed in a solution separately followed by the infiltration of both dispersions through a filter. Graphene oxide was reduced and pH was controlled to form a PS embedded graphene film. 3D porous graphene foam was obtained after the solvent leaching off of PS. The limitation of this technique is the lack of control over interstitial openings (channels) of the graphene foam, because there is no sintering of PS or following enlarging process of the openings. Narrow openings may lead to low mass transport capacity. Xiao *et al.* fabricated nano graphene foam employing a lithographically produced carbon foam [28]. 3D porous carbon foam was fabricated by patterning a photoresist polymer followed by a hydrolyzing step. The 3D porous carbon foam was sputter-coated with Ni and then converted to graphene by annealing the C/Ni composite and etching off of Ni afterward. The limitation of this approach is the depth in the carbon foam reachable by sputter coating. Electrodeposition may potentially provide thick Ni coated carbon foam; however, the removal of carbon substrate remains a problem. The remaining carbon substrate may result in a high density and low electrical and thermal properties of obtained graphene foam. Overall, the fabrication of bulk 3D graphene foams with high specific surface area, high mass transport capacity, and low fabrication complexity is still challenging.

Chapter 3. Hydrophilic Polymer Microsphere Templates

3.1 INTRODUCTION

Polymer templates assembled with microsphere is a three-dimensional periodic structure. As described in Chapter 2, it emerged as an important system due to its potentials in optical and biomedical applications and as templates of inverse microcellular structure for metal foam fabrication [71]. A variety of techniques exist to fabricate polymer microsphere templates such as gravitational sedimentation, centrifugation, vertical deposition, slit fitting or pressing of microspheres in molds, and assembly of microspheres on liquid surface [72]. Those techniques show capability of fabricating polymer microsphere templates with sphere diameter of 10 nm to 2 μm and a thickness up to 30 μm. However, in some applications such as the fabrication of metal foams, the polymer templates applied as templates are required to feature hydrophilicity to enhance the aqueous solution diffusivity in templates.

In this chapter, techniques of fabricating hydrophilic paraffin spheres and PMMA spheres are presented. The assembly of hydrophilic polymer microsphere templates is also discussed. The major advantage of this technique is that hydrophilic foams with different sized microspheres can be assembled efficiently and pore sizes are controllable via selection of microspheres. Hydrophilic paraffin microspheres were fabricated with an oil/water emulsion. PMMA microspheres were hydrolyzed using aqueous acid solution. Paraffin, PMMA, and commercial hydrophilic ethylene acrylic acid (EAA) microspheres were assembled into bulk polymer templates via a compression molding, a sonication assisted sedimentation , and an efficient filtration approach, respectively.

3.2 EXPERIMENTAL

3.2.1 Materials

Ethylene acrylic acid (EAA) microspheres (Kobb Inc.) were selected as one candidate material for opal making due to their low cost (compared with hydro group decorated polystyrene microspheres), hydrophilic property (ensuring a high degree of uptake of the electroplating solution), good morphology (spherical shape and smooth surface), and small sizes ranging from 1 to 10 μm. Paraffin and Sodium Aliphatate (Amazon) were applied as raw materials to fabricate hydrophilic paraffin microspheres. Polyvinyl alcohol (PVA) was purchased from Fisher Scientific Inc. Poly methyl methacrylate (PMMA) (Sigma Aldrich Inc.) microspheres were selected to assemble PMMA templates due to their low cost and ability of being hydrolyzed.

The molecular structures of EAA, paraffin and PMMA are shown in Figure 3-1 and their properties summarized in Table 3-1.

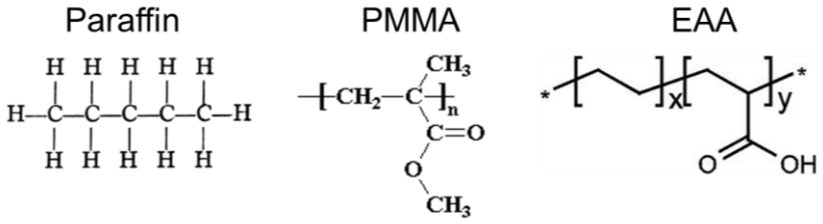

Figure 3-1. Molecular structures of paraffin, PMMA, and EAA

Table 3-1. Properties of paraffin, PMMA, and EAA

Property	paraffin	PMMA	EAA
Density (g cm^{-3})	0.9	1.18	0.938
Melting temperature (ºC)	45-60	160	101
Contact angle with water (°)	109	85.4	69.1

3.2.2 Fabrication of hydrophilic paraffin microspheres

Hydrophilic paraffin microspheres were fabricated using an oil in water emulsion method. PVA was applied as a surfactant and dissolved in deionized water to make a 0.5% (g/ml) solution. The PVA solution was heated to 70 °C under a stirring condition of 600 rpm (IKA RW20 mechanical stirrer). Paraffin and Sodium Aliphatate were melt-mixed under magnetic stirring in a glass beaker at 210 °C on a magnetic stirrer hot plate (Cole-Parmer Instrument, Model 4803-00). The mixture was added into the PVA solution and stirred for 30 min under 1000 rpm. Ice-cold water was added into the stirred suspension to solidify the paraffin spheres. The suspension was poured into a sieve with a pore size of 40 μm to filter away smaller spheres. The paraffin microspheres were then washed with deionized water three times and transferred to a piece of filter paper. The spheres were dried in air for 3 days.

Table 3-2. Parameters for fabricating paraffin microspheres

Sample	Sodium Aliphatate (%)	Melting T (°C)
1	5	210
2	10	210
3	20	210

3.2.3 Hydrolyzation of PMMA microspheres

As sphere sizes go below 100 μm, the separation of spheres becomes challenging. Several methods have been proposed including viscous liquid separation, laminar fluid separation, and centrifuge separation [73, 74]. When employed, these methods either need a liquid system having a specific viscosity or specifically designed devices. In this study, we employed metallic sieves with opening sizes of 53, 63, 75, 90, and 105 μm (H&C Sieving Systems, Inc.) for spheres sorting. Separation was operated at room temperature (25 °C) in sieves submerged in an ultrasonic water bath. After separation in one sieve, the spheres in ultrasonic bath are filtered out and transferred to another sieve with a smaller mesh size. Spheres falling into different grades are dehydrated and stored separately.

To gain hydrophilicity, PMMA spheres was etched using a sulfuric acid based solution ($K_2Cr_2O_7$ 10%, water 25%, H_2SO_4 65%, 10M). To ensure wettability of PMMA spheres in the sulfuric acid based solution, PMMA spheres were wetted with ethanol followed by rinsing of DI water. The PMMA spheres were then dispersed into a sulfuric acid solution preheated to 50 °C and etched for 30 min. $K_2Cr_2O_7$ and H_2SO_4 are strong oxidants and can introduce hydroxyl groups to PMMA surface [75].

3.2.4 Assembly of hydrophilic polymer templates with spheres

Three different methods are used to fabricate EAA, paraffin and PMMA templates due to their different characteristics. For EAA, the microspheres are deposited to form templates by an efficient filtering method, because EAA microspheres tend to float on water surface but deposit naturally. EAA spheres are dispersed into deionized water to form a 2%–5% (g/ml) suspension. The mixture is then feed into a device shown in Figure 3-2 (top) using a 10 ml plastic syringe. Several layers of filter paper are placed at the bottom of a plastic tube. Water is extracted through the bottom paper filter, and the extracting process is accelerated by applying vacuum. Thickness of EAA templates can be controlled by the feeding volume. In this work, templates with a thickness of 3 mm and a diameter of 26 mm are obtained with a fabrication time of 1 hour. After dehydrated at room temperature to remove water, the templates are sintered at 110 °C in a vacuum oven (MTI EQ-DZF-6020). The sintering time varies with the thickness of the template.

Paraffin microspheres are made into templates with an aluminum mold with a diameter of 20 mm. The mold is then vibrated for 15 min on a vibrating table to settle paraffin spheres to their favorite positions. The sample is sintered at 40 °C in a vacuum oven. The sintering time varies to tune the bonding strength among spheres.

PMMA microspheres are assembled to templates by employing an ultra-sonication assisted sedimentation approach. PMMA microspheres are loaded to a mold consisting of two pieces of glass slides and a silicon rubber gasket. Ethanol is added to function as both lubricant and suspending media of the PMMA sedimentation. The mold is positioned in an ultra-sonication bath for 1 h at 25 °C. The mold is then kept at ambient to allow the evaporation of ethanol. The mold is

then sintered at 190 °C in a vacuum oven. The sintering time is tuned to achieve different bonding level.

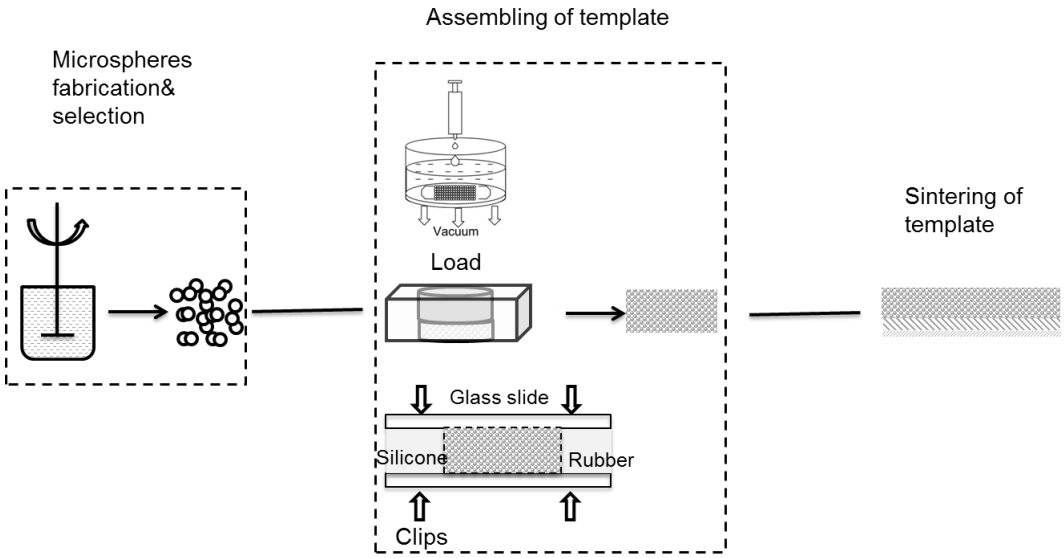

Figure 3-2. Schematic of microsphere assembly

3.2.5 Characterization

The hydrophilicity of modified paraffin and PMMA were measured with a water contact angle goniometer (Vlino SL150). The hydrophilicity was represented with measured water contact angle. Paraffin films with the same compositions paraffin spheres and PMMA films modified under the described conditions were applied to ease the measurement. The fabricate paraffin spheres and sieved PMMA spheres were examined with a JEOL NeoScope 5000 scanning electron microscope (SEM), and their distribution was analyzed employing software Image J. The cross sections of the samples were observed with a JEOL NeoScope 5000 scanning electron microscope (SEM) to study the effect of each processing step. The pore sizes were determined from the SEM images using software Image J. The porosity of

the foamed blends was determined by an ethanol absorption method. The weight of foams was measured initially. The templates were submerged in ethanol for 5 min to allow the full saturation of ethanol. The templates were then removed from ethanol and the ethanol on their surface was cleared carefully. The total weight of templates and absorbed ethanol were measured. Porosities of templates were calculated using the following equation.

$$\varepsilon = \frac{(W_{total} - W_{template})/\rho_{ethanol}}{(W_{total} - W_{template})/\rho_{ethanol} + W_{template}/\rho_{template}} \quad (3\text{-}1)$$

where W_{total} is the weight of template and absorbed ethanol, $W_{template}$ is the weight of the template, $\rho_{template}$ is the density of template, and $\rho_{ethanol}$ is the density of ethanol.

3.3 Results and Discussion

3.3.1 Paraffin

Figure 3-3 shows the results of water contact test of hydrolyzed paraffin. Pure paraffin shows a high water contact angle of 109 º indicating its hydrophobic nature. The water contact angle decreased with increasing sodium content. Samples with three levels of Sodium Aliphatate are hydrophilic (<90 º).

The morphology and size distribution of paraffin microspheres from different conditions are shown in Figure 3-4. It can found that 5 wt% Sodium Aliphatate content resulted in spheres with rough surface and wide size distribution, while the 10 wt% and 20 wt% contents resulted in spheres with smoother surface and relatively narrower size distribution. The yield of paraffin spheres with size of 50-60 μm were measured and listed in Table 3-3. The yield decreased with increasing

Sodium Aliphatate content. 10 wt% was selected for paraffin microsphere fabrication due to its balance of sphere morphology, size distribution, water contact angle and yield.

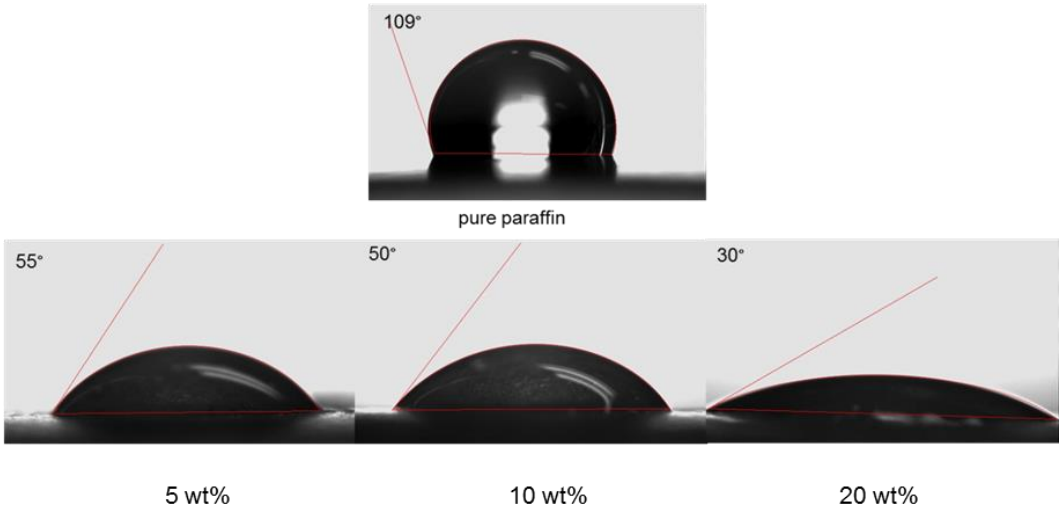

Figure 3-3. Water contact angles of paraffin microspheres with 5%, 10%, and 20% sodium aliphatate

Table 3-3. Yield of paraffin microspheres fabricated under different conditions (size of 50-60 μm)

Batch #	Sodium Aliphatate (wt%)	Percentage (%) in range	Yield (g/2.0g raw material)
1	5	63	0.41
2	10	75	0.34
3	20	88	0.12

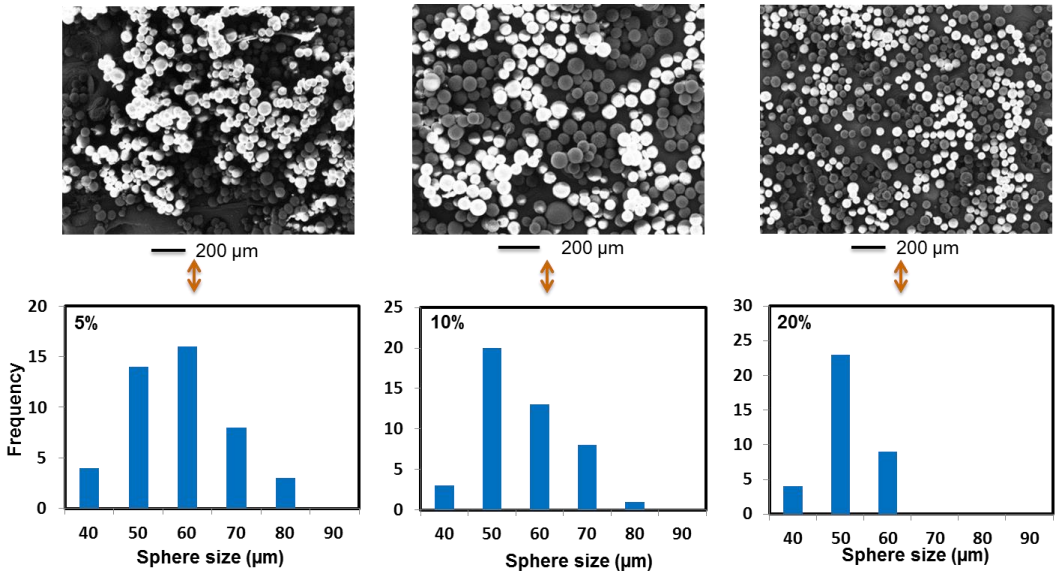

Figure 3-4. Sphere sizes and distributions of paraffin microspheres with 5%, 10%, and 20% sodium aliphatate

Paraffin templates were fabricated using spheres containing 10% sodium aliphatate by the procedure described in Section 3.2.4. The obtained templates were sintered in a two-step procedure to reduce the entire sintering time. In the first step, template was kept in an aluminum mold and sintered for 1.7 h at 40 °C to remove residue water. The template was then transferred onto a piece of aluminum foil (provide a faster heat transfer) and sintered for a specific time. The porosities of templates with different sintering time were calculated using the method described in Equation (3-1). SEM images were not taken from sintered paraffin templates, because the paraffin spheres would melt during the sputter coating process. Theoretically the porosity of a tightly packed face centered cubic structure is 26%. The template sintered on Al foil for 10 min shows a porosity of 35.1%. This is because the used paraffin spheres are not highly uniform. The porosity data in Table 3-4 indicate that the spheres sintered on Al foil longer than 20 min are likely bonded

(porosity decreased from 35.1% to 29.2%). The template with a sintering time of 25 min was selected for potential metal plating substrate due to the easy penetration of electroplating solution and its integrity in electroplating solution. As can be seen in Figure 3-5, the electroplating solution has completely infiltrated the template, exhibiting a greenish color of the solution.

Table 3-4. Porosity of paraffin foams sintered for different time

Sintering time in mold (h)	Sintering time on Al foil (min)	Porosity (%)
1.7	10	35.1
1.7	20	29.2
1.7	25	22.5
1.7	40	14

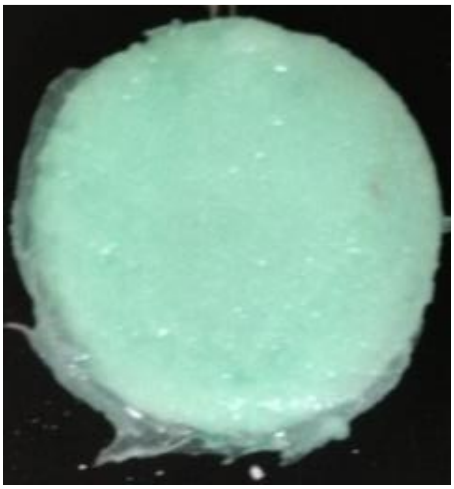

Figure 3-5. Paraffin template soaked in electroplating solution (25 min on Al foil)

3.3.2 PMMA

PMMA spheres are separated with sieves having 53, 63, 75, 90, and 105 µm holes. The separated spheres fall between each grade. After being dehydrated, each grade is examined using SEM. Sphere size distribution of each grade is analyzed using the image processing software, Image J. The spheres in 105 µm range take the highest portion of 50% out of all the PMMA spheres, and distribute mainly between 90 and 105 µm. Hence, this grade was selected to fabricate foams because of a balance between yield and homogeneousness. Figure 3-6 demonstrates the spheres and their distribution.

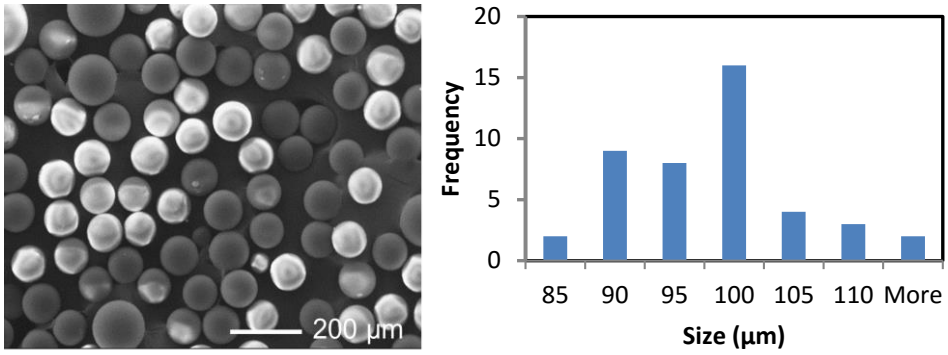

Figure 3-6. PMMA spheres (90-105 µm) image and size distribution

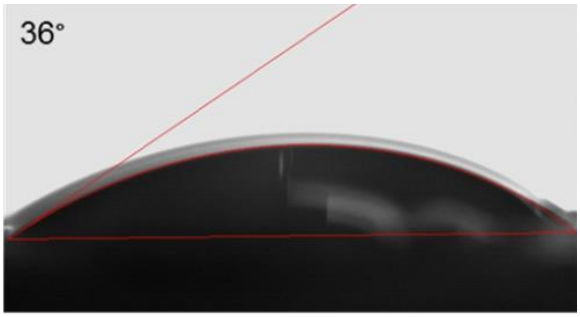

Figure 3-7. Water contact angle of hydrolyzed PMMA

Figure 3-7 shows the water contact angle of sulfuric acid hydrolyzed PMMA, a PMMA film was used instead of the PMMA spheres to ease the measurement. The water contact angle of 36 º indicates the hydrophilicity of hydrolyzed PMMA. After being assembled and dried, PMMA templates were sintered at 190 °C for 3 h and 5 h respectively. As shown in Figure 3-8, PMMA spheres were properly bonded together after 3 h and obtained necking of around 50 μm; as a contrast, a portion of PMMA spheres were melt and lost their spherical morphology after being sintered for 5 h. A proper bonding is needed to maintain the mechanical strength of PMMA opal and spherical shape is needed for an ordered interior structure.

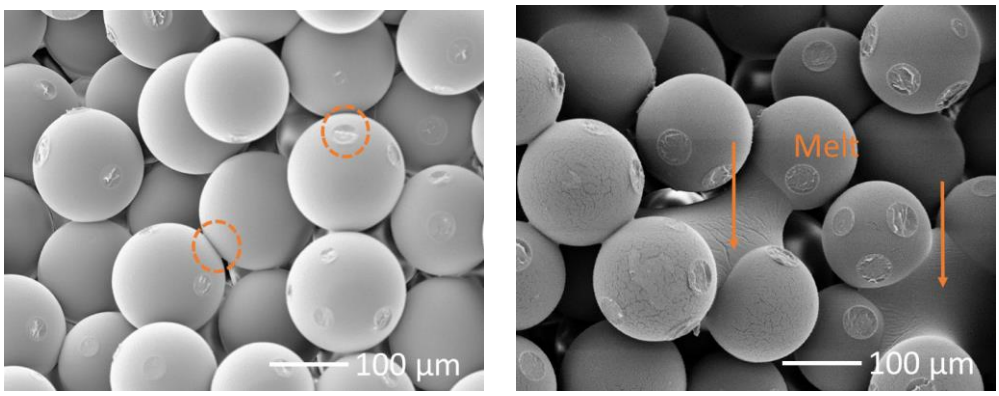

(a) (b)

Figure 3-8. Hydrolyzed PMMA sphere templates sintered at 190 °C for (a) 3 h and (b) 5 h

3.3.3 EAA

Obtained EAA templates were sintered at 110 °C to enhance the bonding strength among EAA spheres inside the templates. Four different sintering times of 1, 3, 5, and 8 min were applied. Figure 3-9 shows SEM images of the samples

sintered with these four sintering times. From Figure 3-9(a), bonding among EAA spheres is not observed. The bonding is still not obvious. After the EAA template was sintered for 5 min, more heat could be transferred into the template, such that more bonding was formed. After the EAA template was sintered for 8 min, almost all the EAA spheres were bonded. The porosities of the sintered templates were calculated using the method described above and are listed in Table 3-5. The porosity decreased with the increasing sintering time. A low porosity represents a tightly bonded template. The templates with a 5 min sintering time were selected for the potential application of fabricating nickel foam due to the proper amounts of bonding among spheres in these templates, which make the templates strong enough to withstand handling in the process, while maintaining a high diffusion rate of aqueous solution like Ni plating electrolyte. The templates sintered for 3 min would collapse under vacuum, and electroplating solution could not enter the templates sintered for 8 min.

Table 3-5. Porosity of EAA templates sintered under different time

Sintering (min)	Porosity (%)
1	16.1
3	13.4
5	9.8
8	5.3

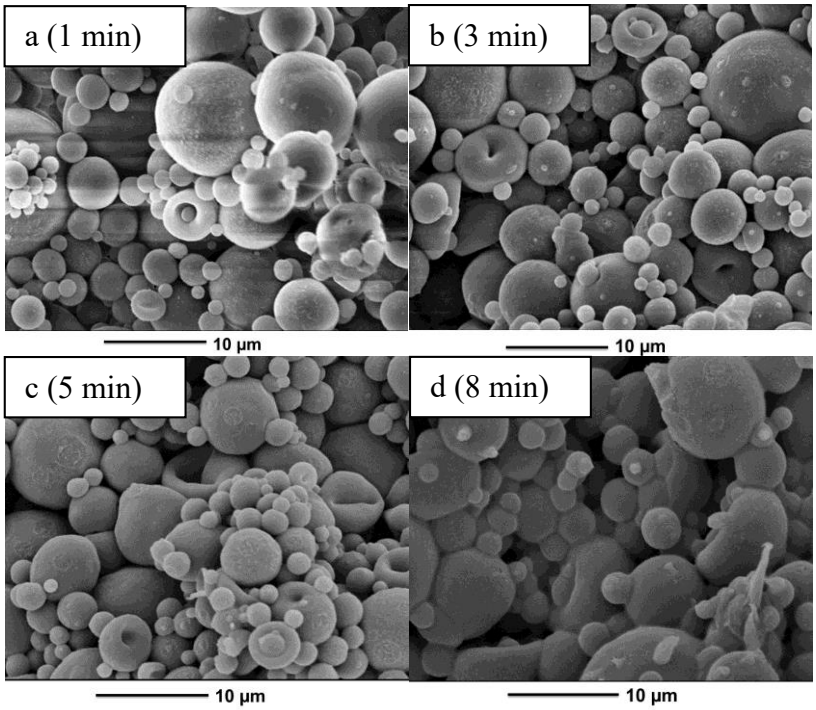

Figure 3-9. The SEM images of EAA templates sintered for different time

3.4 CONCLUSIONS

Three kinds of hydrophilic polymer microspheres with different size ranges were fabricated or selected to fulfill the assembly of hydrophilic polymer templates with different internal opening sizes. Hydrophilic paraffin microspheres with a size range of 50-60 μm were fabricated using a PVA stabilized Sodium Aliphatate and paraffin/water emulsion. 10 wt% Sodium Aliphatate resulted in a balance between paraffin sphere size distribution, yield, and hydrophilicity. PMMA microspheres were separated by applying sieves. PMMA microspheres with a size range of 90-105 μm were hydrolyzed with a simple H_2SO_4 aqueous solution to gain a water contact angle of 36º. Paraffin, EAA, and PMMA microspheres were assembled into bulk hydrophilic polymer templates via a compression molding, a sonication assisted

sedimentation, and an efficient filtration approach. The templates were sintered under different conditions to introduce bonding to spheres while maintaining specific porosities. Process conditions of 40 °C and 25 min, 110 °C and 5 min, and 190 °C and 3 h were chosen for paraffin, EAA, and PMMA assemblies, respectively.

Chapter 4. Hydrophilic Poly(ethylene glycol)/Disulfonated Poly(arylene ether sulfone) Micro/nano Foams

4.1 INTRODUCTION

Hydrophilic polymer micro and nano foams are critically important for many infiltration and separation related applications. As described in the Introduction chapter, the existing fabrications of hydrophilic polymer foams are either complex or involving environmental hazardous chemicals. In addition, the foams fabricated are mostly micro cellular foams with pore sizes of hundreds of microns. An efficient and clean way of producing those foams is missing.

One important potential application of hydrophilic polymer foams is humidification membranes for fuel cell. The humidification membrane is designed to humidify the PEM using the exhaust gas of fuel cell [76]. The maintenance of proper water content in the PEM is important for its performance. Currently, most humidification membranes are made of Nafion (sulfonated tetrafluoroethylene based fluoropolymer-copolymer), and are of high cost because of the difficulty of Nafion fabrication. Alternatives with low cost, easy fabrication, and comparable performance with Nafion are needed.

Polymer blends of random disulfonated poly(arylene ether sulfone) copolymer (BPS) and hydroxyl-terminated poly(ethylene glycol) have found widespread use as waste water treatment and water desalination membranes owing to their highly hydrophilic nature and high water permeability [77]. The properties of these membranes can be tuned according to the requirements by suitable combination of different BPS and PEG contents. Lee *et al.* [78] first reported the water permeability performance of PEG/BPS membranes. Subsequently, a variety of

PEG/BPS blends have been fabricated via an efficient solvent free extrusion method and the membranes have exhibited good water treatment performance. Considering the high molecular weight of BPS matrix (MW 33900) and fully amorphous of BPS [79], such a blend could be foamed in order to make it lightweight, with added benefit of a low thermal conductivity, and potentially high water permeability if open cells were formed. The porous structure of foamed PEG/BPS could be tuned by controlling foaming process parameters to optimize their performance for humidification applications.

This chapter presents the fabrication and evaluation of foamed PEG/BPS as humidification membrane for fuel cell applications. BPS is chosen as the matrix material. PEG, miscible with BPS, is used as the plasticizing additive. The PEG/BPS miscible blend with various loading ratios were foamed using a solid state foaming process under different saturation and foaming conditions. The morphology of foamed samples was characterized with SEM. Foamed samples were subjected to a water permeability test to characterize the humidification performance with an in-house built measurement system. The results were further analyzed according to the material composition and foaming condition.

4.2 EXPERIMENTAL

4.2.1 Materials

The disulfonated poly(arylene ether sulfone) random copolymers (BPS) were prepared by direct aromatic nucleophilic substitution step polymerization as described by McGrath [80]. The BPS polymer applied in this work is BPS-20K synthesized in potassium form by Akron Polymer Systems (Akron, OH) employing McGrath's approach. In the nomenclature BPS-20K, 20 represents 20 mol % of

sulfone groups in the polymer, and K indicates that the type of cation is potassium. The chemical structure of BPS is illustrated in Figure 4-1. BPS-20K (MW 33900 g/mol) is selected in this study owing to its higher thermal stability (decomposes at ~400 °C) than BPS-20H (decomposes at ~230 °C, H indicates hydrogen cation) according to the research of Oh [79]. Considering the processing difficulty resulted from brittleness of BPS [79], a polymer plasticizer was introduced to the system. Poly(ethylene glycol) (PEG) was selected as a plasticizer because PEG was reported to be miscible with BPS [80], which will not result in the one to several hundred micrometer-level domains as those in immiscible polymer blends. Big domains will affect the control of pore size during solid state foaming or phase extraction of the blends. In addition, PEG has good water solubility, hence will enhance the water permeability in the PEG/BPS blends. PEGs with two different molecular weights were purchased from Sigma Aldrich [79]. The properties of PEGs are listed in Table 4-1.

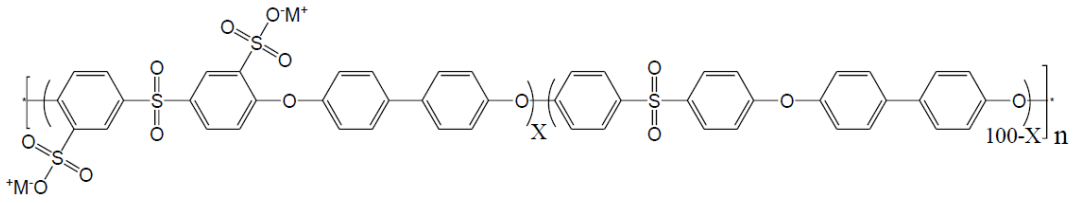

Figure 4-1. (a) Chemical structure of BPS, X is mole portion of disulfonated monomer, M refers to either K or H [79], (b) chemical structure of PEG

Table 4-1. PEG properties

Name	$\bar{Mn}$ (g/mol)	T_g (°C)	T_m (°C)
PEG 200	200	-83	-
PEG 600	600	-69	17

The PEG/BPS blends used in this study had compositions shown in Table 4-2 and were melt extruded to thin membranes [79]. The procedure can be illustrated briefly as the following. Specific amounts of BPS and PEG were premixed well. A 5 mL twin screw extruder (DSM Xplore, the Netherlands) equipped with a film die was then heated to a temperature range of 170-245 °C, which is 50-100 °C higher than the glass transfer temperature (T_g) of the blend and lower than its degradation temperature (T_d). Under the protection of an ultra-dry nitrogen atmosphere (99.9 %, Matheson Tri-Gas, Tx), the blend was mixed and extruded to thin films. Film thickness can be controlled with the tunable speed and torque of the film take-up unit. The T_g and T_d values of obtained PEG/BPS blends were tested by Oh [79] and applied in this work. For humidification performance comparison, Nafion 212 humidification membrane was purchased from DuPont and used as received.

Table 4-2. PEG/BPS membrane properties

Sample ID	PEG (w%)	Tg (°C)	Thickness (mm)
PEG 200-20	20	115-135	210 ± 3
PEG 200-30	30	55-85	210± 3
PEG 600-20	20	122-147	230 ± 3
PEG 600-30	30	64-94	225± 3

4.2.2 Solid State Foaming

The solid state foaming of a polymer matrix consists of three major steps, which are the saturation, desorption, and foaming as shown in Figure 4-2.

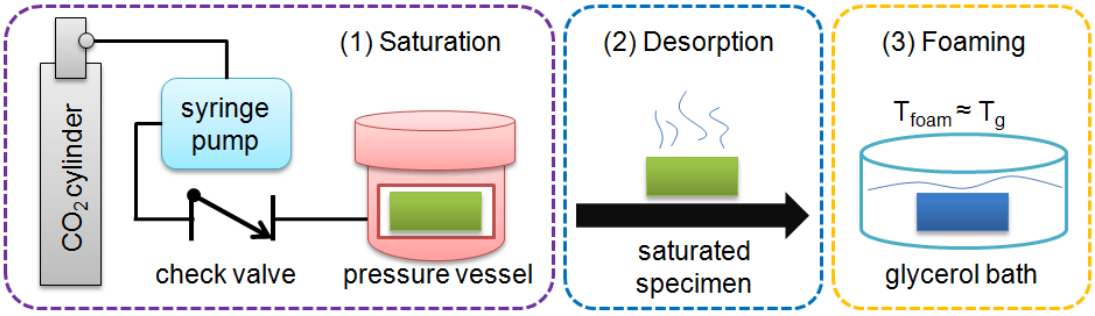

Figure 4-2. Schematic of the solid state foaming method

The specimens were first saturated with CO_2 in a high pressure vessel until the equilibrium (maximum gas concentration in polymer matrix) was achieved. The high pressure vessel (Parker Autoclave Engineers Zipperclave) and syringe pump (Teledyne Model 260D) applied in this work are shown in Figure 4-3. Two batches of PEG/BPS samples were saturated in the high pressure vessel controlled by a syringe pump under the saturation conditions shown in Table 4-3. Different

saturation conditions were used in order to determine the ideal parameters for achieving the equilibrium gas concentration in a short time possible. As seen from the phase diagram of carbon dioxide shown in Figure 4-4, at a temperature of 31 °C and a pressure above 72.9 bar (7.39 MPa) from carbon dioxide becomes a supercritical fluid. It is known that supercritical CO_2 has high diffusivities in polymers but may reduce the equilibrium gas concentration. A low equilibrium gas concentration may result in large pore size and lower porosity during foaming. Hence, subcritical saturation is applied in this work. The CO_2 concentrations in the specimens were measured at regular time intervals till achievement of equilibrium.

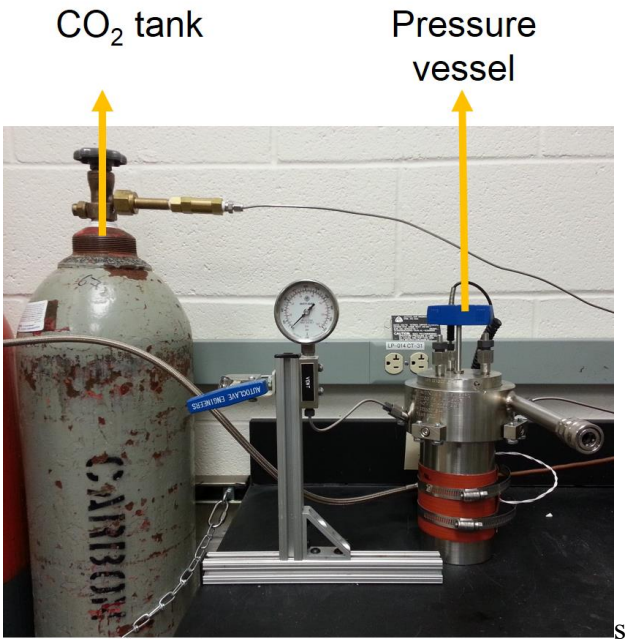

Figure 4-3. High pressure vessel and syringe pump

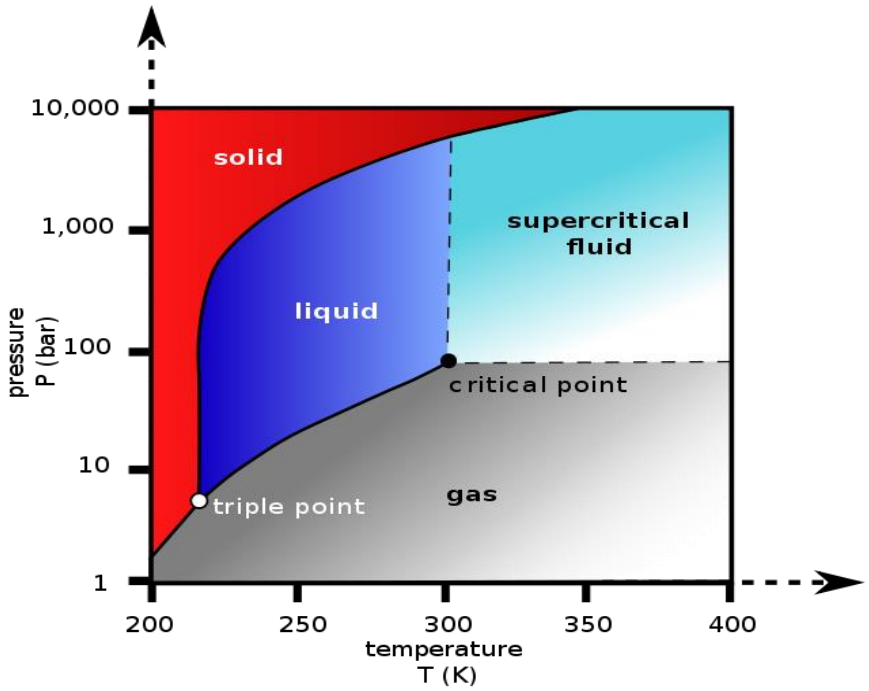

Figure 4-4. Phase diagram of carbon dioxide [81]

Table 4-3. Saturation condition of PEG/BPS samples

Batch	Pressure (MPa)	Temperature (ºC)	Condition	Duration (hours)
1	10	23	Subcritical	100
2	5	23	Subcritical	240

The saturated specimens were then retrieved from the pressure vessel and left in the ambient environment for desorption for a controlled time of 15 min. A fixture to constrain the samples during foaming to ensure flatness was designed and built as shown in Figure 4-5. Samples were foamed using this fixture. The desorbed samples were subsequently heated in a glycerol bath (Fisher Scientific) resulting in the

formation of the porous structure. The glycerol foaming bath setup is shown in Figure 4-6.

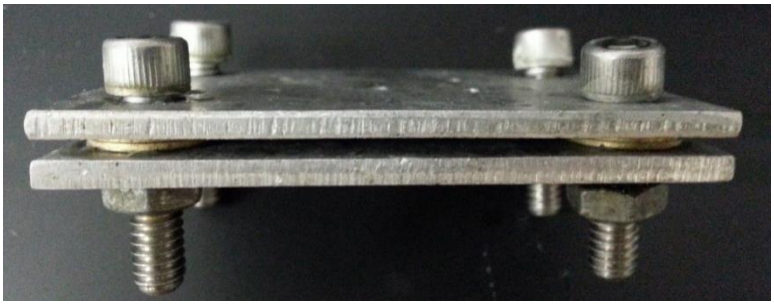

Figure 4-5. Fixture for ensuring flatness of samples during foaming

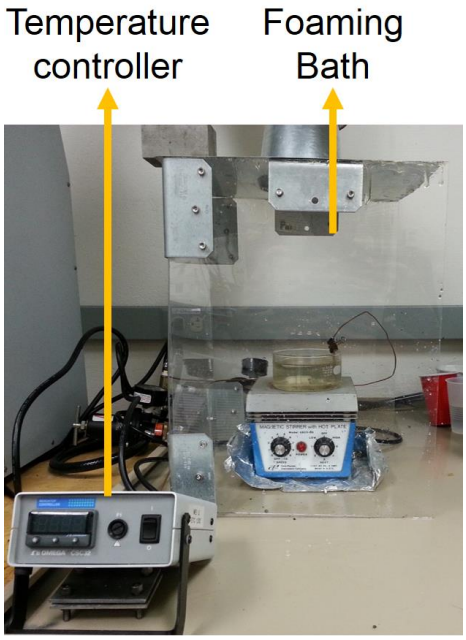

Figure 4-6. Glycerol foaming bath setup

4.2.3 Characterization

Foamed samples were freeze-fractured and the microstructures were examined with a Quanta 650 FEG scanning electron microscope (SEM). The cross

sectional surfaces were sputter coated for 30 seconds with gold/palladium alloy. ImageJ was used to determine the average pore size. The average density of the foamed samples was determined according to ASTM D-792 standard [82] using the following equation.

$$\rho = \frac{\rho_w * W_a}{(W_a - W_w)} \tag{4-1}$$

where ρ = the relative density of sample;

ρ_w = the density of non-solvent at room temperature (25ºC);

W_a = the mass of sample in air at room temperature;

W_w = the mass of sample in a non-solvent (mineral oil) at room temperature.

The water humidification performance of the unfoamed and foamed PEG/BPS samples was evaluated using a test chamber with humidity and temperature control constructed in house, as shown in Figure 4-7. The setup was calibrated with Nafion of known permeability [82]. The principle of the humidification test is also illustrated in the schematic in Figure 4-7. In general, the membrane was initially conditioned at 30% relative humidity and 25 ºC for at least three days and then mounted onto a sealed test chamber located in an environmental control chamber. The test chamber was then circulated with compressed air (10 Psi) for 3 h to bring the interior relative humidity to 6% and dry the membrane. The humidity chamber was then set to a test condition, and the test would start after stopping the circulating air and shutting off valves. The test environment in the

environmental chamber was set at 95% relative humidity and 30 ºC. The test time was set at 10 h.

The air barrier analysis of foamed membranes was conducted using the same test device. Air was fed in the test chamber initially. When the pressure reached to 5 Psi the valves of air inlet and outlet were shut off. The pressure change in the test chamber was monitored with a pressure transducer continuously for 10 h at 25 ºC. The air leaking rate was calculated using the ideal gas law.

$$P \cdot V = n \cdot R \cdot T$$

$$\frac{P_2}{P_1} = \frac{n_2}{n_1}$$

$$\Delta n = n_1 - n_2 \qquad (4\text{-}2)$$

where P = system pressure;

V = system volume;

R = ideal gas constant;

T = system temperature;

P_1 = the initial system pressure;

P_2 = the system pressure at the end of test;

n_1 = the initial gas in mole;

n_2 = the gas in mole at the end of test.

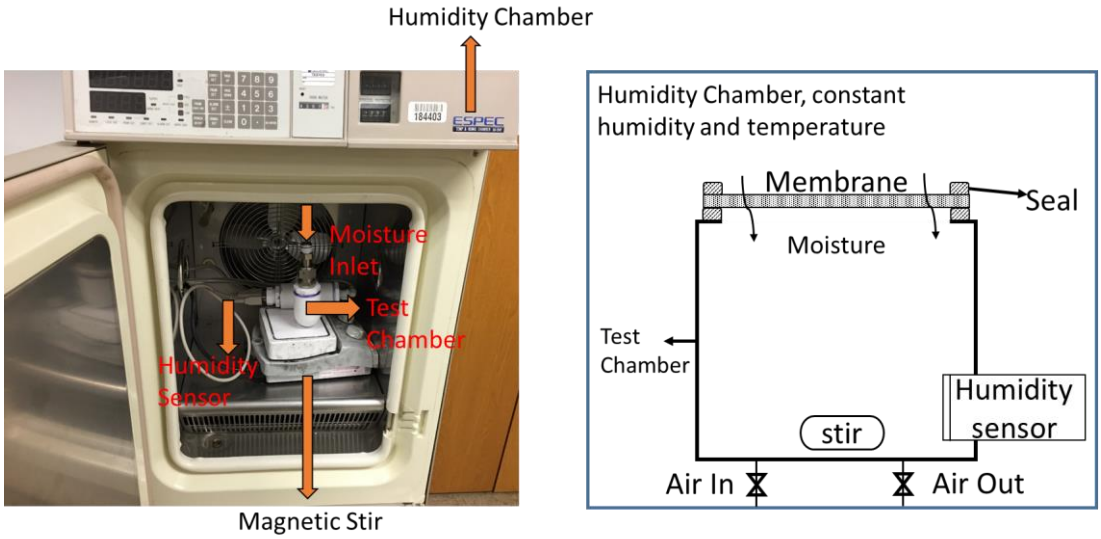

Figure 4-7. The humidification measurement device built in house (left) and the principle of humidification measurement (right)

4.3 Results and Discussion

4.3.1 Foaming results

4.3.1.1 Effect of saturation pressure

The gas concentrations of samples saturated under different pressures were measured and listed in Table 4-4. It can be found that the gas concentrations of samples with the same composition are similar, which indicates that in the selected pressure range, similar equilibrium gas concentrations can be reached although the required saturation times are different. For some polymer matrix, the increasing of saturation pressure will result in the increase of its degree of crystallinity, which will decrease the equilibrium gas concentration. In this case, the applied PBS is fully amorphous and no crystallinity will be generated [79].

SEMs of samples with similar gas concentrations and foamed under the same condition were taken. Figure 4-8 shows a typical pair of images of PEG600-20 samples saturated at 10 MPa and 5 MPa and foamed at 120 ºC. The porous microstructure confirms that the specimens have been foamed. Both specimens have a solid skin layer due to desorption. The microstructures of both samples are similar, which correspond to their similar CO_2 concentrations and porosities as seen in Table 4-4. The average pore size in both of the samples is 5 μm. The results indicate that both 10 MPa and 5 MPa saturation pressures results in similar equilibrium gas concentration on samples with the same composition. When foamed at the same condition, the samples with similar gas concentration obtained similar porosity, porous structure, and average pore sizes. The high saturation pressure is suggested to minimize the saturation time.

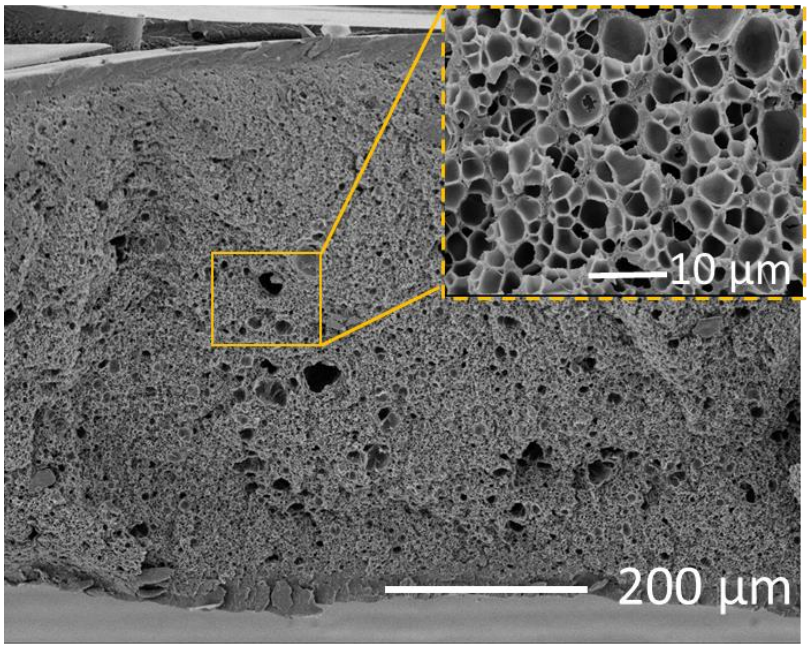

(a)

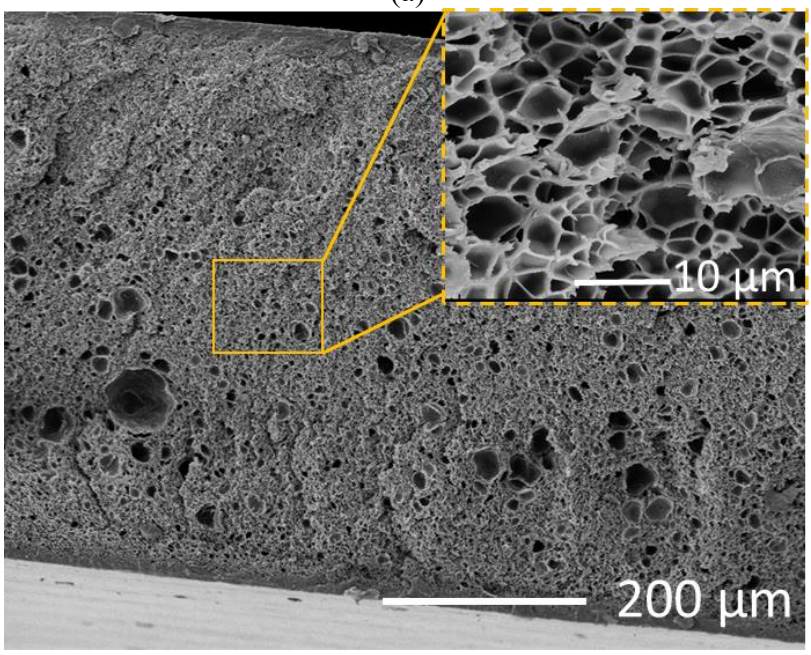

(b)

Figure 4-8. Cross sectional SEM images of (a) PEG600-20 saturated at 10 MPa and foamed at 120 ºC, and (b) PEG600-20 saturated at 5 MPa and foamed at 120 ºC

Table 4-4. Results of solid state foaming study (Foaming time fixed at 15 seconds)

Saturation		Sample ID	Gas Concentration (%)			Foaming Temp. (°C)	Porosity (%)	
Pressure (MPa)	Time (days)		Initial	15 min desorption	30 min desorption			
10	5	BPS	4.8					
		PEG200-20	2.5	2.1±0.1	-	100	3.2	
						110	12.7	
						120	12.9	
						130	7.8	
		PEG200-30	2.1	1.8±0.1	-	50	-	
						70	4.6	
						80	2.1	
		PEG600-20	6.2	4.6 ±0.1	*4.2*	100	37.8	-
						110	44.5	-
						120	59.5 (15min)	*63.7 (30min)*
						130	65.7	-
		PEG600-30	4.2	3.6±0.2	-	50	16.5	
						70	39.7	
						80	34.5	
5	10	PEG200-20	2.5	2.0	-	110	12.3	
		PEG200-30	2.1	1.8	-	70	4.2	
		PEG600-20	6.1	4.5	-	120	57.1	
		PEG600-30	4.1	3.5	-	70	38.8	

4.3.1.2 Effect of foaming temperature

The foaming temperature of polymer matrix is typically at least 15 °C lower than their T_g, because the absorbed CO_2 functions as an additional plasticizer lowering the T_g of polymer matrix. The samples saturated at 10 MPa and desorbed for 15 minutes were foamed at the temperatures according to their T_g for 15 seconds. The temperature ranges are listed in Table 4-4, which are 100, 110, 120, and 130 °C for samples containing 20 wt% PEGs, and 50, 70, and 80 °C for samples containing 30 wt% PEGs. In general, samples foamed at the lowest temperature of selected range did not shown much of porosity because that temperature is not able to soften the polymer matrix enough to release gas rapidly. Samples foamed at medium temperature had the highest porosity, which are 70 °C for PEG200-30 and PE600-30 and 120 °C for PEG200-20 and PEG600-20. As the foaming temperature was further increased, the porosity of the samples dropped down. Since the foaming temperature was approaching T_g, foaming at higher temperatures weakened the material and the porous structure collapsed resulting in a lower porosity. One exception is PEG600-20 foamed at 130 °C, its porosity increased due to the formation of big bubbles as shown in Figure 4-9. Samples saturated at 5 MPa were foamed using the temperatures generating the highest porosity (PEG600-20, 120°C) in the 10 MPa categories. Similar porosity was obtained on samples from both saturation pressures as described in the last section.

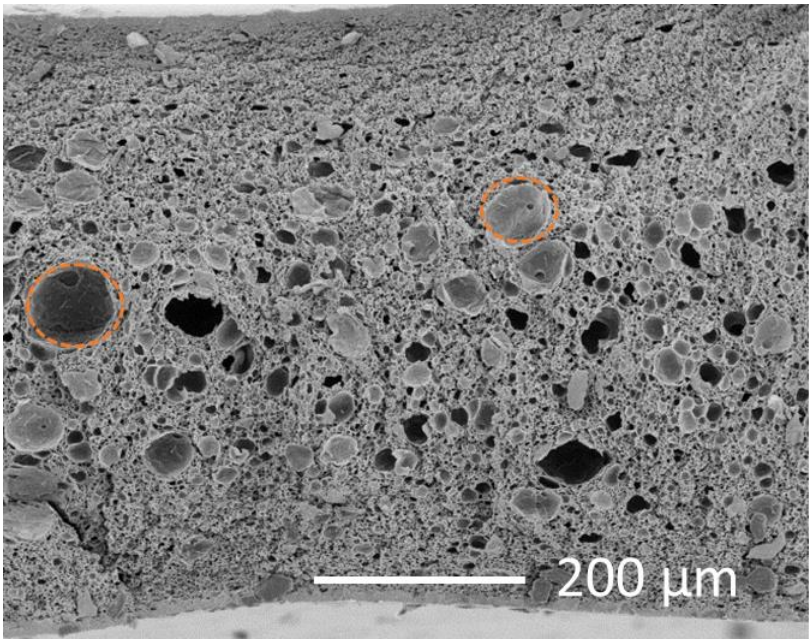

Figure 4-9. Cross section SEM image of PEG600-20 saturated at 10 MPa and foamed at 130 °C

The pore size in the samples foamed at 120 °C and 130 °C which exhibited the highest two porosities were measured. The average pore size in the sample foamed at 130 °C (a large portion of pores were bigger than 10 µm) was around 8 µm bigger than that in the sample foamed at 120 °C (around 5 µm) as shown in Figure 4-10. This result indicates again that a high foaming temperature approaching the T_g of polymer matrix may soften the polymer matrix and result in relatively bigger average sizes. If the foaming temperature exceeds T_g of polymer matrix, the polymer would further lose strength and viscosity resulting in the collapse of pores. Figure 4-11 is an example of over-foamed PEG 600-20 at 150 °C, in which the surface became rough and visible big bubbles were formed.

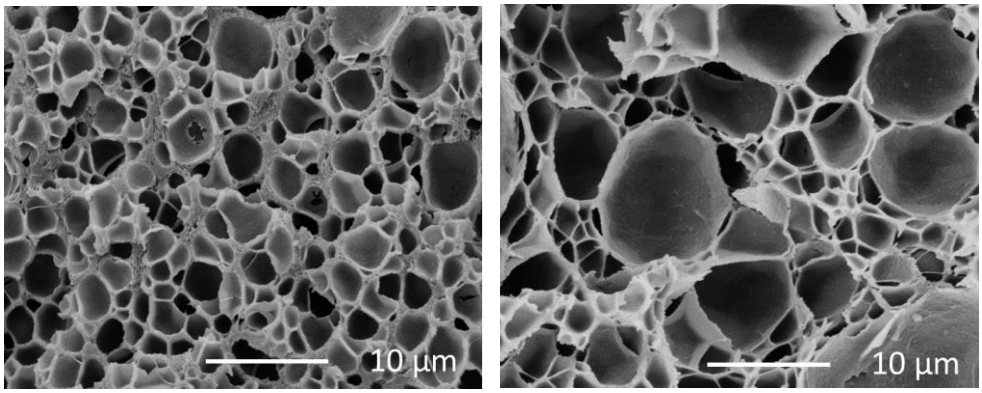

(a) (b)

Figure 4-10. Cross section SEM image of PEG600-20 saturated at 10 MPa and foamed at (a) 120 °C and (b) 130 °C

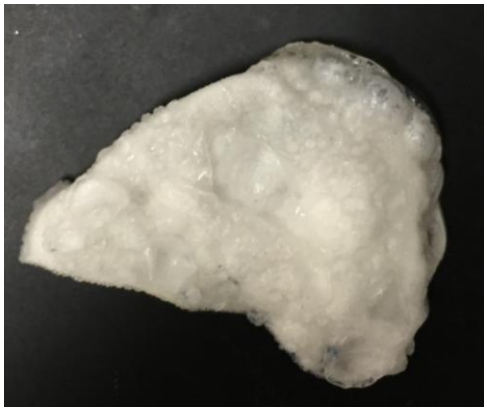

Figure 4-11. Over foamed PEG600-20 at 150 °C

4.3.1.3 Effect of blend composition

PEG600 and PEG200 applied as plasticizer in this work are low molecular weight polymers. The common thought of plasticizers is that they can be embedded among the chains of polymers to space the chains apart and increase the free volume, hence the glass transition temperature the polymer can be lower significantly. As described in the Introduction section, PEGs are miscible with BPS, hence can

function as plasticizers. Theoretically, the increasing free volume will provide more accommodation and increase the equilibrium gas concentration in polymer matrix when saturated. However, from the gas concentration data in Table 4-4, it can be found that PEG600-20 has a higher gas concentration than pure BPS and also higher gas concentration than PEG600-30. The gas concentration in PEG200-20 is higher than PEG200-30. The potential explanation of this phenomenon is that the involvement of proper amount of PEGs (20 wt%) increases the free volume of BPS providing more accommodation for gas. When PEGs content increases to 30 w%, the extra PEG small molecules may occupy some free volume resulting in a lower gas concentration than pure BPS. It can also be found that PEG600/BPS has a much higher gas concentration than PEG200/BPS. The reason is PEG600 has a longer molecular chain than PEG200, which folds and entangles with BPS to generate a bigger free volume. As found by Oh [79], BPS is fully amorphous due to the high number of rings and resulted entanglement between chains. The PEG/BPS is fully amorphous as well due to the miscibility of the two polymer chains, although PEG itself is slightly crystalline. The effect of crystallization under high pressure on gas concentration can be neglected accordingly in this work.

The solid state foaming is driven by both foaming temperature and gas concentration. When gas concentration is low, the polymer matrix can be slightly foamed or not foamable even at a temperature close to T_g. Figure 4-12 illustrates the cross sectional images of PEG200-20 and PEG200-30 foamed at 120 °C and 70 °C respectively. It can be found that both samples were only slightly foamed because of the low gas concentration.

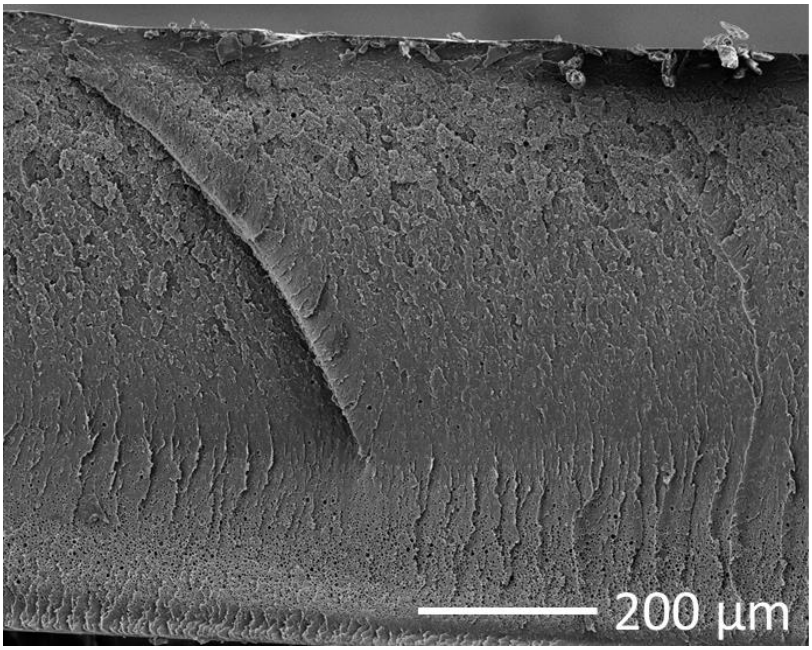

(a)

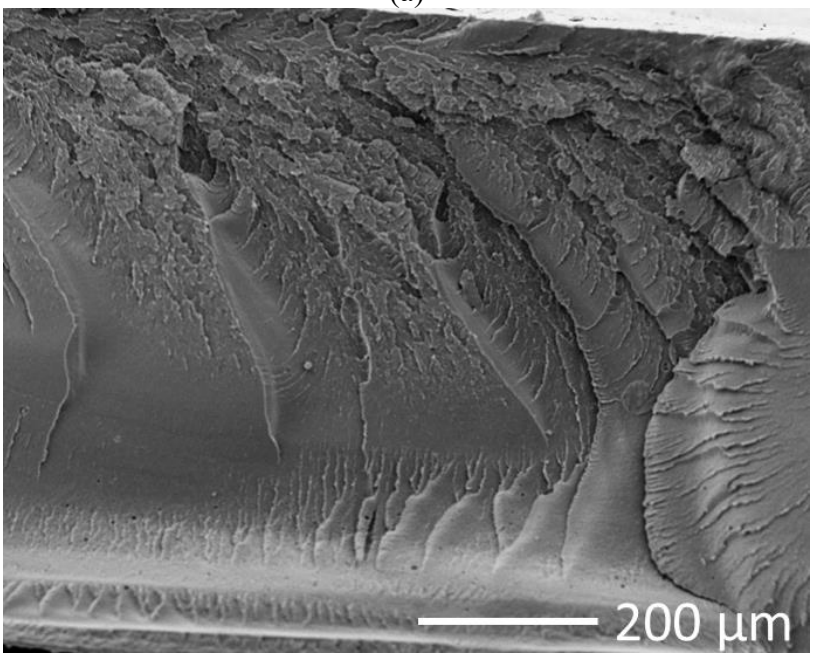

(b)

Figure 4-12. Cross section SEM images of (a) PEG200-20 saturated at 10 MPa and foamed at 120 ºC, and (b) PEG200-30 saturated at 10 MPa and foamed at 70 ºC

4.3.2 Humidification test

To characterize the applicability of fabricated PEG/BPS membranes and foams as fuel cell humidification membranes, humidification tests were conducted applying the in-house built test device shown in section 4.2.3. The results were analyzed and shown in Figure 4-13 and summarized in Table 4-5. In general, the humidification performance of a membrane can be characterized with diffusion coefficient, which determines the water vapor saturation speed in the test chamber. In this work, we run the humidification test for 80000 sec and use the time of reaching 50 % of the final RH in test chamber to quantify the humidification performance.

As summarized in Table 4-5, Nafion 212 membrane yielded the shortest time of reaching 50% RH (8000 s) and highest RH of 82.5%. Before foaming, the descending order of water vapor saturation rate as well as the descending order of maximum relative humidity reached are PEG200-30 > PEG200-20 > PEG600-30 > PEG600-20. The potential reason is that the smaller PEG200 molecules in BPS have higher mobility than PEG600, which would enhance the water molecule diffusion through the membrane by enhanced solution diffusion. This order was changed dramatically after the foaming of the samples. It can be found that foamed PEG600-20 features the shortest time of reaching 50% RH, which is 10000 s. Foamed PEG 600-30 shows the second shortest time of 16000 s, which is close to the 16500 s of foamed PEG200-30. Foamed PEG200-20 shows the longest time of 20000 s, which is the same as solid PEG200-20. In general, the saturation time of PEG600-20 reduced by 70000 s and the saturation time of PEG600-30 reduced by 18000 s after foaming, while the saturation time of PEG200s has no significant change after

foaming. The maximum humidity of all the foamed samples is similar, which is around 78-79 %.

Table 4-5. Results of humidification tests (conducted at 95% RH, 30 ºC; three tests per sample)

Sample ID	Average time to reach 50 % RH (s)	Time difference between solid and foamed samples at 50% RH	Maximum RH (%)
Nafion 212	8000	-	82.5
PEG200-20	20000	-	78.4
PEG200-30	16000	-	80.1
PEG600-20	80000	-	51.9
PEG600-30	34000	-	71.2
Foam PEG200-20	20000	0	78.4
Foam PEG200-30	16500	+500	79.1
Foam PEG600-20	10000	-70000	79.8
Foam PEG600-30	16000	-18000	77.1

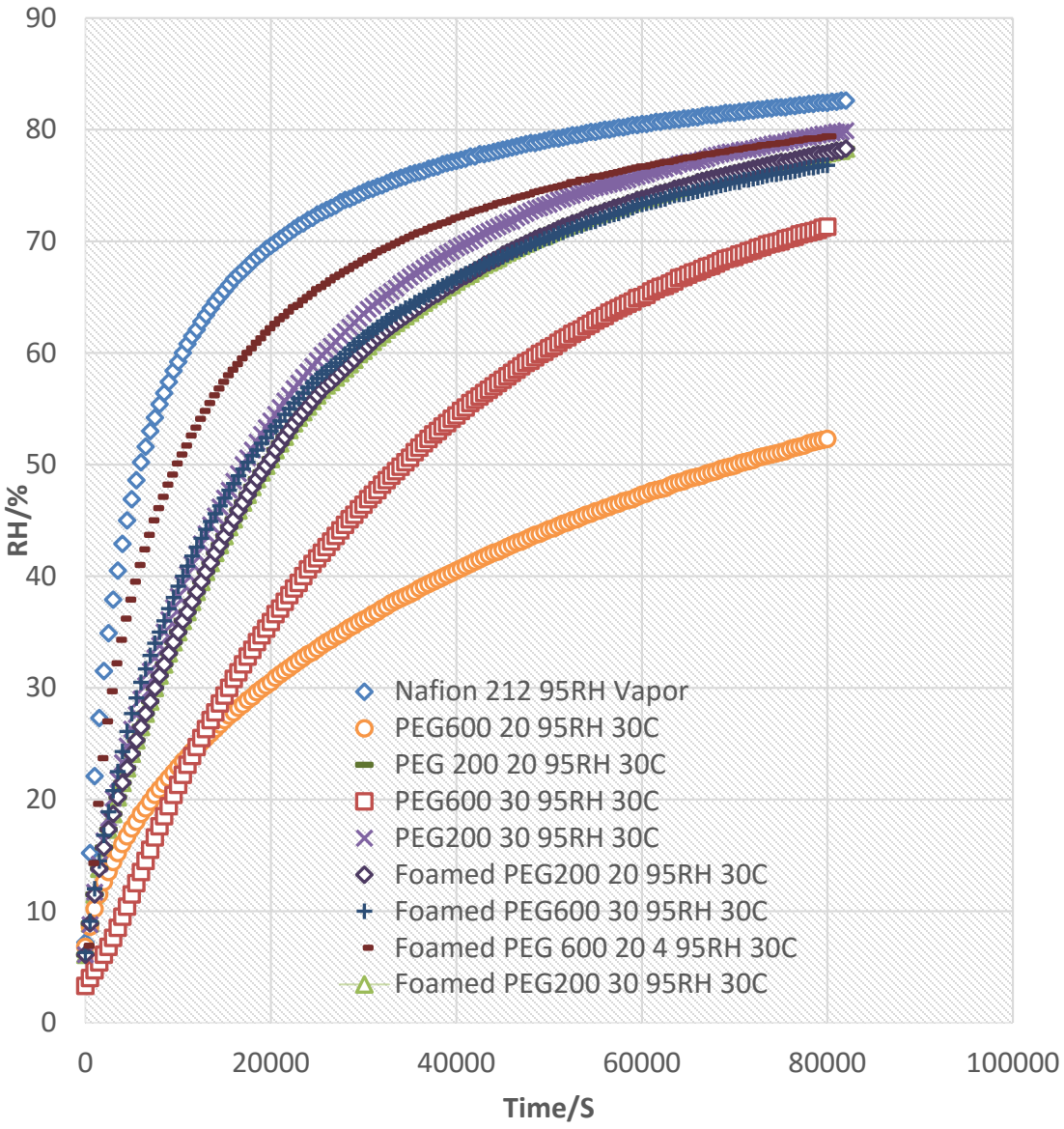

Figure 4-13. Humidification performance tests of solid and foamed samples in the in-house built system at 95 % relative humidity (RH) and 30 ºC

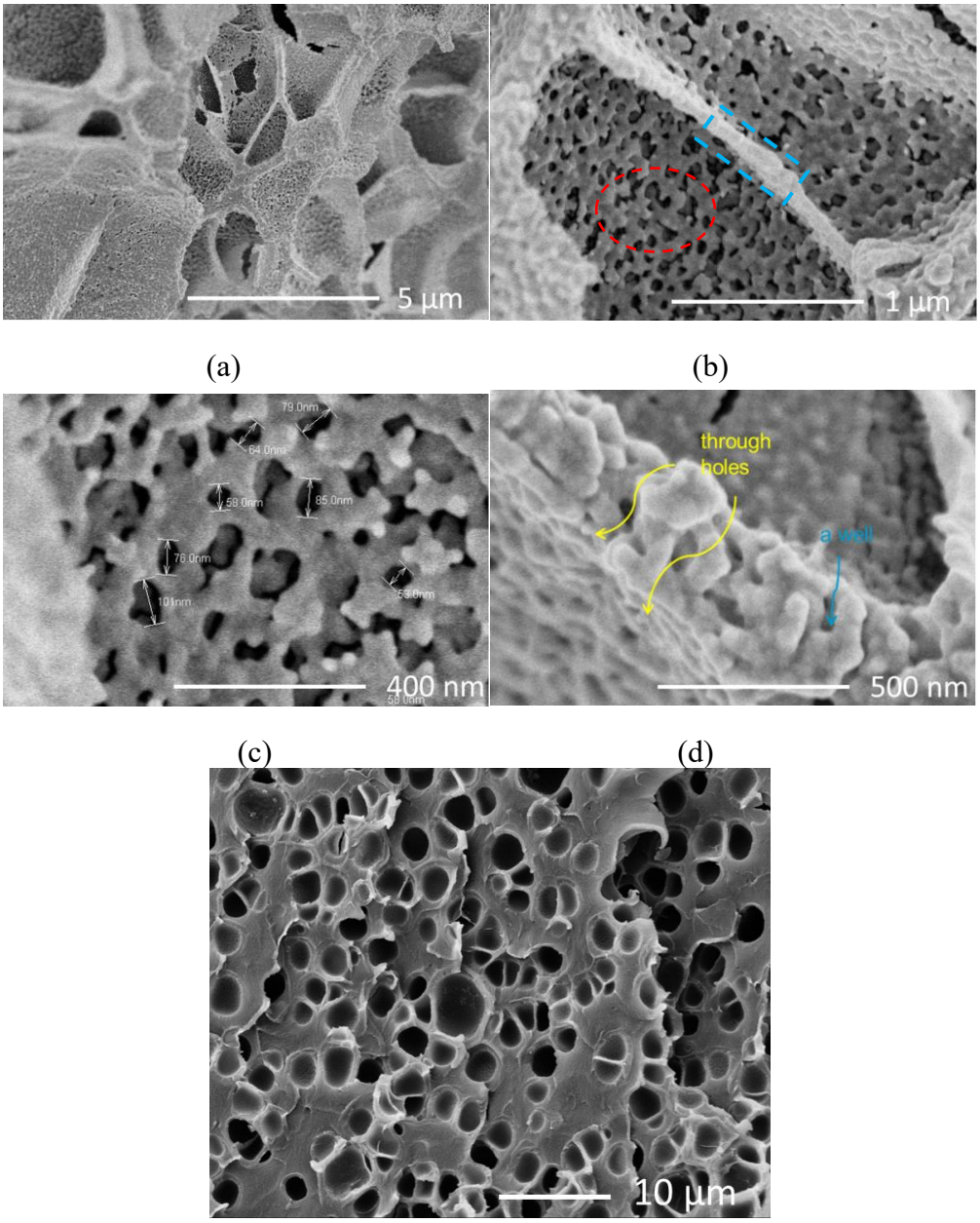

Figure 4-14. Zoomed in cross sectional images of (a) PEG600-20 saturated at 10 MPa and foamed at 120 ºC, (b) a cell of PEG600-20 located at (a), (c) nano open cells on the micro level cells of PEG600-20, (d) the wall between micro level cells of PEG600-20, and (e) PEG200-20 saturated at 10 MPa and foamed at 120 ºC.

The reasonable explanation for the results can be addressed as follows. The foamed samples with PEG600s demonstrate significant increase at the water vapor transfer rate, because they have higher porosity than the samples with PEG200s. Figure 4-14 (a) shows the cross section image of foamed PEG600-20, Figure 4-14 (b) shows one cell of the cross section with nano scale pores on the cell wall. The pore sizes in the read dash circled region of Figure 4-14 (b) were measured and shown in Figure 4-14 (c), which are in the range of 50-100 nm. Figure 4-14 (d) is the enlarged image of the yellow dash rectangular region, which indicates that the cells in foamed PEG600/BPS are connected by 50-100 nm size open pores. The pores can serve as water vapor convection paths because the nano pore size is bigger than the mean free path size of water vapor (42 nm). The foaming converted solution diffusion of solid membranes to a combination of solution diffusion and convection diffusion, which provides a higher water vapor diffusion rate. Figure 4-14 (e) shows the cross section structure of foamed PEG200-20/BPS. No nano-sized open pores were observed among the foamed cells. Foamed PEG200/BPS showed similar performance with the solid samples before foaming owing to the low porosity and absence of nano size pores in those samples. The foamed PEG600-20/BPS membrane has a humidification rate slightly lower than that of Nafion 212. Considering the thickness difference (Nafion: 50 μm, PEG600-20/BPS foam: 280 μm), the water vapor diffusion rate in PEG600-20/BPS foam may be higher than that in Nafion.

4.3.3 Membrane leak test

To test the tolerance of the samples when water concentration is low in fuel cell exhaust gas, the samples were conditioned at 6% RH and 25 ºC. All the solid

samples cracked after 12-48 h as shown in Figure 4-15(a), among which PEG600-20 shows a centimeter size through hole indicating the lowest plasticizing effect of 20 wt% loading of PEG600. As shown in Figure 4-15(b), there are no observable cracks found on foamed samples conditioned under the same condition for 48 h. The potential reason is that the PEG/BPS matrix would shrink because of the loss of water under 6% RH. A strain across the PEG/BPS would be generated because of the shrinkage (the sample was still mounted between two seals, hence the edges were constrained), which may generate cracks when it exceeds the maximum tolerable strain. As a contrast, there are micro or nano pores inside the foamed PEG/BPS which can prevent the formation of global strains by formation of local strains or block the propagation of cracks once they are formed [83].

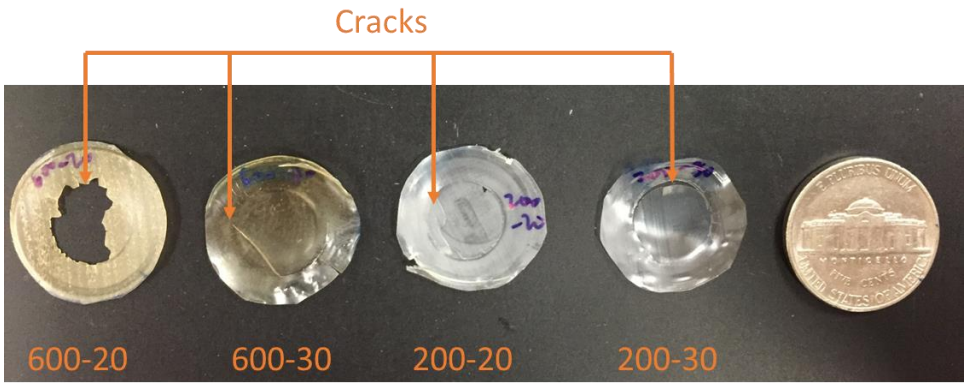

(a)

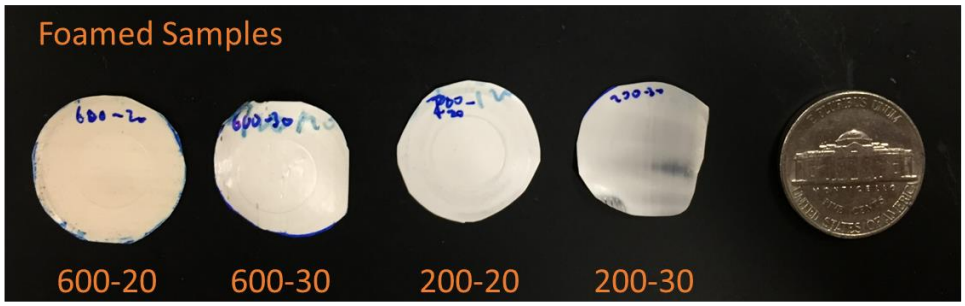

(b)

Figure 4-15. (a) Cracked solid (unfoamed) membranes after humidification test and dried at 6% RH and 25 ºC for 12-48 h, (b) foamed membranes after humidification test and dried at 6% RH and 25 ºC for 48 h

To examine if there are invisible cracks on the foamed sample and also test their gas barrier performance, a leak test was conducted using the device shown in Figure 4-7. The test conditions are 5 Psi pressure, 25 ºC, and 10 h. PEG600-20/BPS and PEG200-20/BPS foamed at 120 ºC were tested because of their higher porosity in their own category. Aluminum (Al) foil, a non-permeable air barrier, was also tested as a reference. The pressure change results were shown in Figure 4-16. It can be found that foamed PEG200-20/BPS has a similar pressure drop as Al foil along the 10 h test time. The foamed PEG600-20/BPS shows a bigger pressure drop. The

pressure drop of Al foil can be considered as the system leak. After subtracting the system leak, foamed PEG600-20/BPS shows a pressure drop of 0.671 Psi and foamed PEG200-20/BPS shows a pressure drop of 0.0541 Psi. The air molecule changes in mole were calculated according to Equation (4-2), which are 0.00084 mole and 0.000085 mole, respectively. Applying the ideal gas law, the leaked gas volumes under 5 Psi and 25 ºC were calculated to be 0.069 standard cubic meter and 0.0056 standard cubic meter. The average gas leak rates over 10 h were calculated as 1.14×10^{-4} SCCM and 9.36×10^{-6} SCCM, respectively. These two numbers are much lower than the failure criteria of 10 SCCM set by the DOE membrane testing protocols [84]. The explanation of the extremely low air leak rate (or permeability) of foamed samples is the solid skin layer of the samples resulted from the desorption priori to solid state foaming. As shown in Figure 4-17, the skin layers are solid, hence they block the path of air to the foam interior open structures. The results suggested that solid PEG/BPS membrane will crack when they are applied as fuel cell humidification membranes for a long period (> ~10 h) when the humidity of fuel cell exhaust gas is low. The foamed PEG/BPS membranes have a far higher tolerance for low humidity operation conditions. The solid state foamed samples were proven not having cracks and show satisfaction of air barrier requirement of fuel cell humidification membrane.

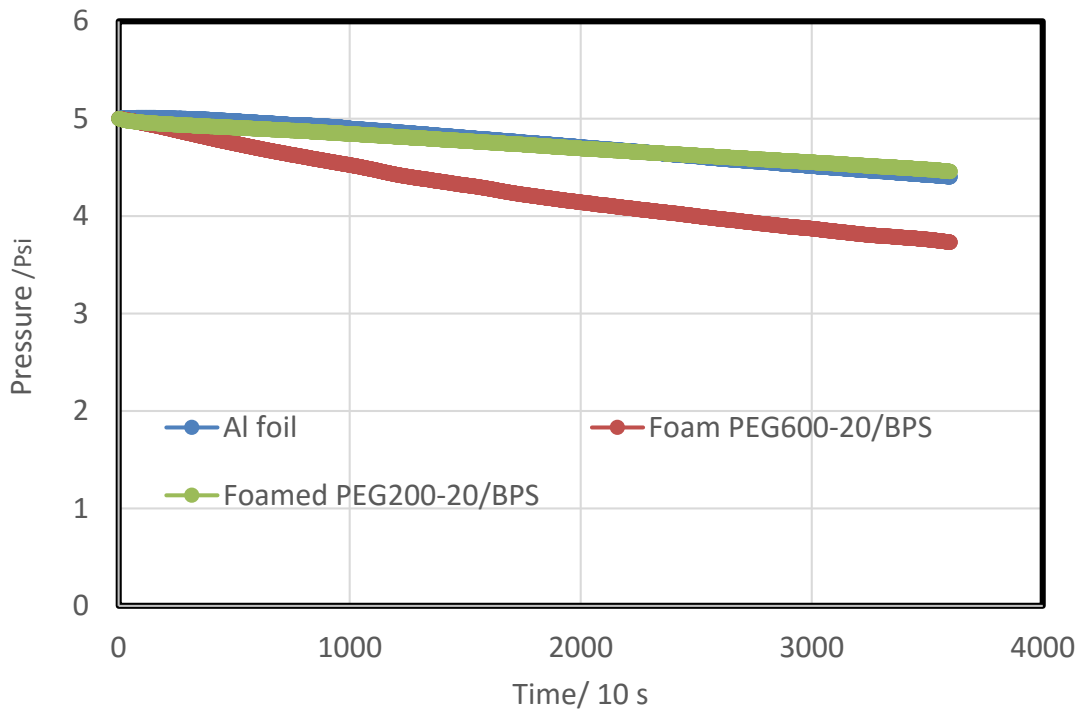

Figure 4-16. The membrane leak test results of Al foil, PEG600-20 saturated at 10 MPa and foamed at 120 ºC, and PEG200-20 saturated at 10 MPa and foamed at 120 ºC.

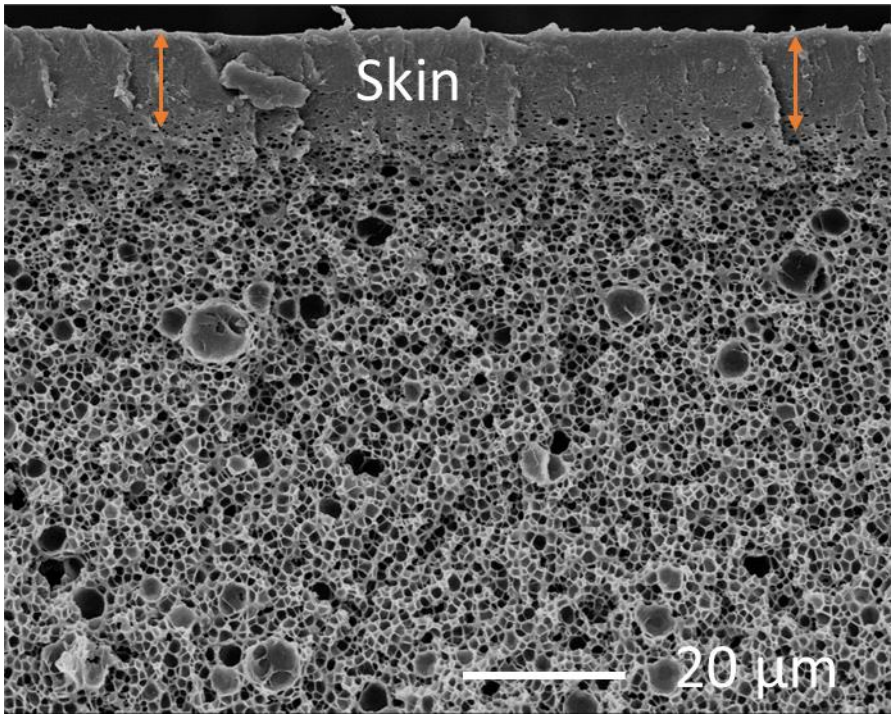

Figure 4-17. The skin layer resulted from desorption process (PEG600/BPS)

4.4 CONCLUSIONS

Novel PEG/BPS foams with micro and nano levels of pore sizes were fabricated using solid state foaming. The processing parameters to fabricate them were determined. The results show that 5 MPa and 10 MPa pressure give the same equilibrium gas concentration in the polymer matrix. Foaming temperature is critical to the structure of foamed samples: a proper foaming temperature is needed to obtain high porosity and small pore size. Composition of PEG/BPS blends has significant effects on equilibrium gas concentration in blends and foamed structures of blends. PEG200 containing blends have low gas concentration and low porosity after being foamed. The applicability of solid and foamed PEG/BPS membranes as fuel cell humidification membranes was investigated. After being foamed, PEG600

containing membranes show significant increase in both humidification rate and maximum relative humidity, while the PEG200 containing membranes have almost no changes. High porosity level and nano pores connecting the micro cells in foamed PEG600/BPS membranes are the main reasons of humidification performance improvement. The humidification performance of foamed PEG600-20/BPS membrane is similar to that of Nafion 212 membrane under the applied test conditions. Solid PEG/BPS membranes would crack during low humidity operation conditions, while foamed membranes show their advantage of keeping structural integrity under those conditions. Air leak test results indicate that foamed PEG/BPS membranes have air leak rates much lower than the DOE requirement. The high Tg (> 130 ºC) of PEG600-20/BPS allows an operation temperature similar or higher than Nafion. In addition, the price of BPS is around $2000/Kg, which will be far lower under mass production and after being blended with PEG. Around 6 m^2 membrane with 200 μm thickness can be processed out of 1 kg BPS, which will generate a cost of around $300/$m^2$ much lower than ~$1000/$m^2$ of Nafion (50 μm). The foamed PEG/BPS membranes show their potentials of being applied as alternative fuel cell humidification membranes.

Chapter 5. Fabricating Microcellular Nickel Foams using Assembled Microsphere Templates

5.1 INTRODUCTION

Like conventional metal foams, microcellular metal foams combine desirable properties of metal and porous material including high thermal, electrical conductivity, and low density, but with a much larger surface-to-volume ratio [38, 39]. Open-celled metal foams allow fluids to flow through, thus have attracted significant interest due to their applications in energy storage devices, such as lithium-ion batteries [85-87], supercapacitors [88-90], and solar energy storage tanks [91, 92]. The metal foams in these applications are used as scaffolds to be loaded with active electrochemical or thermal materials for high efficiency operation. Pore size of the open-cell metal foams is a critical parameter affecting the efficiency of these energy storage devices. As the pore size becomes smaller, a shorter transfer path for charge or heat can be achieved between the functional material and the conducting struts of the scaffold. Therefore, a faster charging and discharging rate could be obtained while maintaining the same capacity [93].

Metal foams have been produced with a number of methods as described in the Introduction chapter, however all those methods still suffer limitations of generating small pore size, high porosity, or open celled structure. In general, the fabrication of open-celled microcellular metal foams is still challenging, due to the availability of small pore-size polymer foam templates, as well as the increased difficulty of mass transport inside the polymeric templates as the pore size reduces. Recently, a sphere-template electrodeposition method was used to fabricate micro- and nano-cellular metal foams [13, 14, 54, 94]. Well-defined cellular microstructure

W. Jiang, S. S. Sundarram, W. Li, Bulk Microcellular Metal Foam Fabrication Using a Novel Electroplating of a Polymer Microsphere Template, Manufacturing Letter, Volume 2, Issue 4, October 2014, Pages 118-121.

W. Jiang: Design and implement involved work, construct manuscript
S. S. Sundarram: Provide valuable discussion and edit the constructed manuscript
W. Li: Direct and supervise the work as supervisor

was obtained after removing the polymer sphere template. However, the foams that were achieved had only a few layers of pores and the overall thickness of the foam was only a few micrometers [52].

We target large scale applications such as solar or thermal energy storage, where these microcellular metal foams will be infiltrated with a large quantity of phase-change material (PCM). Bulk microcellular metal foams would be needed in these applications. As the foam thickness becomes larger, the mass transport process inside the sphere templates will become a limiting factor, affecting both uniformity of foam growth and overall fabrication time.

This chapter discusses the fabrication of bulk microcellular nickel foams. Two different methods are explored. The first is an electroplating method where the metal plating starts from a conductive substrate on which the microsphere template is attached. The second is a hybrid electroless deposition and electropolishing method that is developed in this study. Hydrophilic polymer microsphere templates fabricated in Chapter 2 were used as the templates.

Electroplating with various parameters was conducted and the effects were investigated. Microcellular nickel foams with pore size on the level of 1-10 μm and 60-100 μm were produced with electroplating. However, the electroplating process itself is inherently an unstable process, prone to generate non-uniform nickel foam structures.

To overcome the low homogeneity of nickel foams from electroplating, a novel electropolishing assisted eletroless deposition (EPAELD) method was developed in this study. Ethanol based activation solution was used to allow its infiltration into the porous structure. Comparing to electrodeposition, electroless

deposition does not require an electrode to start the metal deposition process. The reaction happens uniformly across the polymer template, given that the local reactant concentration is also uniform. Although metal foams fabricated with electroless deposition may need a subsequent electrodeposition step to increase the metal layer thickness, the process itself is not sensitive to the uniformity of the polymer sphere template. However, the electroless deposition process suffers the diffusion limitation to reactants inside the polymer sphere templates. Even after long deposition hours, it is challenging to fabricate thick microcellular metal foams.

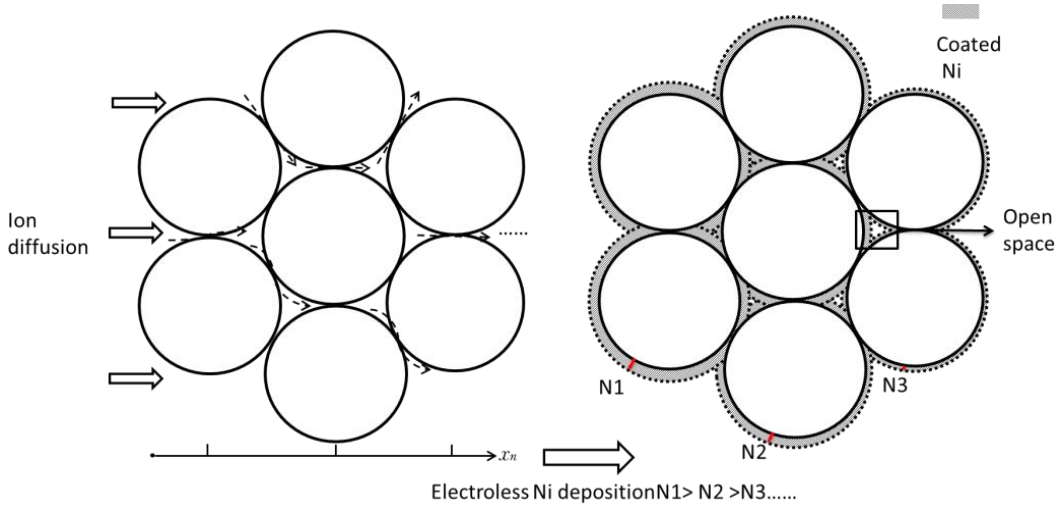

Figure 5-1. Diffusion limitation in microcellular metal foam fabrication using conventional electroless deposition

The problem of diffusion limitation in the electroless deposition process is illustrated in Figure 5-1. Initially, the microsphere template can be fully saturated with electrolyte and the reaction happens at a uniform rate, consuming the same amount of metal ions everywhere in the sphere template. As the local ion concentration becomes lower due to reaction, diffusion from the bulk electrolyte will

be needed to replenish the ion loss. A concentration gradient of ions will then form and metal ions deposit faster in the outer regions of the template where the ion concentration is higher. This will in turn further limit the ion diffusion, as the channels for diffusion at in the outer region become narrower. Therefore, the inner regions of the template could stay incompletely plated, while the outer surface of the template is completely sealed.

To overcome the diffusion limitation problem, an electropolishing step is applied to remove metal at the surface layers of the plated polymer template. This polishing step ensures the opening of ion-diffusion channels and the continuation of electroless deposition process deep inside the microsphere template. Bulk microcellular nickel foams with a thickness up to 2.5 mm were produced using this method.

5.2 EXPERIMENTAL

5.2.1 Materials

Hydrophilic polymer templates assembled with ethylene acrylic acid (EAA) microspheres, hydrolyzed poly(methyl methacrylate) (PMMA) spheres, and hydrolyzed paraffin spheres were used as the templates. The measured contact angles for EAA/water, hydrophilic PMMA/water and hydrophilic paraffin/water are listed in Table 5-1. The contact angles confirm the hydrophilic nature of the templates.

Table 5-1. Contact angle measurements for EAA/water, PMMA/water, and Paraffin water

Substrate material	Contact angle(°)
EAA	69.1
PMMA	36.1
Paraffin	50

5.2.2 Electro deposition

Electro deposition is an electrochemical reaction described by Equation (5-1). Nickel is oxidized to nickel ion at anode and reduced to nickel metal at cathode by applied current. In the electro deposition approach, paraffin was not selected because the weak bonds among paraffin spheres would break during the electroplating process. One side of sintered PMMA or EAA templates was attached to an electrode using electro conductive carbon glue. The templates were then submerged into an electrolyte made with nickel sulfate hexahydrate ($NiSO_4.6H_2O$, ACS reagent, 99%, Sigma Aldrich), boric acid (H_3BO_3, ACS reagent, 99.5%, Fisher Scientific) and deionized water for 5 hours. The polymer template was set as the cathode and a nickel strip was set as the anode. A constant DC voltage level is superimposed onto an amplified square wave signal to provide a power source for a pulse reverse deposition process. A separate DC voltage source is needed to maintain a constant average DC voltage, such that the amount of nickel deposition can be kept constant independent of the pulse voltage. The pulse voltage is provided to regulate the structure of nickel foam via either polishing the plated nickel foam or allowing the nickel ion compensation from electrolyte at the half cycle with reverse current. To investigate the effect of parameters, the experiments on EAA foams were conducted

with two voltage levels and two frequency levels following a factorial experimental design as shown in Table 5-2. Two pulse amplitudes (2.6 and 4.9 V) and two frequency levels (50 and 200 Hz) were used. The average DC level was kept at 1.8 V. The duty cycle of pulse signal was kept at 50%. Two sets of samples were fabricated, with electroplating time of 12 h and 20 h, respectively. In the case of PMMA templates, the DC level was kept at 2 V while two pulse amplitudes of 3 V and 10 V were applied. The frequency of the pulses was kept at 200 Hz and two duty cycle levels of 20% and 50% were applied. Figure 5-2 shows the schematic of experiment, and Figure 5-3 demonstrates the principle of pulse involved electro plating.

$$\begin{aligned} &\text{At anode: } Ni \rightarrow Ni^{2+} + 2e^{-} \\ &\text{At cathode: } Ni^{2+} + 2e^{-} \rightarrow Ni,\ H_2O \rightarrow H^{+} +\ OH^{-} \\ &2H^{+} + 2e^{-} \rightarrow H_{2,}\ Ni^{2+} + 2OH^{-} \ \rightarrow\ Ni_2OH \end{aligned} \tag{5-1}$$

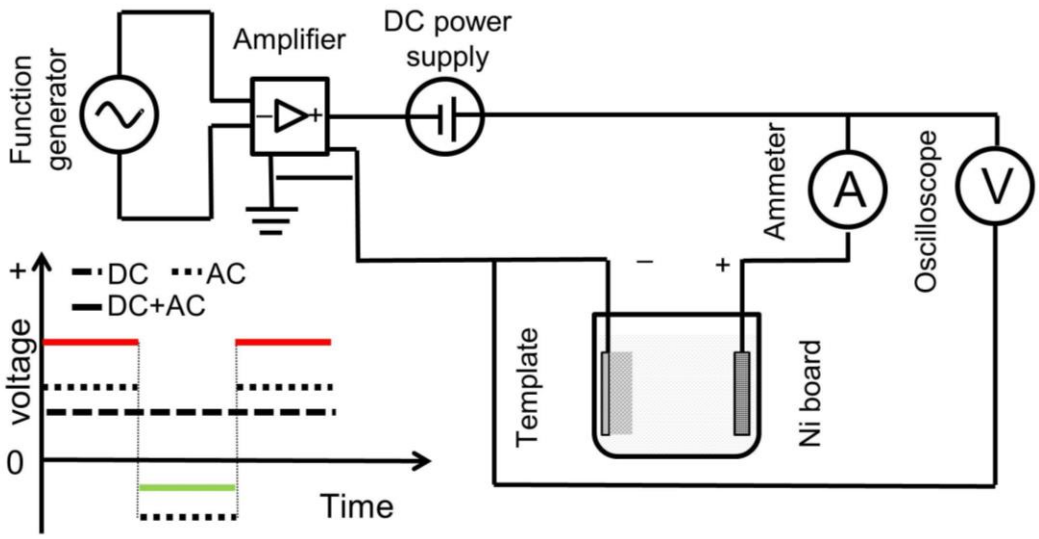

Figure 5-2. Nickel electroplating schematic. DC power supply: PK precision 1672; Function generator: BK Precision 4012A; Amplifier: PYLE PTA1000; Electroplating liquid: $NiSO_4.6H_2O$, H_3BO_3, and H_2O

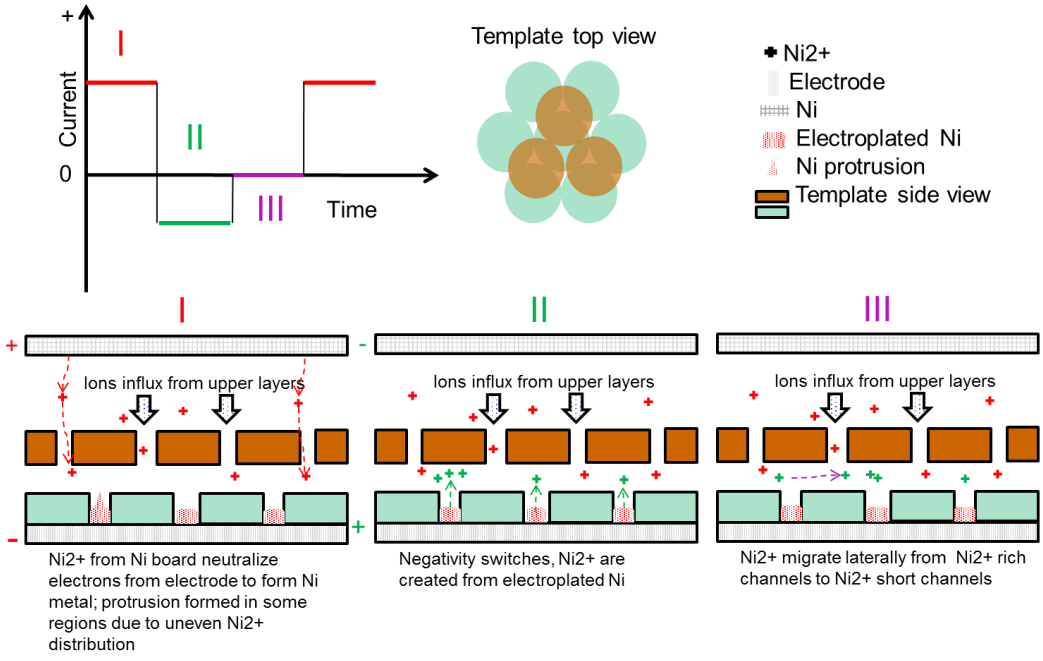

Figure 5-3. Schematic of the electroplating process with pulsed current

5.2.3 Electropolishing assisted electroless deposition

Electroless Ni deposition is an autocatalytic process for depositing Ni on nonconductive surfaces including polymers. Ni deposition on polymers normally includes three steps: etching of the polymer surface, activation, and deposition. Etching increases the hydrophilicity of a surface by generating pits or introducing hydrophilic groups. Activation deposits a layer of catalytic metal, such as palladium, to facilitate the subsequent nickel deposition. The Ni depositing solution consists of Ni ions, reducing, buffering, and complexing agents. The reducing agent converts the palladium ions to palladium metal, which then acts as a catalyst for reducing nickel ions to nickel. The buffering agent helps to maintain proper solution pH to ensure a continuous reaction (pH = 10 in this work). The complexing agent enables the metal ions to remain in soluble form. The composition of applied Ni electroless deposition electrolyte was shown in Table 5-2. Ethanol was included in the electrolyte to further improve the wettability of the polymer template by lowering surface tension.

Table 5-2. Composition of Ni electroless plating solution

Constituent	Quantity (g)
$NiSO_4.H_2O$	2
$NaH_2PO_2.H_2O$	0.75
$Na_4P_2O_7.10H_2O$	1.5
$C_6H_{15}NO_3$	1.5
CH_3CH_2OH	2
H_2O	23

The complete chemical reaction of the electroless deposition process for depositing nickel using a hypophosphite reducing agent is given by Equations 5-2. Ni ions are reduced to Ni by hypophosphite with the palladium (Pd) as a catalyst.

$$Ni^{2+} + 4H_2PO_2^- + H_2O \xrightarrow{Pd} Ni + 3H_2PO_3^- + P + 1.5H_2 + H^+ \qquad (5\text{-}2)$$

The plating solution was subjected to ultrasound treatment to ensure that hydrogen generated in the process was not trapped inside the porous structure impeding the diffusion of plating solution [95]. PMMA and paraffin templates were used in the process. They were first treated in an activation solution (0.1 wt% $PdCl_2$ in ethanol) for 2 h at room temperature, followed by a reduction of Pd^{2+} to Pd in a NaH_2PO_4 aqueous solution (0.1 wt%). An electroless deposition process was conducted in an electroless electrolyte (Table 5-2) for 4 h at room temperature. After attaching to an electrode, the electroless deposited template was positioned in an electroless deposition bath as an anode. For PMMA templates, a pulsed DC power with a 90% duty cycle and 200 Hz frequency was applied for 3 h at a current density of 10 mA/cm^2. The current was then reduced to 4 mA/cm^2 and maintained for 60 h. For paraffin templates, a current of 4 mA/cm^2 was applied for 3 h to open the channels among spheres, and a lower current of 1.5 mA/cm^2 was then applied for 90 h. Figure 5-4 shows the process and schematic of the electropolishing assisted electroless deposition (EPAELD) process. Stage 1 was electroless deposition to introduce electrical conductivity to the opal. At the end of Stage 1, the surficial channels could be blocked by plated nickel resulting in the termination of nickel deposition in the interior region. Stage 2 was designed to open the sealed channels

using a relatively higher current. Stage 3 was designed to supply a lower current to polish off partial nickel and keep the channels open.

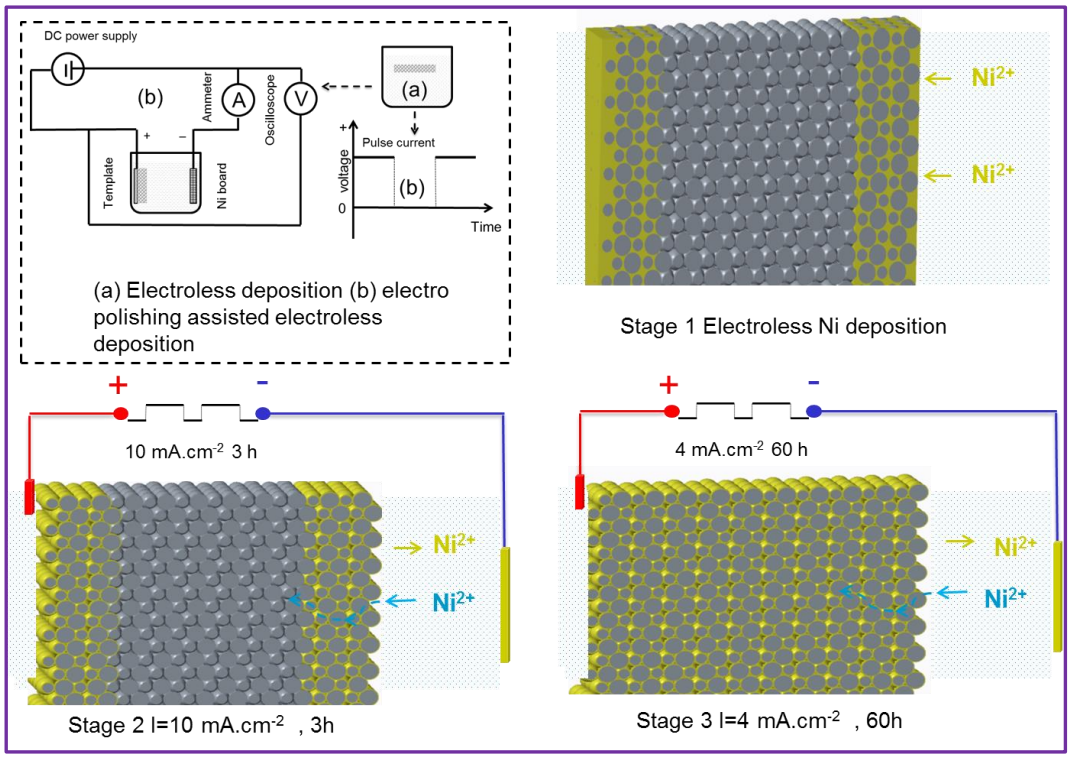

Figure 5-4. Proposed schematic of EPAELD (condition for PMMA templates)

Table 5-3. Composition of the activation solution

Constituent	Quantity (g)
CH_3CH_2OH	35
1N HCl	5.1
$PdCl_2$	0.04

5.2.4 Polymer template decomposition

The thermal cycle to decompose the polymer template consisted of two steps, as shown in Figure 5-5. Initially, the samples were heated to 450 ºC for one hour in standard atmosphere to decompose the polymer and then allowed to cool in air to room temperature. This resulted in the formation of nickel oxide because Ni reacts with oxygen at a temperature above 400 ºC. The product was then kept at 650 °C for 4 hours under a mixed gas flow of 0.020 standard liters per minute (SLPM) H_2 and 0.180 SLPM Ar to reduce oxidation. The system was cooled to room temperature at a rate of 10 °C/min.

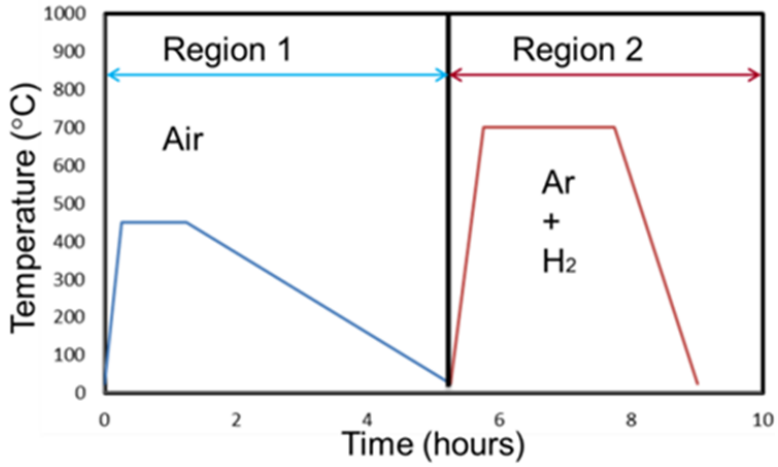

Figure 5-5. A schematic of the thermal treatment cycle to obtain Ni foam from metal filled polymer template

5.2.5 Characterization

The polymer templates after electroplating were freeze-fractured with liquid nitrogen and observed under Nikon LV150L optical microscope equipped with a digital camera. The cross sections of the nickel foams were observed with a JEOL

NeoScope 5000 scanning electron microscope (SEM). Image J was used to obtain pore size measurements from SEM images. Energy dispersive X-ray spectroscopy (EDS) elemental analysis was performed using Quanta 650 FEG SEM to determine the composition of the fabricated nickel foams. The porosity of the fabricated nickel foams was measured using an ethanol uptake technique describe in Chapter 3.

5.3 Results and Discussion

5.3.1 Electro deposition

The experimental conditions and results of electro deposition are summarized in Table 5-4. The cross sections of polymer templates after electro deposition were examined with a Nikon optical microscope. Figure 5-6 shows cross sectional images of four representative samples obtained from one set of experiments with a depositing time of 12 h. Visible electro deposited nickel layers with gray color and a clear boundary between deposited and un-deposited regions can be observed. The uniformity of nickel deposition is defined as the ratio of area deposited.

Table 5-4. Experimental conditions and results of Ni electro deposition on EAA

Experiment	Factor		Response 12h plating		Response 20h plating	
	Voltage (V)	Frequency (Hz)	Thickness (μm)	Uniformity (%)	Thickness (μm)	Uniformity (%)
1	2.6	50	760	0.43	1300	0.36
2	4.9	50	500	0.51	990	0.48
3	2.6	200	410	0.49	870	0.41
4	4.9	200	380	0.54	710	0.50

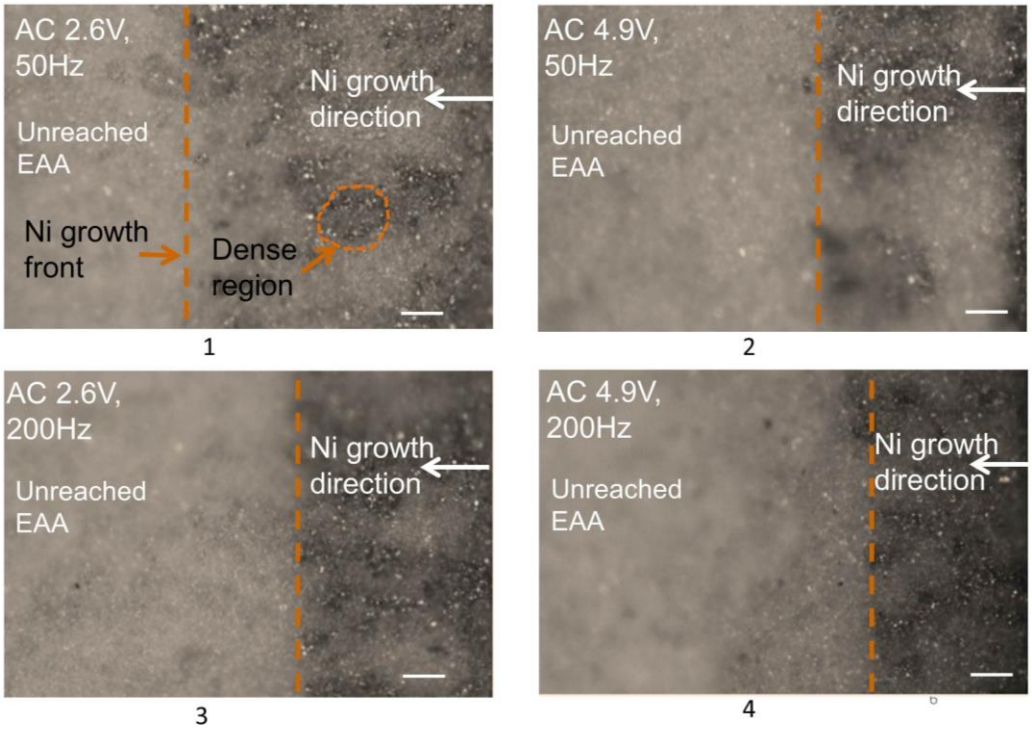

Figure 5-6. Representative images of electro deposited template following experiments 1-4 in Table 5-4. All scale bars are 100 µm

By summarizing the experiments with 12 h deposition, it can be found when frequency is fixed, the sample with a higher voltage level exhibits a denser electro deposited layer. When the voltage is fixed, the sample with a higher frequency shows a denser layer. Correspondingly, when one factor is fixed, the application of a higher level of the other factor results in a thinner deposited layer. The combination of higher levels of both factors results in the densest deposited layer. The samples electroplated for 20 h show a consistent trend with those for 12 h. Figure 5-7 shows the SEM images of nickel foam after the removal of EAA via a thermal treatment and the reduction of oxidized nickel. The foam consists of around 90 atomic% nickel, and the remaining Oxygen, carbon, and sodium are as shown in Figure 5-8,

which indicates a successful recovery. Voids resulted from the failure of depositing nickel to some interstitial space of temples can be found in the SEM images. It suggests that both frequency and AC voltage need to be pushed to an even higher level than those applied in this study to reduce the number of voids significantly or potentially eliminate them.

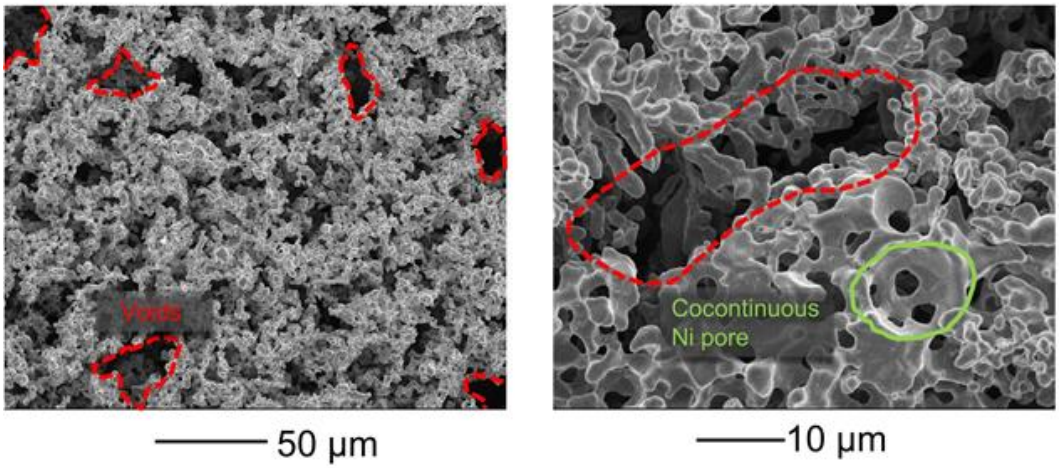

Figure 5-7. Nickel foam after EAA removal and reduction

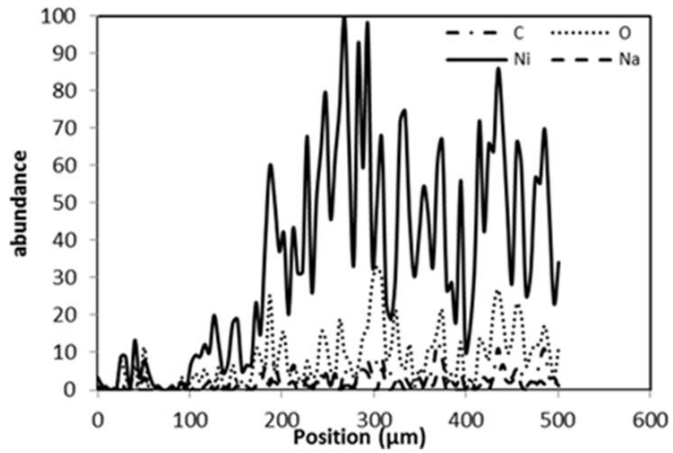

Figure 5-8. EDX results of Ni foam from EAA template after reduction

The reason that AC is applied in the process is due to its potential regulating effect on the structure of nickel foam. A theory was established based on a model of electroplating of an outer surface [67, 68]. When only DC is applied initially, nucleation of nickel metal happens along the entire surface of electrode due to the highly initial nickel cation concentration, and close-packed small crystal grains are formed. As the process progresses, only a portion of small crystals can have the opportunity of capturing cations and grow bigger due to the declining cation concentration. Eventually, big crystal grains grow even faster due to their shorter distance to the cation rich region, and form protrusions resulting in none uniformity of nickel structure. The current density on tips of protrusions are higher than that on a flat surface, which results in an uneven growth speed of surface front [96]. When AC is applied, a negative current can be generated at each cycle, which inverses the cathode and anode. The nickel cations can be replenished by both the cation diffusion from electroplating solution and the dissolution of plated nickel. A cation diffusion model under a square wave voltage was established to show the cation replenishment near cathode [96].

$$\frac{C_S}{C_O} = 1 - \frac{A}{D}\sum_{N=0}^{\infty} B \times \left\{ I \frac{1-exp\left[\frac{-(2n+1)^2 aT}{r+1}\right]}{1-exp[(2n+1)^2 aT]} \right\} \tag{5-3}$$

where *A*, *B,* and *a* are constants related to diffusion thickness, Faraday's constant, and cation concentration, *I* represents the current applied for nickel growth, *n* is the number of cycles, *r* is duty cycle, *D* is diffusion coefficient of cation in solution in templates, C_O is the Ni cation content in plating solution, and C_s is Ni cation content near cathode surface.

If the current I is constant, C_s/C_O will decrease with the increasing AC cycle period T, so increase with the increasing AC frequency. Beside the even nickel growth resulted from a high C_s, more nucleation can also be triggered by AC to form a new layer of close-packed small crystal grains. As a result, protrusions are prevented and the nickel structure is regulated. In our electrodeposition experiments, this theory is verified, although the cation diffusion is significantly complicated by the porous morphology of templates. Physically and electrochemically, there are two underlying mechanisms for the effect of frequency. When applying a high frequency, a relatively high near cathode cation concentration is obtained and leads to an even nickel growth, meanwhile the growth of existing crystal grains are interrupted more often to initiate more nucleation resulting in a tighter nickel structure. Regarding the voltage, a high voltage drives cations to near cathode region more rapidly than a low voltage does, so as to result in a denser nickel structure.

Hydrophilic PMMA templates were electroplated using the conditions listed in Table 5-4. The Ni structure from the 4th condition after PMMA removal is shown in Figure 5-9. It can be found that even the highest power AC was not able to produce thick and homogeneous Ni foam on PMMA templates. The potential reason is that the space between PMMA spheres is too big to provide constrain on Ni deposition. Ni deposition tends to choose an easier path with bigger channel sizes and better Ni ion diffusion from bulk electrolyte.

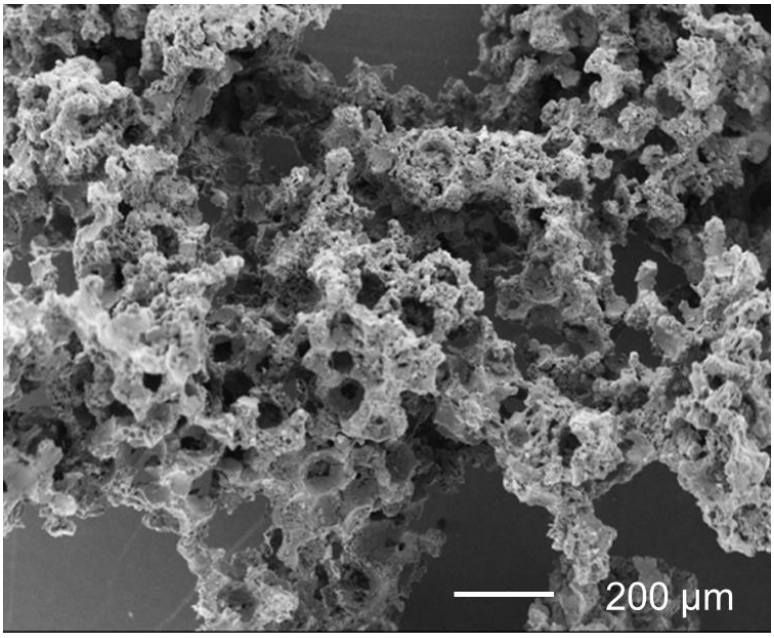

Figure 5-9. SEM images Ni structure plated with 1.8 V DC, 4.9 V AC, 50% duty cycle and 200 Hz

5.3.2 Electropolishing assisted electroless deposition

Figure 5-10 shows comparisons between samples plated with the proposed EPAELD process and those with the conventional electroless deposition process. Figure 5-10 (a) shows the cross section of a PMMA microsphere template deposited with the conventional electroless depositing method. The PMMA template was electroless deposited for 70 h to examine the effect of plating time by keeping the depositing time consistent with EPAELD. It can be found that the center region is bright and the out regions are dark, indicating nickel deposition mostly happened in the outer regions (areas with higher electrical conductivity appear dark under SEM). The reason is that channels in outer regions might become too narrow to provide enough ions to interior via diffusion. As a comparison, Ni was deposited thoroughly

across the cross section of EPAELD as shown in Figure 5-10 (b), which indicates the effectiveness of EPAELD on depositing Ni in thick template. Figure 5-10 (c) and (d) show a similar comparison on paraffin templates. Figure 5-10 (c) demonstrates the cross section of a paraffin template electroless plated for 100 h. It can be found that Ni plating mostly happened in outer regions in Figure 5-10 (c), and in Figure 5-10 (d) the paraffin template was thoroughly deposited when applying EPAELD for the same amount of time. Figure 5-10 (c) and (d) were captured employing an optical microscope due to the melting of paraffin under SEM. The results in Figure 5-10 indicate the capability of EPAELD to plate Ni into thickness template, which is lacking in conventional electroless Ni plating. After the removal of polymer template, the Ni structures are shown in Figure 5-11 and 5-12. It can be found in Figure 5-11 that bulk Ni foam was fabricated with a relatively dense and regular structure employing the EPAELD. The cross section of Ni foam (2.0 mm thickness) from EPAELD of a paraffin template was shown in Figure 5-12. A dense Ni structure was generated by EPAELD on the paraffin template.

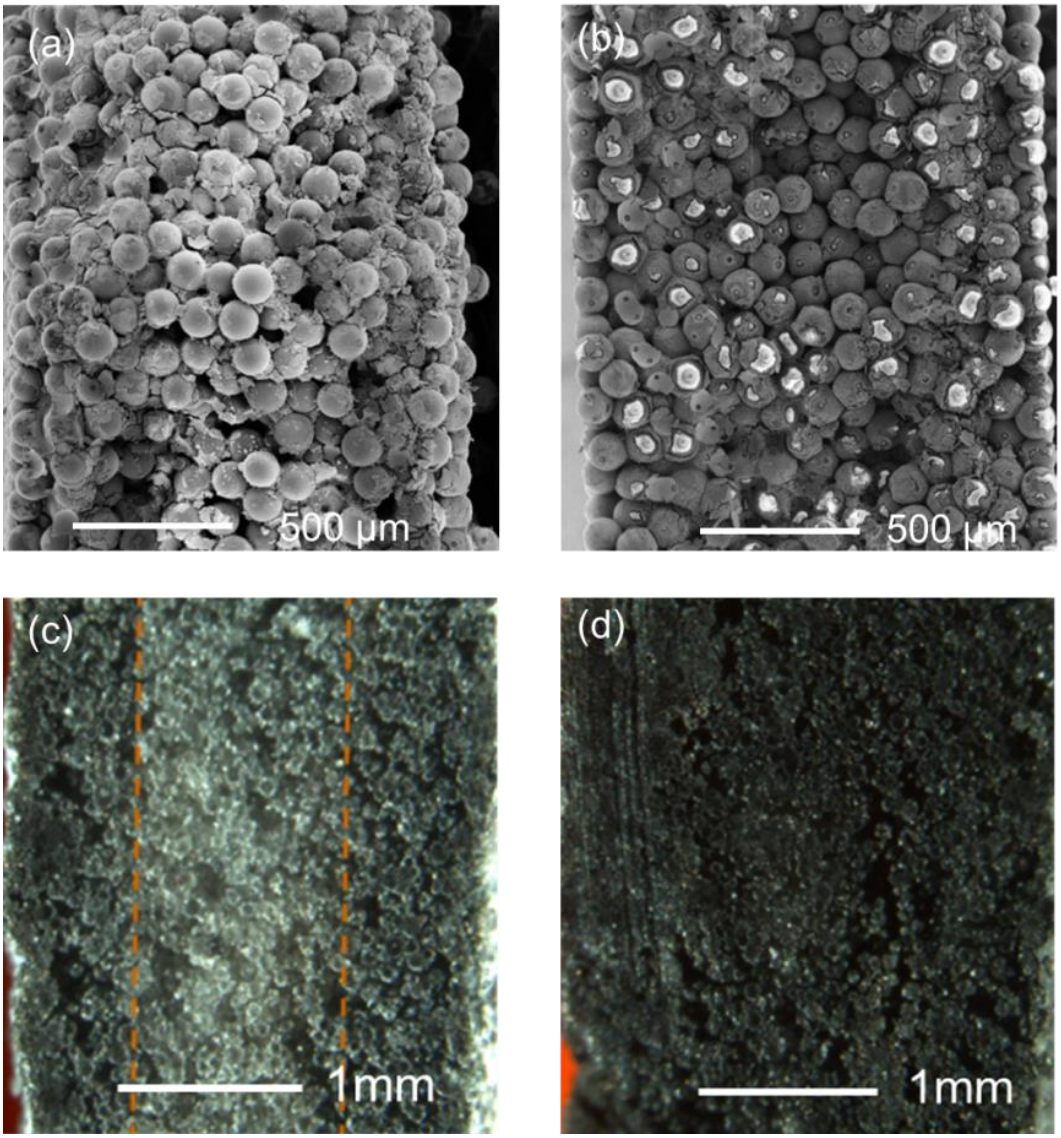

Figure 5-10. PMMA template plated with (a) conventional electroless deposition (b) the EPAELD process; Parafin template plated with (c) conventional electroless deposition (d) the EPAELD process

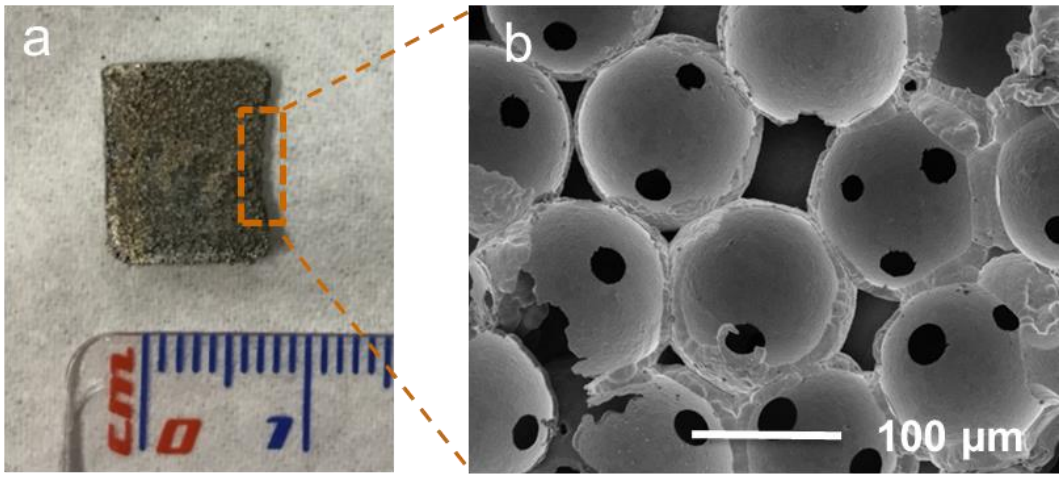

Figure 5-11. Ni foam generated via EPAELD PMMA template

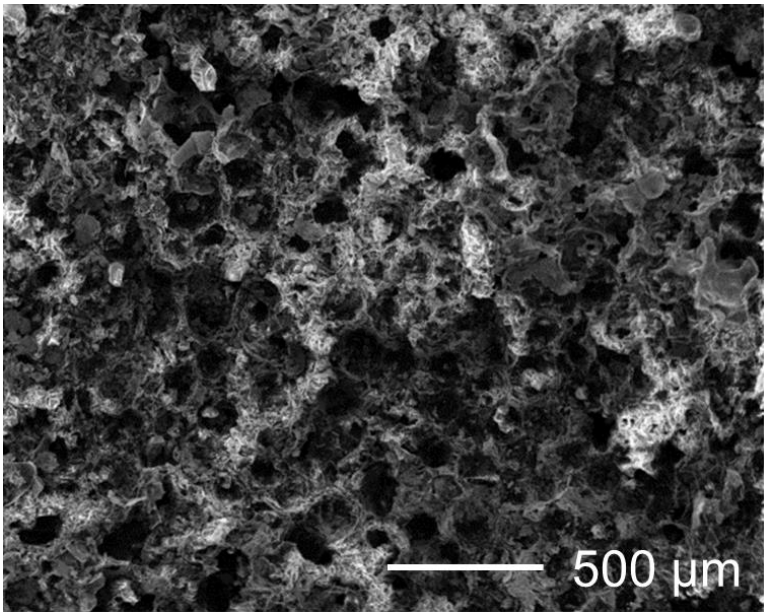

Figure 5-12. Ni foam generated via EPAELD paraffin template

5.4 CONCLUSIONS

The improved electroplating technique involving AC and vacuum is capable of fabricating bulk microcellular nickel foams, but with multiple defects and voids. The designed recovery process shows its effectiveness of reducing the Oxygen in nickel foam involved by an EAA removal process. In the electroplating of porous templates, AC superimposed DC shows a significant effect of regulating the nickel foam structure. Both high AC frequency and high AC voltage show positive effect on the uniformity of deposited nickel foams. The combination of a high frequency and high voltage leads to the densest deposited template. However, with the regulating effect on Ni structure, the electroplating technique with AC is still not capable of producing Ni structure with high uniformity.

A novel approach of electro polishing assisted electroless Ni foam deposition was developed and applied on the fabrication of bulk microcellular Ni foam with multilayers. Free standing and highly uniform bulk Ni foam was obtained by enhancing the electroless deposited one with an additional electrodeposition step.

Chapter 6. Modeling of the EPAELD Process

6.1 Introduction

As described in Chapter 5, an electropolishing-assisted electroless deposition (EPAELD) process was developed to overcome the inhomogeneous Ni deposition on close-packed polymer microspheres template. Since the EPAELD process involves many variables, for example geometric parameters of the sphere template, diffusion coefficient in porous media, and the rate for electrochemical reaction, a process model is needed to achieve fundamental understanding and to optimize the hybrid electroless deposition process. This chapter presents the development of a process model for the EPAELD process. The model suggests that the EPAELD process is cable of depositing Ni evenly across bulk polymer templates, which is not achievable using only either electroless or electro deposition. In addition, the sphere size in template, electrolyte concentration, and electropolishing current density are significant factors of the EPAELD process. Proper combinations of those factors for templates with different sphere size were predicted and suggested through parametric study to achieve the evenest Ni distributions across the templates.

6.2 Modeling Methods

A finite difference analysis of ion diffusion in porous media was conducted. The process model was developed to understand mechanisms of the developed EPAELD process and to predict proper conditions for templates with different sphere sizes.

6.2.1 Reaction kinetics of the electroless deposition process

The same as demonstrated in Chapter 5, the chemical reaction of the electroless deposition process for depositing nickel using a hypophosphite reducing agent is given in Equation (6-1). Ni^{2+} ions are reduced to Ni by hypophosphite [$H_2PO_2^-$] with palladium (*Pd*) as a catalyst.

$$Ni^{2+} + 4H_2PO_2^- + H_2O \xrightarrow{Pd} Ni + 3H_2PO_3^- + P + 1.5H_2 + H^+ \quad (6\text{-}1)$$

The volumetric rate of reaction in electroless deposition , *r*, has been determined as [97],

$$r = e \cdot k \cdot \frac{[\ H_2PO_2^-]}{[H^+]^{0.4}} \quad (6\text{-}2)$$

where *k* represents the reaction rate constant, [$H_2PO_2^-$] and [H^+] are ion concentrations, and *e* is an energy term defined as

$$e = exp(-\frac{E_a}{360R}) \cdot exp(\frac{E_a}{360R} \cdot \frac{T-360}{T}) \quad (6\text{-}3)$$

Ea in Equation (6-3) is the activation energy of the reaction, *R* is the idea gas constant, and *T* is the absolute temperature.

In this study, the pH of the electrolyte is stabilized with a buffering agent, and therefore [H^+] can be assumed constant. Hence the reaction rate at any given time is determined by [$H_2PO_2^-$]. Considering the Ni deposition reaction occurs in the interstitial space of the microsphere template, [$H_2PO_2^-$] will be affected by both the electroless deposition reaction and the diffusion of $H_2PO_2^-$ from the bulk electrolyte. Ion diffusion coefficient depends on the geometry of the porous microsphere template. As shown in Figure 5-1, the diffusion process is time varying

along the cross-section of the template after Ni deposition starts. Initially the template is fully saturated with electrolyte and Ni will be deposited homogenously due to the uniform $H_2PO_2^-$ concentration. Over time, a $H_2PO_2^-$ concentration gradient forms due to the ion consumption and diffusion from the bulk electrolyte. The Ni deposition rate will be faster near the template surface, which will further increase the steepness of the concentration gradient and limit the amount of $H_2PO_2^-$ diffusing into the template interior.

Therefore, the electroless reaction rate in this study is expressed as the following:

$$r(x,t) = e \cdot k \cdot \frac{C(x,t)}{C_H{}^{0.4}} \tag{6-4}$$

where t is time and x is the thickness location, $C(x,t)$ and C_H is the local $H_2PO_2^-$ and H^+ concentration, respectively.

6.2.2 Local $H_2PO_2^-$ concentration

The local $H_2PO_2^-$ concentration is affected by both diffusion and chemical reaction, and can be expressed as

$$C = C_i - C_r + C_D \tag{6-5}$$

where C_i is the initial concentration, *Cr* is the reduction due to reaction, and C_D is the addition due to diffusion. Before the electroless deposition process starts, the initial ion concentration $C_i = C_0$, the ion concentration in the bulk electrolyte. The reduction due to reaction *Cr* can be determined with Equation (6-4). The concentration due to diffusion C_D can be determined with Fick's second law as shown below,

$$\frac{dC}{dt} = -D\frac{d^2C}{dx^2} \tag{6-6}$$

The boundary condition at the template surface can be set as $C = C_0$ and $D = D_0$. According to Yu, *et al.* [98], the diffusion coefficient *D* in a porous media depends on the local porosity (ϕ) and tortuosity (τ), and can be determined using the following equation.

$$D = D_0 \cdot \left(\frac{\phi}{\tau}\right) \tag{6-7}$$

where D_0 is the diffusion coefficient of $H_2PO_2^-$ in bulk Ni electroless deposition electrolyte. For a close-packed sphere template, the tortuosity can be determined through porosity as [98]

$$\tau = 0.5\left(1 + \sqrt{1-\phi}\right) + \frac{\sqrt{\left(\frac{1}{\sqrt{1-\phi}}-1\right)^2+0.25}}{1-\sqrt{1-\phi}} \tag{6-8}$$

It can be seen that the local porosity and tortuosity during the electroless deposition process is a key parameter determining the ion diffusion coefficient. The local porosity changes as Ni is deposited onto the surface of the polymer microspheres. The thickness of Ni deposition can be observed under scanning electron microscopy to validate the process model. Therefore, the deposited Ni layer thickness is determined in this study.

6.2.3 Deposited Ni layer thickness

Figure 6-1 shows a geometric model of a close-packed microsphere template, with *ra* denoting the radius of the microsphere and Δx the distance between two adjacent layers of spheres. The ion concentration and diffusion coefficient of

$H_2PO_2^-$ in the bulk electrolyte are denoted as C_0 and D_0, respectively. The deposited Ni layer thickness is denoted as d_{Ni}.

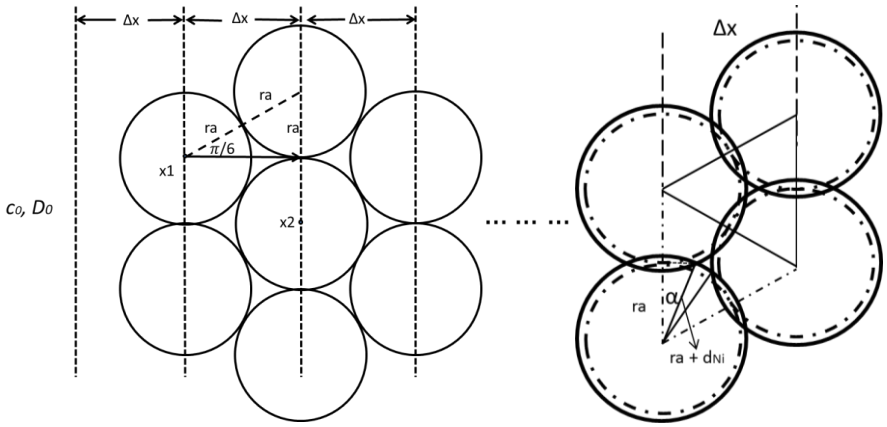

(a) (b)

Figure 6-1. A geometric model of the microsphere template (perpendicular to the 111 plane) before (a) and after (b) nickel deposition

Define a finite volume in the microsphere template to be

$$V=1\times1\times\Delta x \tag{6-9}$$

Given the porosity of the template, ϕt, the volume of the electrolyte is

$$V_t=\phi_t V \tag{6-10}$$

The volume of Ni deposited in the finite volume can be determined as

$$V_{Ni}(x) = \int r(x,t) \times V_t \, dt \tag{6-11}$$

The Ni thickness needed to seal the surface layer can be calculated following

$$d_{Ni-seal} = \frac{ra}{cos(\pi/6)} - ra \tag{6-12}$$

After the surface layer is completely sealed with deposited Ni and the polishing current is introduced, the number of Ni atoms converted to Ni^{2+} by polishing can be calculated with Equation (6-13). Although the local $Ni^{2+}$is increased by the polishing effect, the electroless deposition rate $r(x,t)$ will not be affected by Ni^{2+} but still dominated by $H_2PO_2^-$. Combined with the electroless Ni deposition rate, the number n is used to decide the Ni thickness polished off and also the porosity.

$$n = \frac{1}{z\ F}\int i(t)\,dt \tag{6-13}$$

where *i(t)* represents the polishing current, F is Faraday's constant, and z is the number of electrons transferred from each atom.

To obtain the local (layer wise) volume of net deposited Ni at time t and location x, the electroless deposition rate is needed and can be calculated with Equation (6-14). The Ni volume deposited at t in the layer can be described with the following equation,

$$v_{Ni}(x,t) = \int r(x,t)\cdot v\cdot \phi(x,t)\cdot \frac{M_{Ni}}{\rho_{Ni}}dt \tag{6-14}$$

where M_{Ni} is molecular weight of Ni, and ρ_{Ni} is density of Ni, v is the total volume under investigation.

In fact the deposited Ni volume in the three stages of the EPAELD process is different, and can be expressed as:

$$v_{Ni}(x,t) = \begin{cases} \frac{M_{Ni}}{\rho_{Ni}} \int r(x,t) \cdot V \cdot \phi(x,t)\, dt & Stage\ I \\ -\frac{M_{Ni}}{\rho_{Ni}} \times \frac{1}{z\ F} \int i_1(t)\, dt & Stage\ II \\ \frac{M_{Ni}}{\rho_{Ni}} \left(\int r(x,t) \cdot V \cdot \phi(x,t)\, dt - \frac{1}{z\ F} \int i_2(t)\, dt \right) & Stage\ III \end{cases} \quad (6\text{-}15)$$

The Ni thickness d along time is calculated from local volume of net deposited Ni and local surface area. Deposited Ni thickness at t, $d_{Ni}(x,t)$, can be calculated with the following equation,

$$d_{Ni}(x,t) = \frac{v_{Ni}(x,t)}{S(x,t)} \quad (6\text{-}16)$$

where $s(x,t)$ is the available surface area for Ni deposition.

The surface area of each interior layer (within the interval of Δx) is calculated with Equation (6-17). In a FCC model, each sphere is in contact with 12 neighboring spheres. Assuming the deposited Ni thickness is d_{Ni} the exposed surface area of each sphere can be determined as

$$S_1(x,t) = 4\pi(r_a + d_{Ni})^2 - \pi({d_{Ni}}^2 + {r_s}^2) \times 12 \quad (6\text{-}17)$$

where

$$r_s = \sqrt{(r_a + d_{Ni})^2 - r_a^2} \quad (6\text{-}18)$$

The first term in Equation (6-17) is the entire surface area of a sphere after nickel deposition; the second term is the total covered surface due to sphere overlapping. The total surface area can be found by multiplying $S_1(x,t)$ by the number of spheres in the volume of investigation.

The porosity $\phi(x,t)$ can be obtained by

$$\phi(x,t) = 1 - \frac{v_{Ni}(x,t)+(1-\phi_0)V}{V} \quad (6\text{-}19)$$

That is,

$$\phi(x,t) = \phi_0 - \frac{v_{Ni}(x,t)}{V} \quad (6\text{-}20)$$

where ϕ_0 is the initial porosity of the microsphere template.

6.2.4 Solution procedure

The developed model is solved with a finite difference procedure. It is easy to see that

$$\Delta x = 2 \cdot r_a \cdot cos\frac{\pi}{6} \quad (6\text{-}21)$$

Due to geometric complexity, we assume Δx to be the smallest thickness interval within which the ion concentration is uniform. Inhomogeneous Ni deposition and variable diffusion coefficient along the cross section are taken into account and the template is divided into 20 layers for the PMMA template and 60 layers for the paraffin template. The number of spheres in each layer is chosen to be 10,000. The model was developed in Matlab 2013R (MathWorks Inc.) applying the input values listed in Table 6-1. The values of E_a, K, and D_0 were obtained by fitting the model to experimental data. A flow chart of the simulation is shown in Figure 6-2.

Table 6-1. Values applied in this study

ra: 0.005 cm	c_0 : 0.3 mole/L
pH value: 8.5	T : 298.15 K
$[H+]$: $1\times10^{-8.5}$	$\emptyset_0$: 0.26
R: 0.2871 J/g·K	F : 9.649×10^{7} mA·s/mole
E_a: 560 J/g	Z : 2
K: 1.237×10^{-3} mole/L·s	
D_0 : 9.7×10^{-5} cm^2/s	

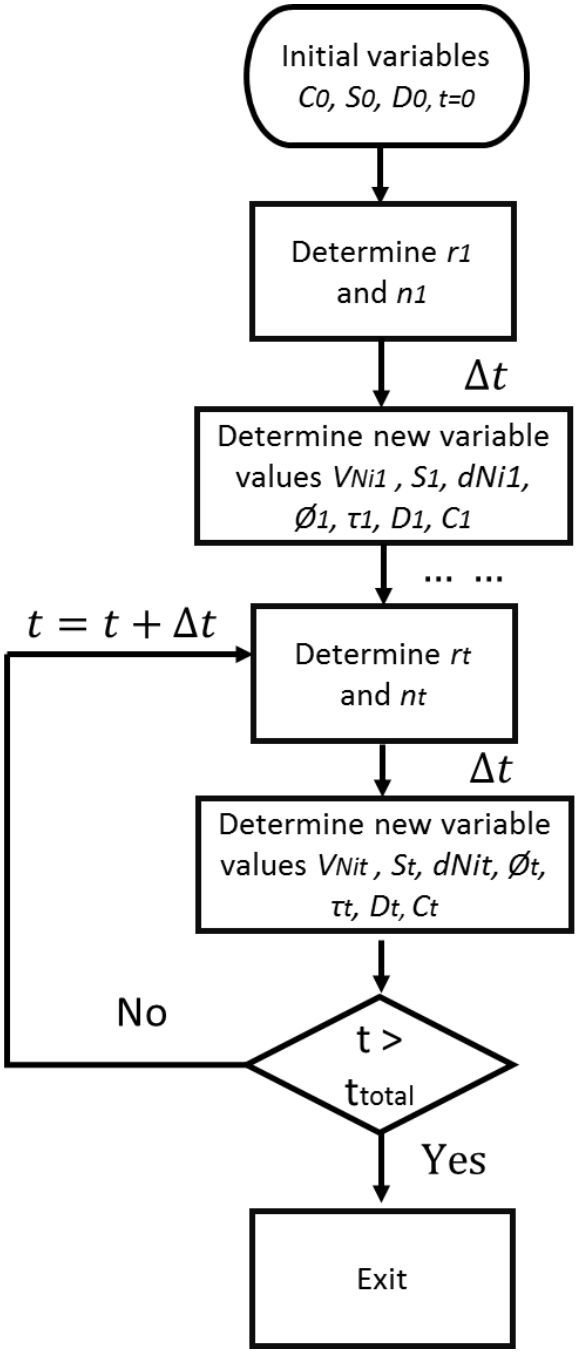

Figure 6-2. A flow chart of the EPAELD simulation process

6.3 Results and Discussion

6.3.1 Model validation

The model was then validated by matching the prediction results with regional Ni thickness measured from the SEM of a fabricated sample. Figure 6-3 shows the cross section of a template after four hours of electroless Ni deposition. Thickness of Ni deposited on different layers were measured with Image J and listed in Table 6-2. Measurements were taken at multiple locations. The data shown in the table is average and range. The experimental values and predicted values of Stage 1 of the process are compared in Figure 6-4.

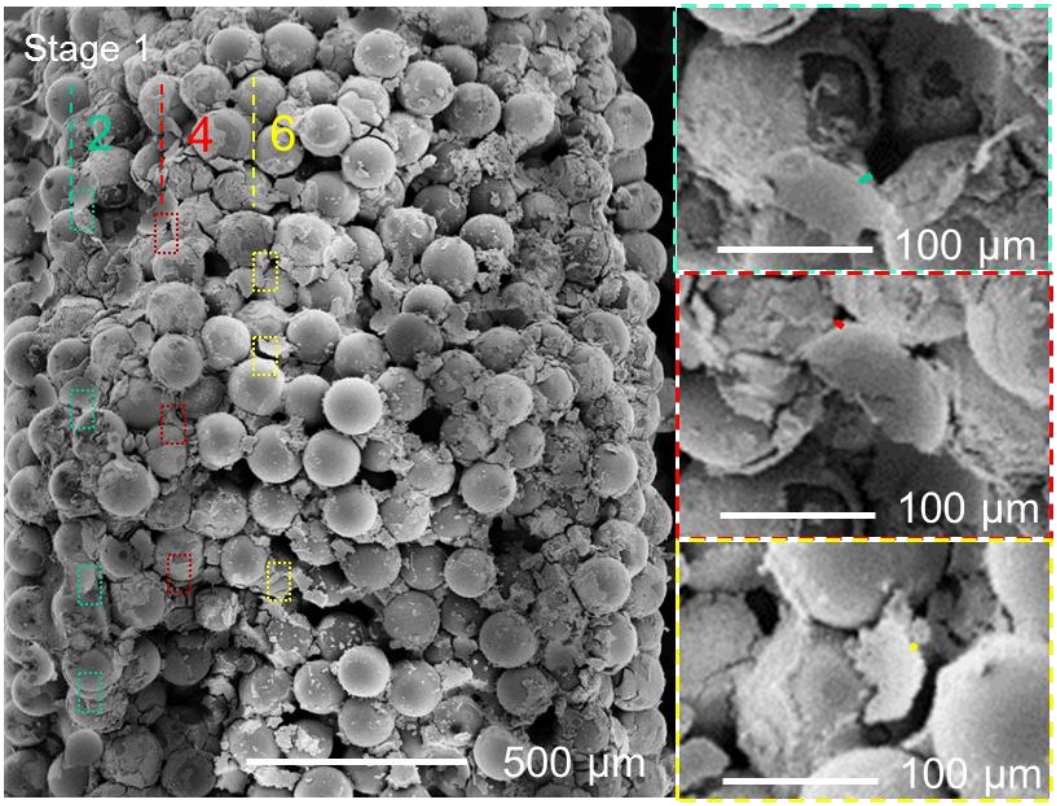

Figure 6-3. Cross section image of template electroless deposited for 4 h.

Table 6-2. Average Ni thickness measured from Layers 2, 4, and 6

Location (layer)	Ni thickness (μm)
2	5.51 (+/- 0.5)
4	3.31(+/- 0.6)
6	2.32 (+/- 0.3)

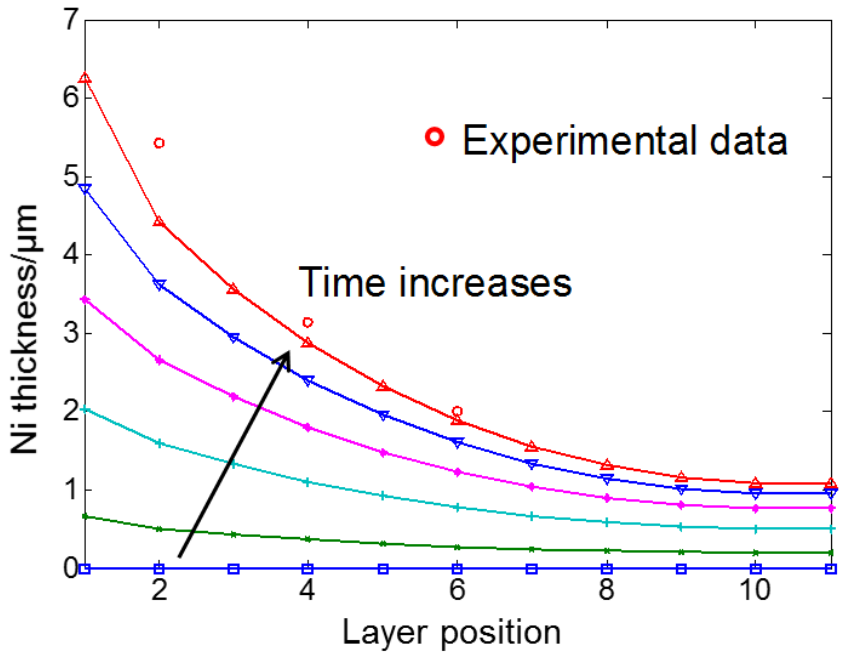

Figure 6-4. The measured and predicted Ni thickness of at the end of Stage 1.

The Ni thickness at different times during Stages 2 and 3 were predicted with the model and shown in Figure 6-5. In Stage 2, the polishing current was exponentially distributed to all the conductive layers (redistributed when a layer became Ni free and electrically non-conductive). According to Equation (6-12), the Ni thickness needed to seal layer 1 is 7 μm. The Ni thickness of Layer 1 decreased from 6.4 μm to 4.8 μm indicating the opening of surface channels. On other layers, more Ni was polished off due to the relatively lower electroless deposition rate from the lower ion diffusion coefficient. At the end of Stage 2, only the first five layers were still Ni coated. Open ion diffusion channels were created while electrical conductivity was maintained for current introduction in Stage 3. In Stage 3, the 4 mA/cm^2 current was exponentially distributed to the first five layers initially and was redistributed when more layers gained conductivity. There is almost no Ni thickness change on the first layer due to the balanced polishing and deposition rate. From Layer 2 to 5, the Ni thickness increased initially because of the relatively thin Ni layer (high D and r), and reached a steady state with Ni build-up and the shrinking of ion diffusion channels. With a constant ion diffusion channel size, ions were allowed to diffuse to deeper inside resulting in a relatively homogeneous Ni deposition along the cross section as shown in Figure 6-5 (b). This agrees well with experimental result shown in Figure 5-10 (b), where the cross section of the sample was fully plated at the end of Stage 3.

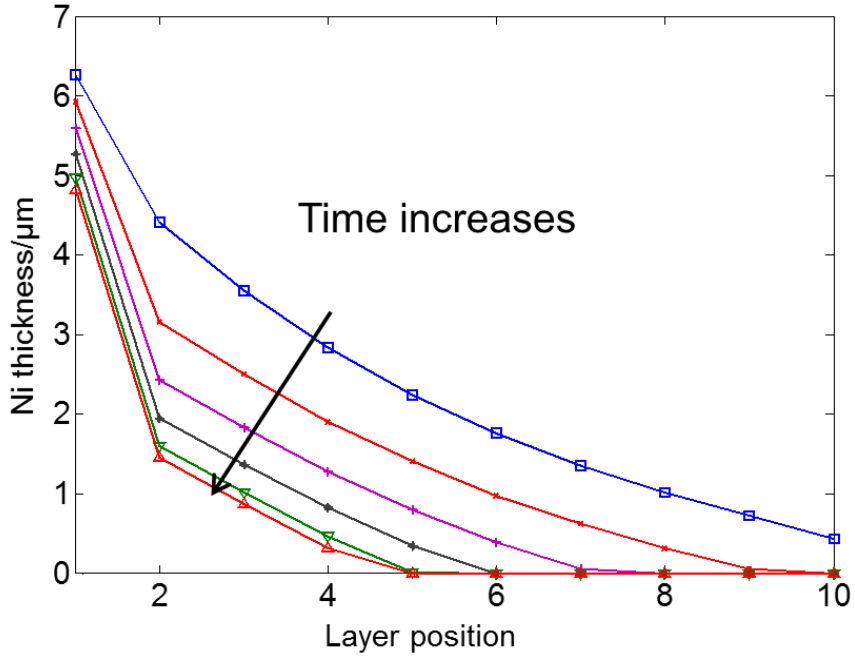

(a)

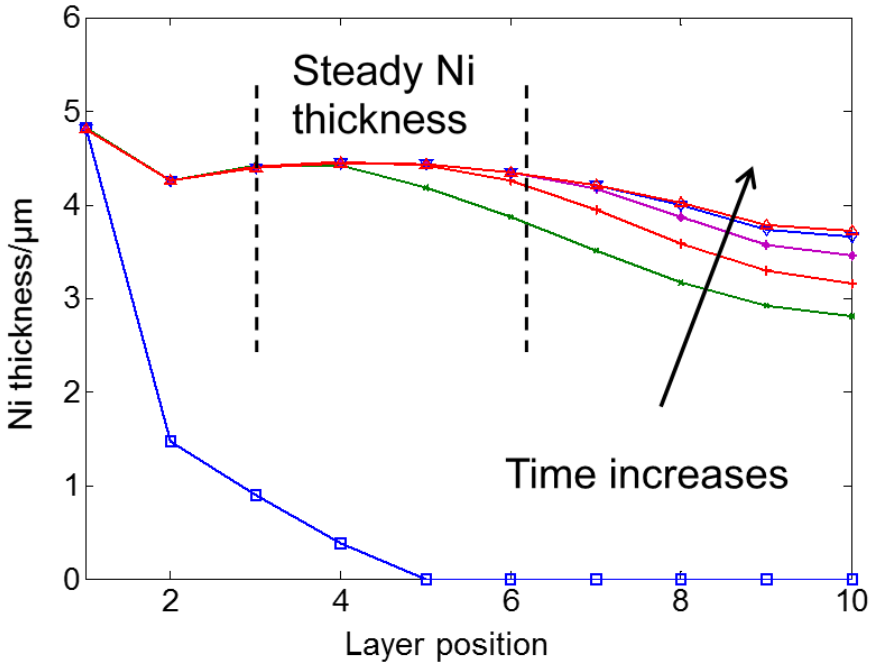

(b)

Figure 6-5. Ni thickness from model in Stage 2 (a) and Stage 3 (b).

6.3.2 Parametric study

6.3.2.1 PMMA template

The experimental study in this work was conducted by selecting conditions based on our previous electroless/electro Ni deposition experiences. In order to investigate the effects of parameters and optimize the processing conditions, a parametric study was conducted employing different electrolyte concentrations, polishing current densities, and depositing/polishing time. In Stage 1, the effect of $H_2PO_2^-$ concentration and electroless deposition time were investigated. Three different electroless deposition times of 2, 4, and 6 h were selected, and correspondingly three $H_2PO_2^-$ concentrations of 0.1, 0.3, 0.5 mol/L were applied. The final Ni thickness of each condition combination was determined and illustrated in Figure 6-6. The purpose of Stage 1 is to coat the exterior regions of the template with Ni to obtain electrical conductivity with a short deposition time. Among the applied conditions, several combinations of 0.3 mol/L, 2 h, 0.5 mol/L, 2 h, and 0.1 mol/L, 2 h provided a Ni thickness of about 2 μm in interior regions while leaving the surface layer unsealed (surface would be sealed if Ni thickness was larger than 7 μm). With these conditions, Stage 2 could be eliminated and a lower current density could be used for Stage 3 processing. Other conditions either required a longer time or generated unsuitable Ni thickness. The curve of Ni thickness from a concentration of 0.3 mol/L and a processing time of 2h was selected as the starting curve for the simulation in the next stage.

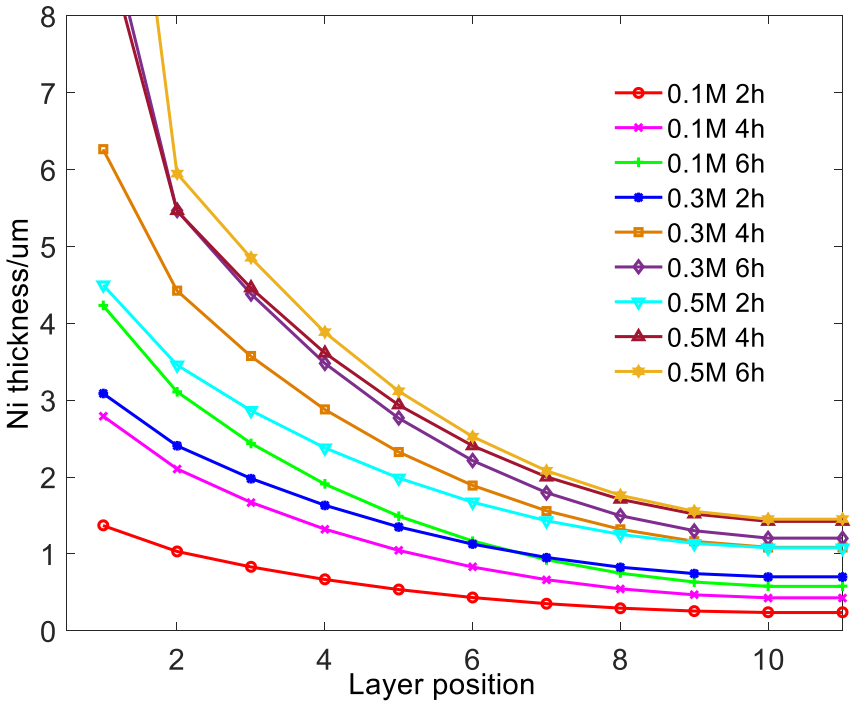

Figure 6-6. Ni thickness from different parametric combinations in Stage 1 (100 μm sphere)

In Stage 3, $H_2PO_2^-$ concentration was kept at 0.3 mol/L. The effects of current density and depositing/polishing time were investigated. Four different current densities of 1, 3, 4, and 6 mA/cm^2 (2 cm^2) were selected; three polishing times of 10, 15, and 20 h were employed. The final Ni thickness of each condition combination was determined and shown in Figure 6-7. It can be found that at a fixed polishing current density, the selected polishing time has no significant effect on Ni thickness distribution along the cross section of the template after 15 h of deposition. In the first 15 h, Ni thickness increases because the deposition rate is higher than polishing rate. After 15 h, the deposition rate reaches a balance with the polishing

rate due to the declining $H_2PO_2^-$ diffusion caused by the reduced channel size between spheres. Current density has a significant effect on Ni thickness and distribution. When current density is lower than 4 mA/cm^2, Ni accumulates on the surface layers faster than what can be polished away, which results in a low $H_2PO_2^-$ concentration and thin Ni layers in the interior region. When 4 mA/cm^2 is applied, Ni thickness on near-surface layers is maintained at 4.5 μm, providing a constant $H_2PO_2^-$ diffusion to interior regions and depositing Ni evenly through the cross section. When 6 mA/cm^2 was applied, the Ni thickness was reduced from 2 μm to 1 μm after 10 h because the polishing rate exceeded the Ni deposition rate. While a detailed study will be needed to determine the optimal polishing current density, for simplicity, 4 mA/cm^2 is used in this study for the PMMA template.

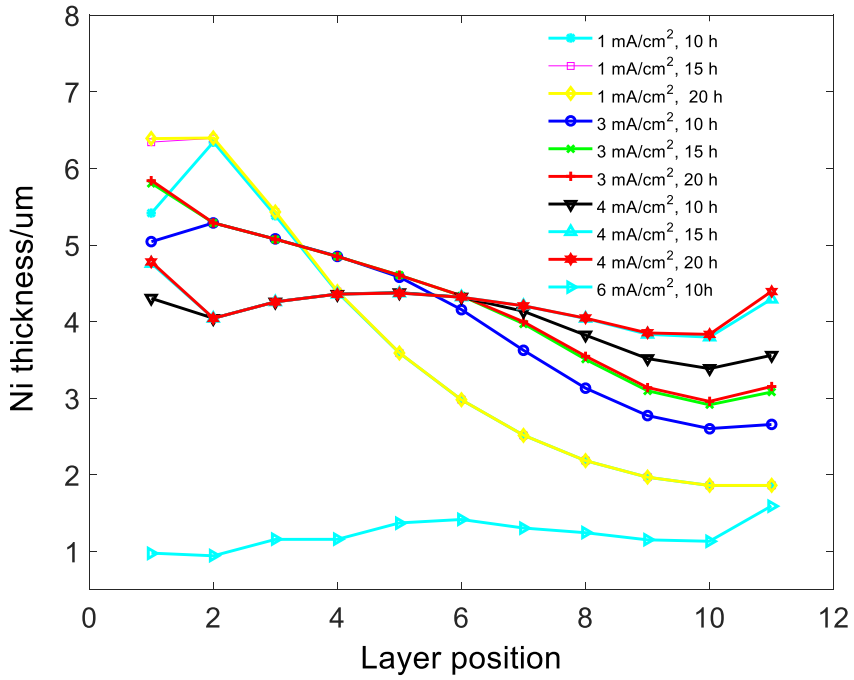

Figure 6-7. Ni thickness from different parametric combinations in Stage 3 (100 µm sphere)

6.3.2.2 Templates of smaller spheres

In order to provide a guideline for Ni deposition on templates made with smaller spheres, a parametric study was conducted on templates with 10 µm spheres. Again, the effects of $H_2PO_2^-$concentration and electroless deposition time were investigated in Stage 1. Three different electroless deposition times of 1, 2, and 4 h were selected and corresponding to each time three $H_2PO_2^-$concentrations of 0.1, 0.3, 0.5 mole/L were applied. The final Ni thickness of each condition combination was determined and shown in Figure 6-8. It was found that Ni thickness increased with increasing time and $H_2PO_2^-$ concentration. In this case Ni thickness was less than 0.2 µm indicating a potential weak electrical conductivity. Among all the conditions, 0.5 mol/L, 2 h and 0.3 mol/L, 2 h provided the two Ni thicknesses larger

than 0.05 µm with an unsealed surface layer (Ni thickness close to 0.7 µm would seal the surface). According to Jun *et al.* [99], Ni is normally deposited as clusters with a diameter of around 0.05 µm. If the predicted Ni thickness is smaller than this value, the continuity and electrical conductivity of a Ni layer, which is required by Stage 3, cannot be guaranteed. Therefore, the predicted curve of Ni thickness from 0.5 mol/L, 2 h was selected for the starting curve for the next stage simulation.

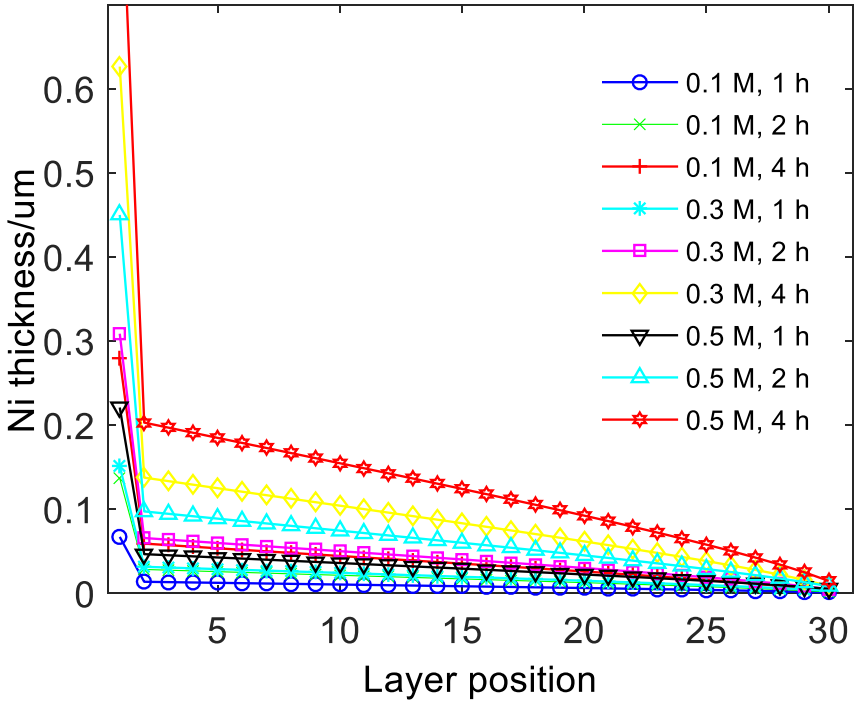

Figure 6-8. Ni thickness from different parametric combinations in Stage 1(10 µm sphere)

In Stage 3, the $H_2PO_2^-$ concentration was kept at 0.5 mol/L and the effects of current density and deposition/polishing time were investigated. Considering that the thin Ni layer is more sensitive to current density, five different current densities of 0.5, 1, 3, 4, and 6 mA/cm^2 (2 cm^2) were selected, and polishing times of 10, 15,

and 20 h were employed. The final Ni thickness of each condition was determined and shown in Figure 6-9. Ni thickness and distribution reached a steady state at 15 h, the same amount of time required by the 100 μm template. The effect of current density on Ni thickness and distribution was significant. When the current density is 0.5 mA/cm^2, the current is able to maintain the surface open and generate a relatively even Ni thickness initially. However, with the Ni building up, interior layers gain electrical conductivity, and the weakened surface current density is not able to stop the increasing of the surface Ni thickness. When 1 mA/cm^2 is applied, the Ni thickness on near-surface layers was maintained at 0.55 μm providing a constant $H_2PO_2^-$ diffusion to interior regions. Ni was deposited evenly along the cross section after 15 h of electropolishing assisted deposition. When current densities higher than 1 mA/cm^2 were applied, Ni thickness was decreased due to the increased polishing effect. With a current density of 6 mA/cm^2, Ni on the first five layers was polished off completely after 10 h and a gradient of Ni distribution was generated. All the applied currents were high enough to keep the surface open and allow the ion diffusion to interior. Among the conditions tested, 1 mA/cm^2 provided the thickest Ni layer for the 10 μm sphere template.

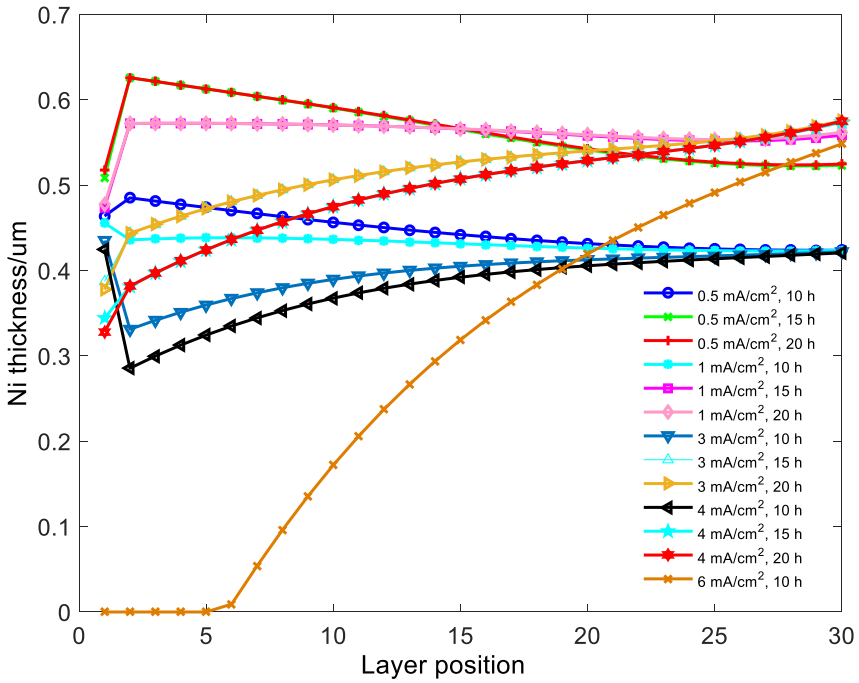

Figure 6-9. Ni thickness from different parametric combinations in Stage 3 (10 µm sphere)

6.4 CONCLUSIONS

A finite difference model was developed to understand the previously developed electropolishing assisted electroless Ni deposition process. The $H_2PO_2^-$ diffusion and Ni deposition along the template cross section were modeled using Fick's second law and empirical kinetic equations. The interaction among $H_2PO_2^-$ diffusion, Ni deposition, and Ni polishing were studied with the model. The model showed the effectiveness of polishing current on keeping template surface open and generating even Ni deposition across the template. The model was validated with measured Ni thickness in the proposed process. For the conditions studied in this research, template sphere size, electrolyte concentration, and electro-polishing current illustrated significant effects on the deposited Ni thickness and thickness

distribution. When the sphere size in a template became smaller, the electroless deposited Ni thickness was thinner than that deposited under the same electrolyte concentration and depositing time (2h and 4h). Smaller sphere size also resulted in a bigger difference between Ni thicknesses on the first layer and second layer. In the EPAELD process, a narrow operating range of conditions is available for templates with smaller spheres owing to the requirement of maintaining electrical conductivity of the template. A proper electrolyte concentration was needed in both 10 μm and 100 μm sphere templates to obtain a balance between Ni thickness and electroless depositing time in Stage 1. A high electrolyte concentration would result in the close of surficial channels in a short time while interior was not deposited. As a contrary, a low electrolyte concentration would result in a long depositing time and a thin Ni thickness leading to low electrical conductivity. 0.3 mol/L and 0.5 mol/L were found to be suitable concentrations for 100 μm sphere template and 10 μm sphere template, respectively. Both concentrations resulted in the proper Ni thickness (100 μm template: ion diffusivity is a priority considering the relatively thicker Ni layer; 10 μm template: electrical conductivity needs to be secured considering the relatively thin Ni layer) while keeping surficial channels open at a moderate electroless depositing time of 2h. Regarding the electro-polishing current density, a high value would result in the polishing off of surficial Ni layer, and so as to termination of the EPAELD process; while a low value would not be capable of keeping the surficial channels open to generate an even interior Ni deposition. 4 mA/cm^2 and 1 mA/cm^2 provided the evenest Ni thickness distribution on 100 μm and 10 μm templates respectively.

Chapter 7. Microcellular Three Dimensional Graphene Foams

7.1 INTRODUCTION

Three-dimensional (3D) graphene foams are attracting significant interests due to their superior electrical and thermal properties and potential applications in high performance lithium-ion batteries and super capacitors [3, 15, 42, 43, 100, 101]. In these energy storage applications, the graphene foam is used as an electrode with active materials infiltrated in the pores. Comparing to conventional electrode designs, this configuration provides a much larger contact surface and shorter charge transfer distance between the active material and current collector. As a result, 3D graphene foam-based batteries and super capacitors could have an extremely high load capacity, as well as fast charging and discharging rates [15, 102, 103].

Recent studies have demonstrated 3D graphene foams with pore sizes on different length scales. With commercially available Ni foams as a template, a chemical vapor deposition (CVD) method has been used to fabricate 3D graphene foams with a pore size on the level of several hundreds of micrometers [15-17]. Such a large pore size leads to a relatively low specific surface area and long charge transfer path, resulting in a slow charging and discharging rate for the energy storage device. Furthermore, large pore-sized graphene foams tend to be brittle and can cause structural problems in subsequent handling. Graphene foams of nanometer pore sizes were fabricated with a lithographically-defined polymer foam as a template [18]. Amorphous carbon foam was first obtained by patterning a photoresist polymer structure followed by a pyrolysis step. The amorphous carbon foam was then sputter-coated with Ni and annealed to obtain a graphene layer on the pore walls

W. Jiang, H. Xin, W. Li, Microcellular 3D graphene foam via chemical vapor deposition of electroless plated nickel foam templates, Materials Letter, Volume 162, 1 January 2016, Pages 105–109.

W. Jiang: Design and implement involved work, construct manuscript
H. Xin: Conduct partial characterization and edit the constructed manuscript
W. Li: Direct and supervise the work as supervisor

of the carbon foam. Nickel was subsequently dissolved, with the amorphous carbon remaining as a structural support for the nanoporous graphene layer. Graphene foams with a pore size on the level of a few micrometers have also been fabricated, but only through a self-assembly method [104]. Graphene oxide (GO) platelets and polystyrene (PS) microspheres were first dispersed in solutions separately and then mixed and filtered through a membrane filter. The PS spheres were then removed with solvent to obtain the 3D graphene structure.

When it comes to the energy storage application, small pore-sized graphene foams are generally desirable for high loading of active materials and, at the same time, fast charging/discharging rates. However, as the pore size becomes nanoscale it presents a challenge for active materials to infiltrate into the porous structure due to the surface tension effect. Another challenge for nanoporous graphene foam is that the fabrication process so far has been limited to produce thin layer materials in the range of 10-25 μm [105]. Thicker graphene foams are needed to satisfy the high loading requirement of energy storage devices.

In this chapter, a fabrication process for microcellular 3D graphene foams with a pore size on the level of 1 to 100 μm is reported. The thickness of the foam is targeted at the millimeter level. Using the microcellular bulk Ni foam introduced in Chapter 5, an atmospheric pressure CVD (APCVD) process was employed to obtain thick microcellular graphene foams. This chapter presents the fabrication and characterization of the microcellular graphene foam and shows that the nickel foam template obtained in this study is thermally-stable for the APCVD growth of microcellular graphene foams.

7.2 EXPERIMENTAL

7.2.1 Processing

Fabricated Ni foam templates were loaded in a 1-inch fused quartz tube furnace (TF55035A-1, Linderburg/Blue M). The tube was first evacuated, then purged with a gas mixture of Ar (80 sccm, 99.999%, Airgas) and H_2 (20 sccm, 99.999%, Airgas) until reaching the atmospheric pressure. The furnace was heated up to 850 °C at the highest rate and held at this temperature for 10 min to anneal the Ni foam under flowing Ar (40 sccm) and H_2 (10 sccm). The Ni foam was then exposed to 40 sccm Ar, 5 sccm H_2, and 5 sccm CH_4 (99.999%, Airgas) for 10 min before cooling down to room temperature at a rate of 10 °C min^{-1}. During the process, a few layers of graphene grew on the surface of nickel foam. The graphene-nickel composite was submerged in 0.5 M $Fe(NO_3)_3$ (Aldrich) aqueous solution at 80 °C for 20 h to dissolve the Ni substrate. The graphene foam was washed with deionized water, rinsed with isopropanol and dried in the ambient environment for characterization.

7.2.2 Characterization

The specific area of obtained Ni foam was measured with a Quantachrome® ASiQwin™ surface area analyzer. Density of the Ni foam was obtained by measuring its dimensions and weight. The graphene foam was examined using SEM before and after the nickel removal. After the nickel removal, the graphene foam was analyzed with a Raman spectrum analyzer (Witec Alpha 300). Strut walls of the obtain graphene foam was examined with a transmission electron microscope (TEM) (JEOL 2010F).

7.3 Results and Discussion

Figure 7-1 shows the optical and SEM images of the obtained Ni foam template after the PMMA spheres were removed. An optical image of the sample is shown in Figure 7-1 (a), with a bulk size of 10×12×1.5 mm^3. As introduced in Chapter 5, the density of the Ni foam obtained was measured at 0.05 $g \cdot cm^{-3}$ and the specific area at 5.00 $m^2 \cdot g^{-1}$. The specific surface-to-volume ratio was thus determined to be 2.5×10^5 $m^2 \cdot m^{-3}$, which is 50 times larger than that of commercial Ni foams (typical commercial Ni foams have a 0.01 $m^2.g^{-1}$ specific area and ~0.5 $g \cdot cm^{-3}$ density).

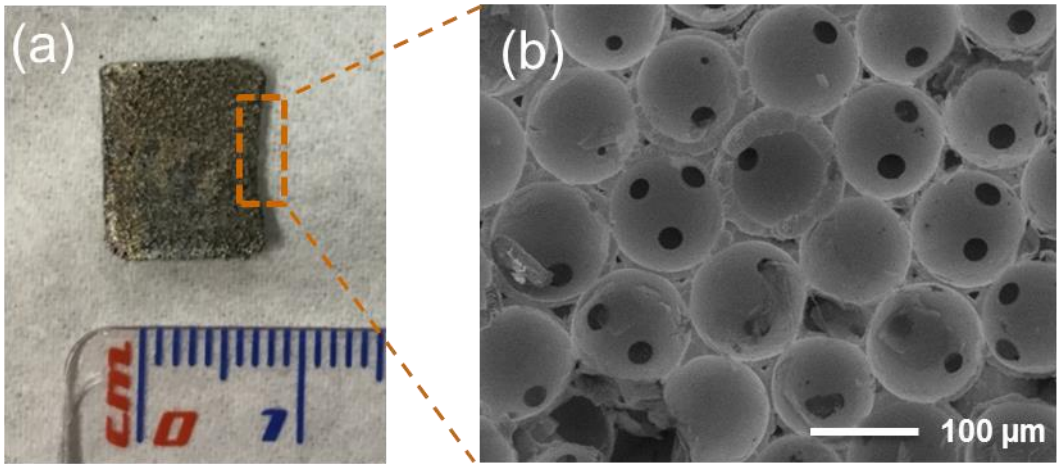

Figure 7-1. The Ni foam produced by EPAELD on PMMA template

Figure 7-2 introduces the Ni foam after graphene CVD. Fig7-2 (a) shows the morphology of Ni foam after 20 min annealing and 10 min graphene growth at 850 °C. Figure 7-2 (b) shows the graphene grains replicated those of the Ni foam substrate, suggesting that the Ni grain size was approximately 10 μm after annealing. Figure 7-3 shows the fabricated graphene foam after Ni etching off. The overall

foam size was 10×12×1.5 mm^3 as replicated from the nickel foam template. Figures 3(a) and (b) show that graphene grew on the surface of pore walls with a graphene grain size of approximately 10 µm across. Figures 3(c) and (d) show the free standing graphene foam structure after the nickel template was removed. A transmission electron microscopy (TEM) image of the pore wall is shown in Figure 7-4, indicating a 5 nm thick pore wall comprising of 15 layers of graphene for the obtained microcellular graphene foam. The Raman spectrum in Figure 7-5 has a 2D peak and a G peak with an intensity ratio of 1:3, confirming the few layer graphene (FLG) foam structure.

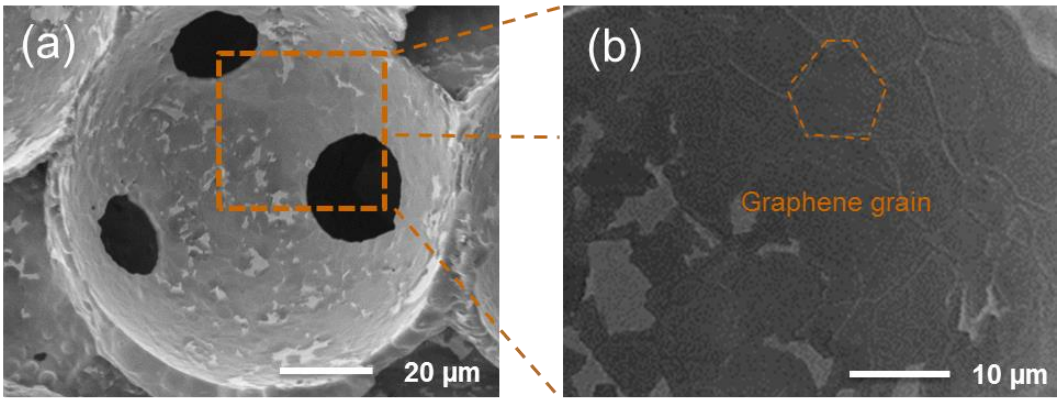

Figure 7-2. One cell of the Ni foam after graphene growth

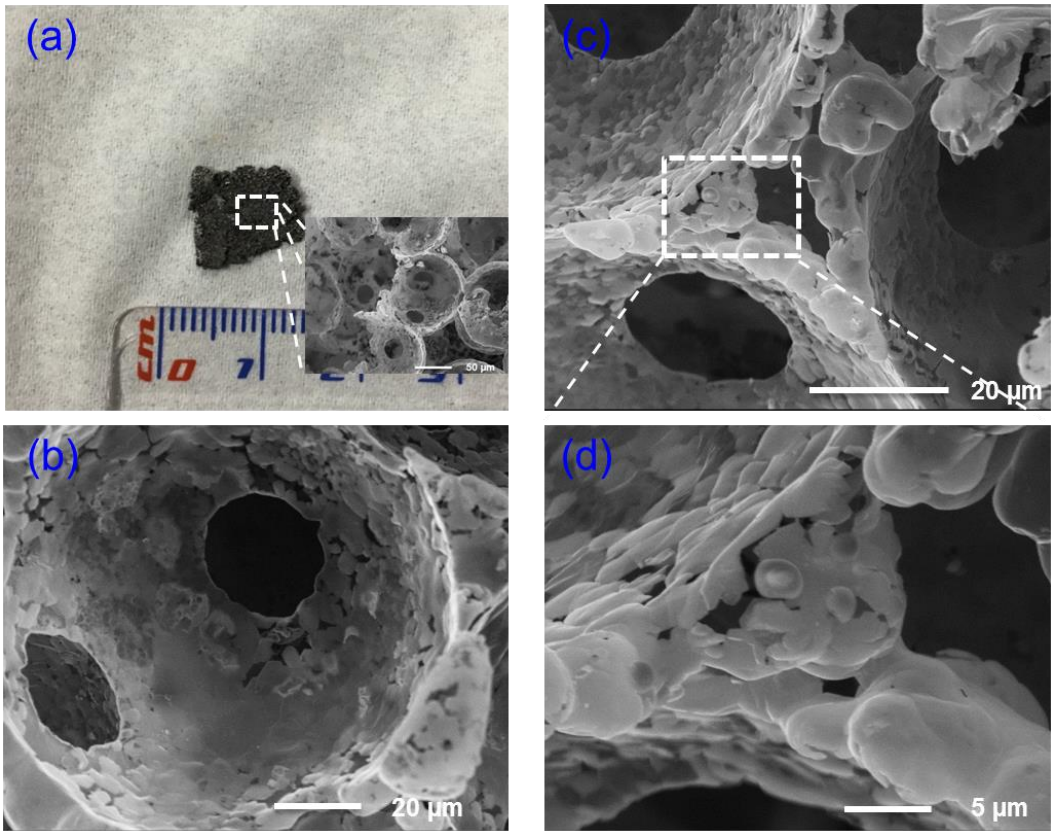

Figure 7-3. SEM images of fabricated graphene foam after Ni etching out: (a) overall picture, (b) a cell of the graphene foam, (c) free standing graphene foam after the nickel template was removed, (d) an exploded view of a joint region of three pores

The density of the obtained FLG foam in this study was measured at 0.0020 $g \cdot cm^{-3}$. This value is about two times that of a similar graphene foam structure reported by Ji, *et al.* (~0.0010 $g \cdot cm^{-3}$) [106]. However, the surface area of our foam is ~50 times larger, because the pore size of our foam is about 4 times smaller than that previously reported. The pore size of the graphene foam can be further reduced by using smaller pore-sized nickel foam templates. However, it should be noted that the pore size of nickel foam cannot be too much smaller, as the thermal stability of

smaller pore-sized nickel foams could prevent the formation of the cellular porous structure of graphene foams in the CVD graphene growth process.

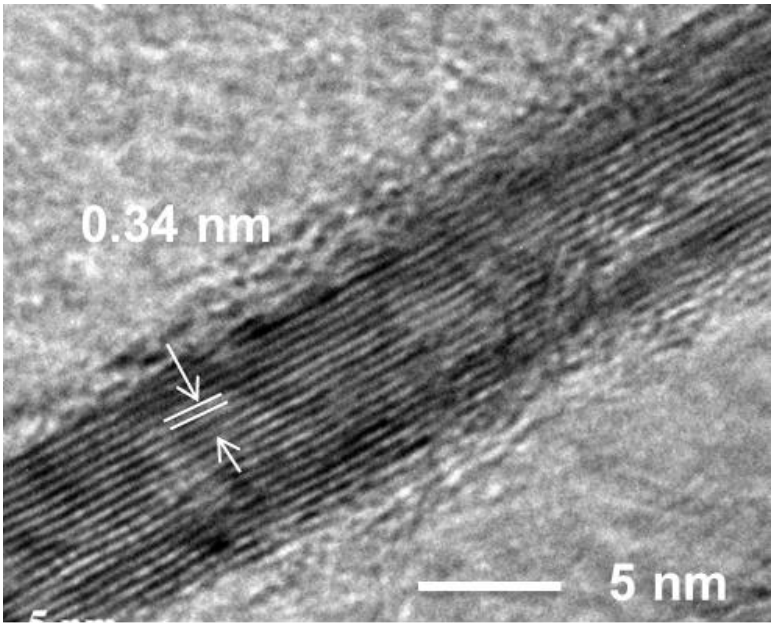

Figure 7-4. TEM image showing the thickness and number of layers of graphene strut wall

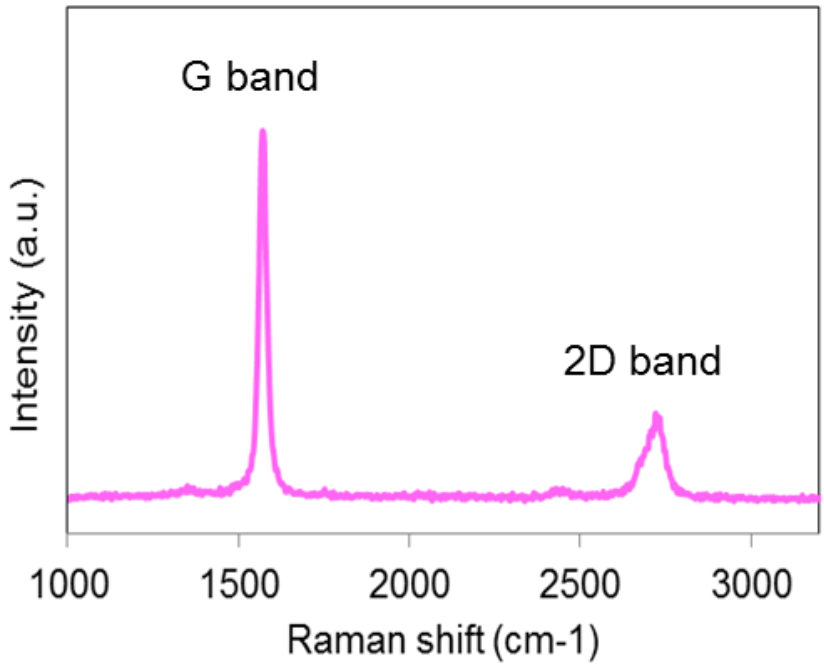

Figure 7-5. The Raman spectrum of the graphene foam

To fabricate 3D graphene foams using a CVD process, the sacrificial Ni foam template has to be able to withstand a temperature above 850 °C [107]. According to Yu *et al.* [108] and our previous work with ethylene acrylic acid (EAA) microspheres (1–10 µm diameter) [109], Ni foams with a pore size smaller than 10 µm will collapse at the temperature for the CVD graphene growth. The Ni foam from Yu *et al.* had a pore size around 2 µm and lost its porous structure at 600 °C. Figures 7-6 (a) and (b) show the morphology change of our small pore-sized Ni foam patterned with an EAA microsphere template. The average pore size was about 10 µm. After annealing at 850 °C for 30 min, the 10 µm spherical cells collapsed into a coral-like structure.

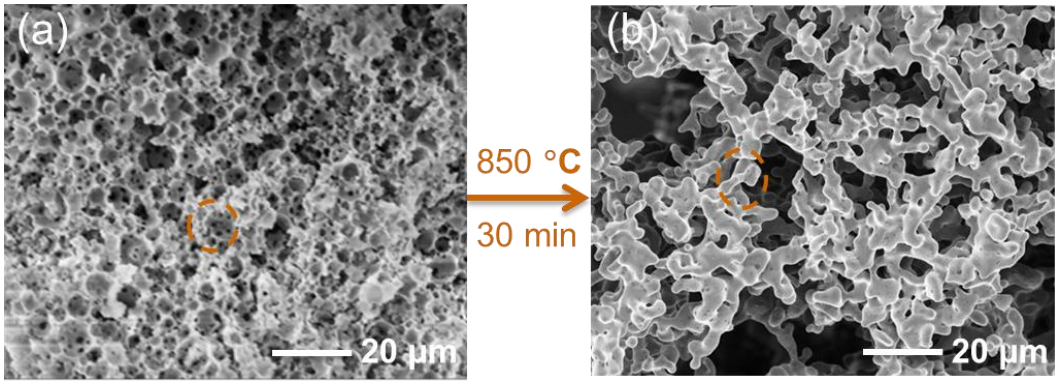

Figure 7-6. (a) Ni foam obtained with EAA microsphere template (pore size 10 µm). (b) The 10 µm nickel foam lost its cellular structure after 30 min annealing at 850 °C.

The collapse of cellular structure in small pore-sized Ni foams is the result of grain growth of electroplated Ni to minimize the surface energy under elevated temperatures. According to Klement *et al.* [110], electroplated Ni is mostly nanocrystalline with an average grain size around 20 nm. However, the CVD graphene growth process introduces high thermal energy and large grain growth potential. Larger grains are expected to form. When the grain size is larger than the strut thickness of Ni foam, the grain growth will exert a large surface tension on the cellular foam structure, causing it to collapse in order to achieve a lower surface energy state. The strut thickness of the coral-like nickel foam structure is approximately 10 µm, while the cellular nickel foam structure has a much smaller pore wall thickness. As the pore size becomes larger, the pore walls become thicker, bringing thermal stability to the nickel foam template for the CVD graphene growth. The microcellular nickel foams fabricated in this study (with a pore size ~100 µm) were sufficiently stable in the CVD process to fabricate 3D graphene foams.

7.4 CONCLUSIONS

A fabrication process for microcellular 3D graphene foams is demonstrated with ambient pressure chemical vapor deposition of Ni foam templates. The microcellular Ni foam templates introduced in Chapter 5 exhibited sufficient thermal stability for few layer graphene growth in the APCVD process, yielding graphene foams with a pore size less than 100 μm, density of 0.0020 $g \cdot cm^{-3}$, and pore wall thickness of 5 nm. The 3D graphene foam has a cellular morphology with surface-to-volume ratio of 2.5×10^5 $m^2 \cdot m^{-3}$ and is expected to find applications in energy storage devices for balanced high loading and fast charging and discharging rates.

Chapter 8. Summary and Future Work

8.1 SUMMARY

Hydrophilic polymer microsphere templates and hydrophilic polymer foams with micro and nano-sized open cells were fabricated in this study. PMMA, paraffin, and EAA templates were fabricated via assembly of hydrophilic microspheres. Hydrophilic PEG/BPS polymer foams with two levels of pore size (micro and nanometers) were fabricated via solid state foaming. The sphere assembled templates were used to fabricate nickel foams via a novel electropolishing assisted electroless plating method. An ethanol based electroless plating solution was used to enhance the diffusion coefficient of electrolyte in the porous structure. A finite difference model was developed to explore mechanisms of the newly developed nickel foam plating method. The model was also used to determine suitable plating conditions for nickel foams with different cell sizes. The fabricated nickel foams were employed as a template for producing 3D few layer graphene foams. As a special application, the fabricated PEG/BPS foams were tested for water and air diffusivities.

The major contributions of this work are summarized below.

- Hydrophilic polymer micro templates were fabricated with microspheres featuring different size ranges. Hydrophilic paraffin spheres were fabricated using a simple water/oil emulsion approach. Hydrolyzed PMMA and EAA spheres were selected because of their low cost. The parameters for fabricating paraffin spheres and hydrolyzing PMMA spheres were determined. The conditions of assembling spheres were identified. Sintering temperature and time

were the two major parameters affecting the porosity of the assembled samples.

- Hydrophilic PEG/BPS foams with micro and nano-sized open cells were fabricated via solid state foaming, and the foams' applicability as fuel cell humidification membrane was investigated. BPS was selected as the polymer matrix because it is highly hydrophilic, fully amorphous, and mechanically strong. However, PEG was applied as a plasticizer to BPS because BPS is brittle at a low humidity. The parameters of saturation and foaming were investigated. Foaming temperature and blend composition determined the porosity and pore size of foamed samples. PEG200 containing blends have a low gas concentration and low porosity after foaming. Testing results indicated that PEG600 containing foams had a significant increase in both humidification rate and the maximum relative humidity that can be achieved, comparing to the corresponding solid membranes. The PEG200 containing foams had almost no changes from the unfoamed sample. High porosity levels and nano pores connecting the micro cells in foamed PEG600/BPS membranes are the main reason for the increase in humidification performance of the foamed membranes. The humidification performance of foamed PEG600-20/BPS membrane is comparable with Nafion 212 membrane under the applied test conditions. Unfoamed PEG/BPS membranes would crack under low humidity conditions, while foamed membranes remained an integral piece under those conditions. Air leak test results indicate

that foamed PEG/BPS membranes have an air leak rate much lower than the DOE requirement for a humidification membrane. Furthermore, the high T_g (> 130 ºC) of PEG600-20/BPS allows an operation temperature higher than that of Nafion. In addition, the price of PEG/BPS membranes (both foamed and solid) is (< \$300/m^2) much lower than ~\$1000/m^2 for Nafion (50 μm). The foamed PEG/BPS membranes showed potential as an alternative for fuel cell humidification applications.

- The fabricated microsphere templates were used for plating nickel foams. The electroplating approach was shown not suitable for fabricating bulk nickel foams due to the limitation of ion diffusion in the porous structure. A novel electropolishing assisted electroless plating approach was developed to fabricate microcellular nickel foams. Ethanol based electroless plating solutions were used to further reduce the surface tension of polymer microspheres. The results indicate that the developed approach could deposit nickel thoroughly and evenly across PMMA and paraffin microsphere templates up to 2.5 mm thick (equivalent to 25 layers of spheres), while the eletroless plating process alone could only plate nickel on a few layers of spheres with the same amount of plating time. Even given plenty of time, thoroughly plated microsphere templates could not be obtained due to the limitation to ion diffusion.
- A finite difference model was developed to study mechanisms of the developed bulk nickel foam fabrication approach and determine

suitable conditions for nickel foams with different cell sizes. When only electroless plating was applied, plated nickel thickness on near surface layers were much thicker than that on interior layers. The thick near surface nickel coating reduced the porosity and increased the tortuosity of the microsphere template, thus leading to reduced diffusivity of ion into the template interior. As a result, uneven nickel plating happened. When electropolishing was introduced, the near surface nickel was polished off faster than the interior nickel due to an uneven polishing current distribution resulted from the uneven nickel thickness from the former electroless plating process. Hence, a relatively constant ion diffusion rate toward the interior was maintained. Finally, a relatively evenly distributed nickel thickness was formed. Suitable conditions for electropolishing assisted electroless plating process for templates with different sphere sizes were determined with the model.

- 3D few layer graphene foams were fabricated using the obtained nickel foam as a template. The microcellular Ni foam templates exhibited sufficient thermal stability for few layer graphene growth in the APCVD process, yielding graphene foams with a pore size less than 100 μm, density of 0.0020 $g \cdot cm^{-3}$, and pore wall thickness of 5 nm. The 3D graphene foam has a cellular morphology with surface-to-volume ratio of 2.5×10^5 $m^2 \cdot m^{-3}$ and is expected to find applications in energy storage devices for balanced high loading and fast charging and discharging rates.

8.2 FUTURE WORK

The current work has paved way for further study, which could include the following.

8.3.1 Extending applications of hydrophilic polymer nanofoams

Hydrophilic polymer foams with micro and nano-sized open cells could be used as templates for fabricating nano pore-sized nickel foam and as water treatment membranes. Comparing with the existing methods for fabricating nano-sized Ni foams, which are electrodeposition of costly polymer nano-sphere templates (> $100 per 10 mL water suspension) and electroless deposition of nanoporous polymer foams from chemical degradation of block copolymers, the as developed hydrophilic polymer foams are at a much lower cost and require a simple and environmentally friendly fabrication process. The challenge will be the removal of the solid skin layers. The developed hydrophilic foams are a possible candidate for water treatment membrane owing to its higher water permeability resulted from its open nano-sized pores, compared with the solid membranes. Foaming may reduce the amount of material needed and thus lower cost as well. The fabrication of Ni nanofoams with hydrophilic polymer nanofoams as templates could be investigated. The application of hydrophilic polymer nanofoams as water treatment membrane could be addressed. New foaming conditions need to be developed to realize those potentials.

8.3.2 Improvement on the process model

The current finite difference model was validated with the measured nickel thickness on different microsphere layers. However, the current measurements were based on freeze-fractured SEM samples, where accurate measurements of nickel

coating thickness have been challenging. A better sample preparation method could be developed to allow more accurate coating thickness measurements.

8.3.3 Application of nickel/graphene microcellular foams in energy storage applications

Fabricated nickel foams and graphene foams could be used as a scaffold for energy storage electrodes. Suitable active materials with high energy density and compatibility with the scaffold could be developed or selected. Potential candidate active materials could include electrically conductive polymer and nano silicon blends, metal oxides, and lithium ion electrode materials such as $LiFePO_4$. Devices and infiltration approaches need to be developed to test this electrode design concept.

References

[1]. Li, S., Y. Wang, Y. Liu, and W. Sun, *Estimation of Thermal Conductivity of Porous Material with FEM and Fractal Geometry.* International Journal of Modern Physics C, 2009. 20(4): p. 513-526.

[2]. Wang, M. and N. Pan, *Modeling and Prediction of the Effective Thermal Conductivity of Random Open-Cell Porous Foams.* International Journal of Heat and Mass Transfer, 2008. 51(5-6): p. 1325-1331.

[3]. Chen, Y., X. Zhang, P. Yu, and Y. Ma, *Electrophoretic deposition of graphene nanosheets on nickel foams for electrochemical capacitors.* Journal of Power Sources, 2010. 195(9): p. 3031-3035.

[4]. Zhang, H.Y., D. Pinjala, Y.K. Joshi, T.N. Wong, and K.C. Toh, *Development and Characterization of Thermal Enhancement Structures for Single-Phase Liquid Cooling in Microelectronics Systems.* Heat Transfer Engineering, 2007. 28(12): p. 997-1007.

[5]. Apprill, J.M., D.R. Poirier, M.C. Maguire, and T.C. Gutsch, *porous metals process control.* MRS Online Proceedings Library, 1998. 521: p. 291-296.

[6]. Banhart, J., *Manufacture, characterisation and application of cellular metals and metal foams.* Progress in materials Science, 2001. 46(6): p. 559-632.

[7]. Bram, M., C. Stiller, H.P. Buchkremer, D. Stöver, and H. Baur, *High-porosity titanium, stainless steel, and superalloy parts.* Advanced Engineering Materials, 2000. 2(4): p. 196-199.

[8]. Clancy, R.B., J.K. Cochran, and T.H. Sanders, *Fabrication and properties of hollow sphere nickel foams.* MRS Online Proceedings Library, 1994. 372: p. 155-165.

[9]. Salehi, P., P. Sarazin, and B.D. Favis, *Porous Devices Derived from Co-Continuous Polymer Blends as a Route for Controlled Drug Release.* Biomacromolecules, 2008. 9(4): p. 1131-1138.

[10]. Sarazin, P., X. Roy, and B.D. Favis, *Controlled Preparation and Properties of Porous Poly(l-lactide) Obtained from a Co-continuous Blend of Two Biodegradable Polymers.* Biomaterials, 2004. 25(28): p. 5965-5978.

[11]. Wadley, H.N.G., *Cellular metals manufacturing: an overview of stochastic and periodic concepts*. in *Cellular Metals and Metal Foaming Technology*. 2001. Verlag-MIT.

[12]. Yamada, Y., T. Banno, Y. Li, and C. E. Wen., *Anisotropic mechanical properties of nickel foams fabricated by powder metallurgy*. 2008. Trans Tech Publications Ltd.

[13]. Ghanem, M.A., P.N. Bartlett, P. De Groot, and A. Zhu, *A double templated electrodeposition method for the fabrication of arrays of metal nanodots.* Electrochemistry communications, 2004. 6(5): p. 447-453.

[14]. Hao, Y., F. Zhu, C. Chien, and P.C. Searson, *Fabrication and magnetic properties of ordered macroporous nickel structures.* Journal of the Electrochemical Society, 2007. 154(2): p. D65-D69.

[15]. Dong, X., Y. Ma, G. Zhu, Y. Huang, J. Wang, M.B. Chan-Park, et al., *Synthesis of graphene–carbon nanotube hybrid foam and its use as a novel three-dimensional electrode for electrochemical sensing.* Journal of Materials Chemistry, 2012. 22(33): p. 17044-17048.

[16]. Ning, J., X. Xu, C. Liu, and D. Fan, *Three-dimensional multilevel porous thin graphite nanosuperstructures for Ni (OH) 2-based energy storage devices.* Journal of Materials Chemistry A, 2014. 2(38): p. 15768-15773.

[17]. Singh, E., Z. Chen, F. Houshmand, W. Ren, Y. Peles, H.M. Cheng, et al., *Superhydrophobic graphene foams.* small, 2013. 9(1): p. 75-80.

[18]. Xiao, X., T.E. Beechem, M.T. Brumbach, T.N. Lambert, D.J. Davis, J.R. Michael, et al., *Lithographically defined three-dimensional graphene structures.* ACS nano, 2012. 6(4): p. 3573-3579.

[19]. Braun, P.V., *Materials Chemistry in 3D Templates for Functional Photonics.* Chemistry of Materials, 2013. 26(1): p. 277-286.

[20]. Jiang, P. and M.J. McFarland, *Large-scale fabrication of wafer-size colloidal crystals, macroporous polymers and nanocomposites by spin-coating.* Journal of the American Chemical Society, 2004. 126(42): p. 13778-13786.

[21]. Yu, A., F. Meiser, T. Cassagneau, and F. Caruso, *Fabrication of polymer-nanoparticle composite inverse opals by a one-step electrochemical co-deposition process.* Nano Letters, 2004. 4(1): p. 177-181.

[22]. Wang, D. and F. Caruso, *Fabrication of polyaniline inverse opals via templating ordered colloidal assemblies.* Advanced materials, 2001. 13(5): p. 350-354.

[23]. Eaves, D., *Polymer Foams-Trends in Use and Technology*1996, Shawbury, UK: Smithers Rapra Press. 152.

[24]. Cui, Z., B. Nelson, Y. Peng, K. Li, S. Pilla, W.-J. Li, et al., *Fabrication and characterization of injection molded poly (ε-caprolactone) and poly (ε-caprolactone)/hydroxyapatite scaffolds for tissue engineering.* Materials Science and Engineering: C, 2012. 32(6): p. 1674-1681.

[25]. Kang, J., *The synthesis of nanoporous hydrogels using sacrificial block copolymers*, 2006, Massachusetts Institute of Technology.

[26]. Hua, Y., S. Zhang, Y. Zhu, Y. Chu, and J. Chen, *Hydrophilic polymer foams with well‐defined open‐cell structure prepared from pickering high internal phase emulsions.* Journal of Polymer Science Part A: Polymer Chemistry, 2013. 51(10): p. 2181-2187.

[27]. Zhao, Y.-H., Y.-Y. Xu, and B.-K. Zhu, *In situ crosslinking of hyperbranched polyglycerol in casting solutions and its effect on the structure and properties of porous PVDF membranes.* Journal of Applied Polymer Science, 2010. 117(1): p. 548-556.

[28]. Virgilio, N., P. Sarazin, and B.D. Favis, *Towards ultraporous poly(l-lactide) scaffolds from quaternary immiscible polymer blends.* Biomaterials, 2010. 31(22): p. 5719-5728.

[29]. Sundarram, S.S., W. Jiang, and W. Li, *Fabrication of Small Pore-Size Nickel Foams using Electroless Plating of Solid-state Foamed Immiscible Polymer Blends.* Journal of Manufacturing Science and Engineering, 2013. Submitted.

[30]. Miller, D., P. Chatchaisucha, and V. Kumar, *Microcellular and nanocellular solid-state polyetherimide (PEI) foams using sub-critical carbon dioxide I. processing and structure.* Polymer, 2009. 50(23): p. 5576-5584.

[31]. Wang, X., *Solvent-free fabrication of porous polymer for tissure engineering applications*, 2007, University of Washington: Seattle, WA, USA.

[32]. Zhou, C., N. Vaccaro, S.S. Sundarram, and W. Li, *Fabrication and characterization of polyetherimide nanofoams using supercritical CO2.* Journal of Cellular Plastics, 2012. 48(3): p. 239-255.

[33]. Aher, B., N.M. Olson, and V. Kumar, *Production of bulk solid-state PEI nanofoams using supercritical CO2.* Journal of Materials Research, 2013. FirstView: p. 1-8.

[34]. Krause, B., K. Diekmann, N.F.A. van der Vegt, and M. Wessling, *Open Nanoporous Morphologies from Polymeric Blends by Carbon Dioxide Foaming.* Macromolecules, 2002. 35(5): p. 1738-1745.

[35]. Krause, B., H.J.P. Sijbesma, P. Münüklü, N.F.A. van der Vegt, and M. Wessling, *Bicontinuous Nanoporous Polymers by Carbon Dioxide Foaming.* Macromolecules, 2001. 34(25): p. 8792-8801.

[36]. Tappan, B.C., S.A. Steiner Iii, and E.P. Luther, *Nanoporous Metal Foams.* Angewandte Chemie International Edition, 2010. 49(27): p. 4544-4565.

[37]. Vukovic, I., S. Punzhin, Z. Vukovic, P. Onck, J.T.M. De Hosson, G. ten Brinke, et al., *Supramolecular route to well-ordered metal nanofoams.* ACS Nano, 2011. 5(8): p. 6339-6348.

[38]. Lefebvre, L.P., J. Banhart, and D. Dunand, *Porous metals and metallic foams: current status and recent developments.* Advanced Engineering Materials, 2008. 10(9): p. 775-787.

[39]. Liu, P. and K. Liang, *Preparation and corresponding structure of nickel foam.* Materials science and technology, 2000. 16(5): p. 575-578.

[40]. Ye, S., J. Feng, and P. Wu, *Deposition of Three-Dimensional Graphene Aerogel on Nickel Foam as a Binder-Free Supercapacitor Electrode.* ACS applied materials & interfaces, 2013.

[41]. Wang, Z.-L., D. Xu, H.-G. Wang, Z. Wu, and X.-B. Zhang, *In Situ Fabrication of Porous Graphene Electrodes for High-Performance Energy Storage.* ACS nano, 2013. 7(3): p. 2422-2430.

[42]. Chen, J., C. Li, and G. Shi, *Graphene Materials for Electrochemical Capacitors.* The Journal of Physical Chemistry Letters, 2013. 4(8): p. 1244-1253.

[43]. Chen, Z., W. Ren, L. Gao, B. Liu, S. Pei, and H.-M. Cheng, *Three-dimensional flexible and conductive interconnected graphene networks grown by chemical vapour deposition.* Nature materials, 2011. 10(6): p. 424-428.

[44]. Baumeister, J. and J. Weise, *Manufacturing Processes for Metal Foams.* Metal Foams: Fundamentals and Applications, 2012: p. 1.

[45]. Brown, I., D. Clift, and S. Sotiropoulos, *Preparation of microporous nickel electrodeposits using a polymer matrix.* Materials research bulletin, 1999. 34(7): p. 1055-1064

[46]. Jinghuai, Z., H. Zhilin, X. Huiping, F. Zhengqiu, and Y. Chengzhou, *Study on Electroless Nickel on Foam Polyurethane [J].* Chinese Journal of Rare Metals, 2001. 4: p. 011.

[47]. Kuphal, J.A., L.M. Robeson, and J.J. Weber, *Blends of poly (propylene carbonate) and poly (methyl methacrylate) and their use in decomposition molding*, 1989, Google Patents.

[48]. LI, K., J. LUO, Y. LIU, and Y. TANG, *Electroless plating in synthesizing nickel foams [J].* High Power Laser and Particle Beams, 2007. 7: p. 023.

[49]. Liu, P. and K. Liang, *Review Functional materials of porous metals made by P/M, electroplating and some other techniques.* Journal of materials science, 2001. 36(21): p. 5059-5072.

[50]. Paserin, V., S. Marcuson, J. Shu, and D.S. Wilkinson, *The chemical vapor deposition technique for Inco nickel foam production–manufacturing benefits and potential applications*. in *Proc. of the conf. metfoam*. 2003.

[51]. Smorygo, O., V. Mikutski, A. Marukovich, A. Ilyushchanka, V. Sadykov, and A. Smirnova, *An inverted spherical model of an open-cell foam structure.* Acta Materialia, 2011. 59(7): p. 2669-2678.

[52]. Stein, A., *Sphere templating methods for periodic porous solids.* Microporous and Mesoporous Materials, 2001. 44: p. 227-239.

[53]. Yang, S., Z. He, X. Huang, and Z. Liu, *A research on the electroless nickel plating on polycarbonate.* Electroplating and Pollution Control, 2005. 25(4): p. 32.

[54]. Zhang, H., X. Yu, and P.V. Braun, *Three-dimensional bicontinuous ultrafast-charge and-discharge bulk battery electrodes.* Nature Nanotechnology, 2011. 6(5): p. 277-281.

[55]. Zhao, X., F. Su, Q. Yan, W. Guo, X.Y. Bao, L. Lv, et al., *Templating methods for preparation of porous structures.* Journal of Materials Chemistry, 2006. 16(7): p. 637-648.

[56]. Apprill, J., D. Poirier, M. Maguire, and T. G. *Gasar, porous metals process control*. in *Materials Research Society Symposium Proceedings*. 1998. Cambridge Univ Press.

[57]. Clancy, R., J. Cochran, and T. Sanders, *Fabrication and Properties of Hollow Sphere Nickel Foams*. in *MRS Proceedings*. 1994. Cambridge Univ Press.

[58]. Banno, T., C.E. Wen, Y. Yamada, and Y.C. Li, *Anisotropic mechanical properties of nickel foams fabricated by powder metallurgy*. in *Materials science forum*. 2008. Trans Tech Publ.

[59]. Hsueh, H.Y., Y.C. Huang, R.M. Ho, C.H. Lai, T. Makida, and H. Hasegawa, *Nanoporous gyroid nickel from block copolymer templates via electroless plating.* Advanced Materials, 2011. 23(27): p. 3041-3046.

[60]. Paserin, V., S. Marcuson, J. Shu, and D.S. Wilkinson, *CVD technique for Inco nickel foam production.* Advanced Engineering Materials, 2004. 6(6): p. 454-459.

[61]. Brown, I. and S. Sotiropoulos, *Electroplating and electroless plating of Ni through/onto a porous polymer in a flow cell.* Journal of applied electrochemistry, 2001. 31(11): p. 1203-1212.

[62]. Boiko, L., *Formation of Porous Structures in Metal–Hydrogen Systems.* Materials Science, 2002. 38(4): p. 544-549.

[63]. Wadley, H., *Cellular metals manufacturing: an overview of stochastic and periodic concepts*. in *International Conference on Cellular Metals and Metal Foaming Technology*. 2001.

[64]. Andersen, O., U. Waag, L. Schneider, G. Stephani, and B. Kieback, *Novel metallic hollow sphere structures.* Advanced Engineering Materials, 2000. 2(4): p. 192-195.

[65]. Eaves, D., *Handbook of polymer foams.* polimeri, 2004. 25: p. 1-2.

[66]. Krishnan, S., J.Y. Murthy, and S.V. Garimella, *A two-temperature model for solid-liquid phase change in metal foams.* Journal of heat transfer, 2005. 127(9): p. 995-1004.

[67]. Chung, C.-K. and W. Chang, *Effect of pulse frequency on the morphology and nanoindentation property of electroplated nickel films.* Microsystem technologies, 2007. 13(5-6): p. 537-541.

[68]. Chung, C.-K. and W.-T. Chang, *Deep nickel metal deposition on multiscale feature sizes of a small hole and large sector cavities using electroforming.* Journal of Micro/Nanolithography, MEMS, and MOEMS, 2009. 8(2): p. 021111-021111-6.

[69]. Mallory, G.O. and J.B. Hajdu, *Electroless plating fundamentals and applications*1990, Orlando, FL: William Andrew. 539.

[70]. Dullien, F.A., *Porous media: fluid transport and pore structure*2012: Academic press.

[71]. Stein, A. and R.C. Schroden, *Colloidal crystal templating of three-dimensionally ordered macroporous solids: materials for photonics and beyond.* Current Opinion in Solid State and Materials Science, 2001. 5(6): p. 553-564.

[72]. Velev, O.D. and A.M. Lenhoff, *Colloidal crystals as templates for porous materials.* Current opinion in colloid & interface science, 2000. 5(1): p. 56-63.

[73]. Kemsheadl, J. and J. Ugelstad, *Magnetic separation techniques: their application to medicine.* Molecular and cellular Biochemistry, 1985. 67(1): p. 11-18.

[74]. Akbulut, O., C.R. Mace, R.V. Martinez, A.A. Kumar, Z. Nie, M.R. Patton, et al., *Separation of nanoparticles in aqueous multiphase systems through centrifugation.* Nano letters, 2012. 12(8): p. 4060-4064.

[75]. Goddard, J.M. and J. Hotchkiss, *Polymer surface modification for the attachment of bioactive compounds.* Progress in polymer science, 2007. 32(7): p. 698-725.

[76]. Chen, D., W. Li, and H. Peng, *An experimental study and model validation of a membrane humidifier for PEM fuel cell humidification control.* Journal of Power Sources, 2008. 180(1): p. 461-467.

[77]. Koo, J.H., *Polymer nanocomposites: processing, characterization, and applications*2006: McGraw-Hill New York.

[78]. Vaia, R.A., G. Price, P.N. Ruth, H.T. Nguyen, and J. Lichtenhan, *Polymer/layered silicate nanocomposites as high performance ablative materials.* Applied Clay Science, 1999. 15(1): p. 67-92.

[79]. Oh, H.J., B.D. Freeman, J.E. McGrath, C.H. Lee, and D.R. Paul, *Thermal analysis of disulfonated poly (arylene ether sulfone) plasticized with poly (ethylene glycol) for membrane formation.* Polymer, 2014. 55(1): p. 235-247.

[80]. Lee, C.H., D. VanHouten, O. Lane, J.E. McGrath, J. Hou, L.A. Madsen, et al., *Disulfonated poly (arylene ether sulfone) random copolymer blends tuned for rapid water permeation via cation complexation with poly (ethylene glycol) oligomers.* Chemistry of materials, 2011. 23(4): p. 1039-1049.

[81]. Jacobs, M. *Carbon dioxide pressure-temperature phase diagram*. 2005; Available from: http://en.wikipedia.org/wiki/File:Carbon_dioxide_pressure-temperature_phase_diagram.svg.

[82]. ASTM, *Standard Test Methods for Density and Specific Gravity (Relative Density) of Plastics by Displacement*, in *D792*,2008.

[83]. Michler, G.H. and F. Baltá-Calleja, *Mechanical properties of polymers based on nanostructure and morphology*. Vol. 71. 2005: CRC Press.

[84]. Garland, N., T. Benjamin, and J. Kopasz, *DOE fuel cell program: durability technical targets and testing protocols.* ECS Transactions, 2007. 11(1): p. 923-931.

[85]. Yu, Y., C.H. Chen, J.L. Shui, and S. Xie, *Nickel‐Foam‐Supported Reticular CoO‐Li2O Composite Anode Materials for Lithium Ion Batteries.* Angewandte Chemie International Edition, 2005. 44(43): p. 7085-7089.

[86]. Huang, X., J. Tu, X. Xia, X. Wang, and J. Xiang, *Nickel foam-supported porous NiO/polyaniline film as anode for lithium ion batteries.* Electrochemistry communications, 2008. 10(9): p. 1288-1290.

[87]. Yang, C., D. Zhang, Y. Zhao, Y. Lu, L. Wang, and J.B. Goodenough, *Nickel foam supported Sn–Co alloy film as anode for lithium ion batteries.* Journal of Power Sources, 2011. 196(24): p. 10673-10678.

[88]. Li, J., Q.M. Yang, and I. Zhitomirsky, *Nickel foam-based manganese dioxide–carbon nanotube composite electrodes for electrochemical supercapacitors.* Journal of Power Sources, 2008. 185(2): p. 1569-1574.

[89]. Wang, G., J. Huang, S. Chen, Y. Gao, and D. Cao, *Preparation and supercapacitance of CuO nanosheet arrays grown on nickel foam.* Journal of Power Sources, 2011. 196(13): p. 5756-5760.

[90]. Wang, Y.-L., Y.-Q. Zhao, and C.-L. Xu, *May 3D nickel foam electrode be the promising choice for supercapacitors.* Journal of Solid State Electrochemistry, 2012. 16(3): p. 829-834.

[91]. Oya, T., T. Nomura, N. Okinaka, and T. Akiyama, *Phase change composite based on porous nickel and erythritol.* Applied Thermal Engineering, 2012. 40: p. 373-377.

[92]. Li, S.S.S.a.W., *The Effect of Pore Size and Porosity on Thermal Management Performance of Phase Change Material Infiltrated Microcellular Metal Foams.* Applied Thermal Engineering, 2013. Accepted.

[93]. Sundarram, S.S. and W. Li, *On thermal conductivity of micro‐and nanocellular polymer foams.* Polymer Engineering & Science, 2013.

[94]. Yan, H., C.F. Blanford, J.C. Lytle, C.B. Carter, W.H. Smyrl, and A. Stein, *Influence of processing conditions on structures of 3D ordered macroporous metals prepared by colloidal crystal templating.* Chemistry of materials, 2001. 13(11): p. 4314-4321.

[95]. Bulasara, V.K., R. Uppaluri, and M.K. Purkait, *Effect of ultrasound on the performance of nickel hydrazine electroless plating baths.* Materials and Manufacturing Processes, 2012. 27(2): p. 201-206.

[96]. Wong, K., K. Chan, and T. Yue, *A study of surface finishing in pulse current electroforming of nickel by utilizing different shaped waveforms.* Surface and Coatings Technology, 1999. 115(2): p. 132-139.

[97]. Mallory G O, H.J.B., *Electroless plating-fundamentals and Applications*, in *American Electroplaters and Surface Finishers Society*.

[98]. Bo-Ming, Y. and L. Jian-Hua, *A geometry model for tortuosity of flow path in porous media.* Chinese Physics Letters, 2004. 21(8): p. 1569.

[99]. Jun, J.B., M.S. Seo, S.H. Cho, J.G. Park, J.H. Ryu, and K.D. Suh, *Synthesis of monodisperse nickel‐coated polymer particles by electroless plating method utilizing functional polymeric ligands.* Journal of Applied Polymer Science, 2006. 100(5): p. 3801-3808.

[100]. Cao, X., Y. Shi, W. Shi, G. Lu, X. Huang, Q. Yan, et al., *Preparation of novel 3D graphene networks for supercapacitor applications.* Small, 2011. 7(22): p. 3163-3168.

[101]. Maiyalagan, T., X. Dong, P. Chen, and X. Wang, *Electrodeposited Pt on three-dimensional interconnected graphene as a free-standing electrode for fuel cell application.* Journal of Materials Chemistry, 2012. 22(12): p. 5286-5290.

[102]. Sundarram, S.S. and W. Li, *The effect of pore size and porosity on thermal management performance of phase change material infiltrated microcellular metal foams.* Applied Thermal Engineering, 2014. 64(1): p. 147-154.

[103]. Wei, W., S. Yang, H. Zhou, I. Lieberwirth, X. Feng, and K. Müllen, *3D graphene foams cross‐linked with pre‐encapsulated Fe3O4 nanospheres for enhanced lithium storage.* Advanced materials, 2013. 25(21): p. 2909-2914.

[104]. Choi, B.G., M. Yang, W.H. Hong, J.W. Choi, and Y.S. Huh, *3D macroporous graphene frameworks for supercapacitors with high energy and power densities.* ACS nano, 2012. 6(5): p. 4020-4028.

[105]. Lee, J.-S., H.-J. Ahn, J.-C. Yoon, and J.-H. Jang, *Three-dimensional nano-foam of few-layer graphene grown by CVD for DSSC.* Physical Chemistry Chemical Physics, 2012. 14(22): p. 7938-7943.

[106]. Ji, H., L. Zhang, M.T. Pettes, H. Li, S. Chen, L. Shi, et al., *Ultrathin graphite foam: a three-dimensional conductive network for battery electrodes.* Nano Letters, 2012. 12(5): p. 2446-2451.

[107]. J. Kim, H. K. Jung, S. H. Kim, and H. W. Lee, *The effect of various parameters for few-layered graphene synthesis using methane and acetylene* Journal of Ceramic Processing Research, 2012. 13: p. 42-46.

[108]. Yu, X., Y.J. Lee, R. Furstenberg, J.O. White, and P.V. Braun, *Filling fraction dependent properties of inverse opal metallic photonic crystals.* Advanced materials, 2007. 19(13): p. 1689-1692.

[109]. Jiang, W., S.S. Sundarram, and W. Li, *Fabrication of microcellular metal foams with sphere template electrodeposition.* Manufacturing Letters, 2014. 2(4): p. 118-121.

[110]. Klement, U., U. Erb, A. El-Sherik, and K. Aust, *Thermal stability of nanocrystalline Ni.* Materials Science and Engineering: A, 1995. 203(1): p. 177-186.

Vita

Wei Jiang was born in Yantai in China. He got his Bachelor of Engineering in Polymer Science & Engineering from College of Engineering, Qingdao University of Science and Technology, China in 2006. In fall 2006 he joined East China University of Science and Technology for his Master of Science in Polymer Science & Engineering and received his degree in 2009. He started his master program at The University of Texas at Austin in fall 2009 and started his doctorate program in fall 2011. He started working under the supervision of Dr. Wei Li in spring 2012. His areas of interest are micro and nano manufacturing for energy and thermal management applications.

Email: weizyjiang@utexas.edu

This dissertation was typed by the author.